SEISMIC PERFORMANCE DESIGN CRITERIA FOR BRIDGE BENT PLASTIC HINGE REGIONS

Final Report

SPR 802

Oregon Department of Transportation

SEISMIC PERFORMANCE DESIGN CRITERIA FOR BRIDGE BENT PLASTIC HINGE REGIONS

Final Report

PROJECT SPR 802

by

A K M Golam Murtuz, Graduate Research Assistant
Peter Dusicka, Professor
Thomas Schumacher, Associate Professor

Portland State University

for

Oregon Department of Transportation
Research Section
555 13th Street NE, Suite 1
Salem OR 97301

and

Federal Highway Administration
1200 New Jersey Avenue SE
Washington, DC 20590

November 2020

Technical Report Documentation Page

1. Report No. FHWA-OR-RD-21-04	2. Government Accession No.	3. Recipient's Catalog No.
4. Title and Subtitle Seismic Performance Design Criteria for Bridge Bent Plastic Hinge Regions		5. Report Date - November 2020- 6. Performing Organization Code
7. Author(s) A K M Golam Murtuz; 0000-0002-5058-4409 Peter Dusicka, PhD, PE; 0000-0003-2199-1619 Thomas Schumacher, PhD, PE (DE); 0000-0003-0118-9119		8. Performing Organization Report No.
9. Performing Organization Name and Address Department of Civil & Environmental Engineering Portland state University 1930 SW 4th Avenue, Suite 200 Portland, Oregon 97201		10. Work Unit No. (TRAIS) 11. Contract or Grant No.
12. Sponsoring Agency Name and Address Oregon Dept. of Transportation Research Section and Federal Highway Admin. 555 13th Street NE, Suite 1 1200 New Jersey Avenue SE Salem, OR 97301 Washington, DC 20590		13. Type of Report and Period Covered Final Report 14. Sponsoring Agency Code
15. Supplementary Notes		

16. Abstract: The main objective of this research was to quantify the material strain limits for seismic assessment of existing sub-standard reinforced concrete bridge bents considering operational performance design criteria. Limited confidence exists in the current material strain limit state for operational performance criteria due to lack of experimental results considering the typical detailing of Oregon bridges and the cumulative damage effect resulting from an anticipated long-duration Cascadia Subduction Zone (CSZ) event. Component details for bridge bents such as geometry and reinforcing details were determined through a statistical analysis of available bridge drawings built prior to 1990 in the State of Oregon. Three full-scale bridge bent column-footing subassembly specimens were constructed and subjected to reverse cyclic lateral deformations utilizing a traditional loading protocol and a protocol representing the demands expected from a CSZ earthquake. The tests were designed so that variable axial loading could be applied in order to simulate the secondary effects experienced in a column that is part of a multi-column bent during an earthquake event. Material strains along with global and local deformation quantities were measured with a suite of external and internal sensors mounted to and embedded in the specimens. Despite having sub-standard seismic detailing, all three specimens exhibited ductile behavior under reverse cyclic lateral loading, achieving a minimum displacement ductility of 8.0. The obtained results also suggest that the material strain limits currently used for the seismic evaluation of existing bridges in Oregon considering operational performance criteria are conservative, but may still require further experimental validation. Finally, strain limits based on previous research at Portland State University (PSU) were compiled and combined with the results from this study to propose recommended strain limit values.

17. Key Words: Reinforced concrete bridge columns, Subduction zone earthquakes, Large scale cyclic test, Performance-based seismic design, Strain limit states.	18. Distribution Statement Copies available from NTIS, and online at www.oregon.gov/ODOT/TD/TP_RES/		
19. Security Classification (of this report) Unclassified	20. Security Classification (of this page) Unclassified	21. No. of Pages 127	22. Price

Technical Report Form DOT F 1700.7 (8-72) Reproduction of completed page authorized Printed on recycled paper

SI* (MODERN METRIC) CONVERSION FACTORS

APPROXIMATE CONVERSIONS TO SI UNITS

Symbol	When You Know	Multiply By	To Find	Symbol
		LENGTH		
in	inches	25.4	millimeters	mm
ft	feet	0.305	meters	m
yd	yards	0.914	meters	m
mi	miles	1.61	kilometers	km
		AREA		
in^2	square inches	645.2	millimeters squared	mm^2
ft^2	square feet	0.093	meters squared	m^2
yd^2	square yards	0.836	meters squared	m^2
ac	acres	0.405	hectares	ha
mi^2	square miles	2.59	kilometers squared	km^2
		VOLUME		
fl oz	fluid ounces	29.57	milliliters	ml
gal	gallons	3.785	liters	L
ft^3	cubic feet	0.028	meters cubed	m^3
yd^3	cubic yards	0.765	meters cubed	m^3
~NOTE: Volumes greater than 1000 L shall be shown in m^3.				
		MASS		
oz	ounces	28.35	grams	g
lb	pounds	0.454	kilograms	kg
T	short tons (2000 lb)	0.907	megagrams	Mg
		TEMPERATURE (exact)		
°F	Fahrenheit	(F-32)/1.8	Celsius	°C

APPROXIMATE CONVERSIONS FROM SI UNITS

Symbol	When You Know	Multiply By	To Find	Symbol
		LENGTH		
mm	millimeters	0.039	inches	in
m	meters	3.28	feet	ft
m	meters	1.09	yards	yd
km	kilometers	0.621	miles	mi
		AREA		
mm^2	millimeters squared	0.0016	square inches	in^2
m^2	meters squared	10.764	square feet	ft^2
m^2	meters squared	1.196	square yards	yd^2
ha	hectares	2.47	acres	ac
km^2	kilometers squared	0.386	square miles	mi^2
		VOLUME		
ml	milliliters	0.034	fluid ounces	fl oz
L	liters	0.264	gallons	gal
m^3	meters cubed	35.315	cubic feet	ft^3
m^3	meters cubed	1.308	cubic yards	yd^3
		MASS		
g	grams	0.035	ounces	oz
kg	kilograms	2.205	pounds	lb
Mg	megagrams	1.102	short tons (2000 lb)	T
		TEMPERATURE (exact)		
°C	Celsius	1.8C+32	Fahrenheit	°F

*SI is the symbol for the International System of Measurement

ACKNOWLEDGEMENTS

The authors would like to thank the members of ODOT's Technical Advisory Committee as well as the Research Section for their advice and assistance during the project and preparation of this report.

DISCLAIMER

TABLE OF CONTENTS

1.0 INTRODUCTION 1

1.1 GENERAL 1
1.2 OBJECTIVE AND SCOPE 1
1.3 REPORT CONTENTS 2

2.0 PREVIOUS RESEARCH RESULTS 3

2.1 INTRODUCTION 3
2.2 LITERATURE REVIEW 3

3.0 REPRESENTATIVE BRIDGE SELECTION 11

3.1 GENERAL 11
3.2 OREGON BRIDGE INVENTORY 11
3.3 BRIDGE CHARACTERISTICS 13
3.3.1 Number of Spans, NBI Item 45 13
3.3.2 Number of Lanes, NBI Item 28A 14
3.3.3 Length of Bridge, NBI Item 49 15
3.4 TYPICAL BENT CHARACTERISTICS 16
3.4.1 Number of Columns per Bent 16
3.4.2 Column Height 16
3.4.3 Column Details 17
3.4.4 Splice Length 18
3.4.5 Foundations Details 19
3.4.6 Crossbeam Details 20
3.5 SUMMARY 20

4.0 EXPERIMENTAL PROGRAM 23

4.1 GENERAL 23
4.2 TEST MATRIX 23
4.3 GEOMETRY AND REINFORCEMENT 25
4.4 MATERIAL PROPERTIES 26
4.4.1 Steel 27
4.4.2 Concrete 27
4.5 SPECIMEN CONSTRUCTION 28
4.6 TEST SETUP 29
4.7 INSTRUMENTATION 33
4.7.1 Footing Instrumentation 33
4.7.2 Column Instrumentation 35
4.8 LOADING PROTOCOL 37
4.8.1 Axial Loading Protocol 37
4.8.2 Lateral Displacement History 39
4.9 SUMMARY 41

5.0 EXPERIMENTAL RESULTS AND ANALYSIS 43

5.1 INTRODUCTION 43

5.2 VISUAL OBSERVATIONS 43
5.2.1 Specimen SCF#8 43
5.2.2 Specimen SVF#8 45
5.2.3 Specimen LVF#8 48
5.3 MEASURED DATA 52
5.3.1 Global Response 53
5.3.2 Local Response 64
6.0 IMPACTS ON DUAL DESIGN CRITERIA 71
6.1 GENERAL 71
6.2 ODOT DESIGN PHILOSOPHY 71
6.3 EXPERIMENTAL STRAINS 74
6.3.1 Square RC Column Tests [Mehary & Dusicka (2015)] 74
6.3.2 RC Bent Tests [Gallardo (2017)] 75
6.3.3 Circular RC Column Tests [Dusicka & Lopez (2016)] 77
6.3.4 Square RC Column Tests (This Research) (4 - #8 Rebar) 79
6.4 PERFORMANCE LIMIT STATES 82
6.4.1 Operational Performance Level 82
6.4.2 Life Safety Performance Level 85
6.5 SUMMARY 85
7.0 OVERALL SUMMARY AND CONCLUSION 87
7.1 CONCLUSIONS 87
7.2 RECOMMENDATIONS FOR FUTURE RESEARCH 89
8.0 REFERENCES 91
APPENDIX A A-1

LIST OF TABLES

Table 2.1: Bridge Performance Assessment (Hose, Silva and Seible 2000) 3
Table 2.2: Strain Limit State Definition (from Priestley 2000) 4
Table 2.3: Limit State Definition (from Kowalsky 2000) 4
Table 2.4: Performance Limit State Definition (from Sheikh, et al. 2012) 5
Table 2.5: Material Strain Limit States (from Oregon Department of Transportation 2019 and Canadian Standards Association Group 2014) 8
Table 2.6: Component Performance Levels Adapted (Hose, Silva and Seible 2000) 8
Table 2.7: Limit States for RC Bridge Column with CFRP (from Jean, et al. 2012) 9
Table 3.1: Kind of Material and/or Design, NBI Item 43A (FHWA, 1995) 11
Table 3.2: Type of Design and/or Construction, NBI Item 43B (FHWA, 1995) 11
Table 3.3: Classification of Multi-span Bridges in Oregon Built Prior to 1990, based on NBI item 43 12
Table 4.1: Test Specimen Details 25
Table 4.2: Rebar Tensile Strength Result 27
Table 4.3: Concrete Compressive Strength Test Result 27

Table 6.1: ODOT's Current Performance Criteria and Strain Limit States (Oregon Department of Transportation 2019) 72
Table 6.2: Minimum Performance Level for Retrofitted Bridges Adopted by ODOT....73
Table 6.3: Bridge Performance Parameters (Limit States) for RC Square Column [Dusicka & Lopez (2016)]....75
Table 6.4: Bridge Performance Parameters (Limit States) for RC Bent [Gallardo (2017)]....77
Table 6.5: Bridge Performance Parameters (Limit States) for Circular RC Columns [Dusicka & Lopez (2016)]....79
Table 6.6: Lateral Force and Displacements for Different Damage Levels....80
Table 6.7: Measured Strains for Different Damage Levels....81
Table 6.8: Recommended Material Strain Values for Different Damage Levels in Substandard Square RC Columns 82
Table 6.9: Comparison of Recommended Strain Limits for Different Performance Objectives ..84
Table 6.10: Strain Limit State for "Operational" Performance Objective 84
Table 6.11: Strain Limit State for "Life Safety" Performance Objective 85

LIST OF PHOTOS/FIGURES

Figure 3.1: Classification of Oregon bridges....13
Figure 3.2: PMF for number of spans of CCSG bridges built prior to 1990....14
Figure 3.3: PMF for number of lanes of multi-span CCSG bridges built before 1990 14
Figure 3.4: Cumulative distribution function for bridge length 15
Figure 3.5: Frequency plot for bridge length of multi-span CCSG bridges built before 1990 15
Figure 3.6: Number of columns per bent for multi-span CCSG bridges built before 1990....16
Figure 3.7: Variation of column heights for multi-span CCSG bridges built before 1990 (a) for end bents and (b) for intermediate bents 17
Figure 3.8: Cross section and elevation view of typical column-footing details....18
Figure 3.9: (a) Variation of splice length multiplier for #8 splice bars and (b) Cumulative percentage changes for splice length multiplier....19
Figure 3.10: Plan view of a typical foundation reinforcing detail 20
Figure 4.1: Test matrix....24
Figure 4.2: (a) Column-footing longitudinal section details (b) Column cross sectional details (Section A-A), (c) Tie bar details, (d) Foundation cross section details 26
Figure 4.3: (a) Average concrete compressive strength vs. age of cylinder and (b) Average concrete compressive strength as percentage of 28-day strength vs. age of concrete 28
Figure 4.4: Elevation view of test setup....30
Figure 4.5: Illustration of lever arm arrangement for axial loading 31
Figure 4.6: Beam arrangement for variable axial load application: Plan view, Elevation view, and Static equilibrium of the system....32
Figure 4.7: Typical external instrumentation for the foundation.....34
Figure 4.8: Internal instrumentation for the foundation. (Only the foundation reinforcement is shown for simplicity; rebar with no strain gauges are shown using dashed lines) 35
Figure 4.9: Typical column external instrumentation.....36
Figure 4.10: Typical column internal instrumentation.....37
Figure 4.11: Free body diagram for variation of axial load in a two-column bridge bent.....38

Figure 4.12: Variable axial loading protocol....39
Figure 4.13: Lateral loading protocols: (a) Conventional laboratory and (b) Subduction zone loading protocol....41
Figure 5.1: Different damage states for specimen SCF#8....45
Figure 5.2: Different damage states for specimen SVF#8....48
Figure 5.3: Different damage states for specimen LVF#8....52
Figure 5.4: Computation of absolute lateral load with axial component correction....53
Figure 5.5: Measured lateral displacement correction due to foundation uplift....54
Figure 5.6: Force-Displacement response for specimen SCF#8....55
Figure 5.7: Force-Displacement response for specimen SVF#8....56
Figure 5.8: Force-Displacement response for specimen LVF#8....57
Figure 5.9: Strength degradation for tested specimens....59
Figure 5.10: Stiffness degradation for tested specimens....60
Figure 5.11: Effect of axial load variation on (a) Yield curvature, (b) Ultimate curvature, (c) Curvature ductility, (d) Yield moment, (e) Ultimate moment and (f) Peak moment capacity. All analyses performed using Response-2000....62
Figure 5.12: Backbone curve comparison for tested specimens....64
Figure 5.13: Measurement of average rotation....65
Figure 5.14: Curvature profile for (a) Pre-yield SCF#8 (b) Post-yield SCF#8, (c) Pre-yield SVF#8, (d) Post-yield SVF#8, (e) Pre-yield LVF#8 and (f) Post-yield LVF#8....67
Figure 5.15: Concrete compressive strain profiles for (a) Pre-yield SCF#8 (b) Post-yield SCF#8, (c) Pre-yield SVF#8, (d) Post-yield SVF#8, (e) Pre-yield LVF#8 and (f) Post-yield LVF#8....69
Figure 6.1: Visualization of PBSD (after Moehle and Deierlein 2004), adaptation to ODOT's requirements....72
Figure 6.2: Test setup and geometry of RC column specimen [Mehary & Dusicka (2015)]....74
Figure 6.3: RC square column performance. (a) Force-displacement hysteresis curve and (b) force-displacement envelope [Mehary & Dusicka (2015)]....75
Figure 6.4: Reinforced concrete bent test setup [Gallardo (2017)]....76
Figure 6.5: RC bent performance. (a) Force-displacement hysteresis curve and (b) force-displacement envelope [Gallardo (2017)]....77
Figure 6.6: Geometry and reinforcement of RC Bridge column specimens [Dusicka & Lopez (2016)]....78
Figure 6.7: Circular RC column performance. (a) Force-displacement hysteresis curve and (b) force-displacement envelope [Dusicka & Lopez (2016)]....79
Figure A-1: Test setup (a) Top view, (b) East face view and (c) Column external instrumentation....A-2
Figure A-2: Moment-Curvature response for specimen SCF#8 (a) 0"-3" segment, (b) 3"-9" segment, (c) 9"-15" segment, (d) 15"-24" segment, (e) 24"-33" segment, (f) 33"-39" segment, (g) 39"-102" (Top) segment and (h) Measured segment....A-4
Figure A-3: Moment-Curvature response for specimen SVF#8 (a) 0"-3" segment, (b) 3"-9" segment, (c) 9"-15" segment, (d) 15"-24" segment, (e) 24"-33" segment, (f) 33"-39" segment and (g) 39"-102" (Top) segment and (h) Measured segment....A-6
Figure A-4: Moment-Curvature response for specimen LVF#8 (a) 0"-3" segment, (b) 3"-9" segment, (c) 9"-15" segment, (d) 15"-24" segment, (e) 24"-33" segment, (f) 33"-39" segment and (g) 39"-102" (Top) segment and (h) Measured segment....A-8

Figure A-5: System deformation for SCF#8 (a) Uplift measured at the north face of foundation, (b) Uplift measured at the south face of the foundation and (c) Column top displacement due to foundation uplift (Rigid body approximation). A-9
Figure A-6: System deformation for SVF#8 (a) Uplift measured at the north face of foundation, (b) Uplift measured at the south face of the foundation and (c) Column top displacement due to foundation uplift (Rigid body approximation). A-10
Figure A-7: System deformation for LVF#8 (a) Uplift measured at the north face of foundation, (b) Uplift measured at the south face of the foundation and (c) Column top displacement due to foundation uplift (Rigid body approximation). A-11
Figure A-8: Foundation Rebar strain hysteresis for specimen SVF#8 (a) Longitudinal rebar @ 13” from column center, (b) Longitudinal rebar @ 19” from column center, (c) Longitudinal rebar @ 26” from column center, (d) Transverse rebar @ 13” from column center, (e) Transverse rebar @ 19” from column center, (f) Transverse rebar @ 13” from column center and (g) Instrumentation designation. A-13
Figure A-9: Foundation Rebar strain hysteresis for specimen LVF#8 (a) Longitudinal rebar @ 10” from column center, (b) Longitudinal rebar @ 13” from column center, (c) Longitudinal rebar @ 26” from column center, (d) Transverse rebar @ 13” from column center, (e) Transverse rebar @ 19” from column center, (f) Transverse rebar @ 13” from column center and (g) Instrumentation designation. A-15

1.0 INTRODUCTION

1.1 GENERAL

Seismic design of new bridges and assessment of existing bridges in western half of Oregon needs to consider two-level performance objectives; life-safety and operational. The life-safety performance objective is intended to ensure that a bridge does not collapse under the design earthquake; however, the bridge is expected to sustain significant damage. The operational performance objective is intended to limit the seismic damage resulting from a specific demand level so that functionality of the bridge is minimally impacted. Within the Western parts of the state, the structural design of the substructure is often governed by the operational performance criteria and not the life safety criteria. The current design methodology for the operational performance objective has two main components: use of a specific seismic hazard that has traditionally been lower than that used for life safety performance, and limit of the material strains to stricter levels than those used for life safety.

The operational performance objective often governs bridge bent design, but limited confidence exists in the selection of the appropriate material strain limits for achieving rapid return to operational condition. This lack of knowledge has cascading effects on the direct cost of construction, especially when considering the retrofit of existing bridges. This has recently been highlighted in retrofit assessment projects conducted on a select number of bridges where the designers found that the operational performance under the Cascadia Subduction Zone (CSZ) event governed the extent of retrofit required (Dusicka et. al. 2015).

Current material strain limits are based on experimental data generated for reinforced concrete columns that are either based on 1) modern detailing requirements, 2) exhibit excessively poor detailing relative to those used in existing bridges in Oregon, or 3) do not consider the cumulative damage effects from the long duration CSZ event. Recently completed tests of a bent representative of ODOT detailing were completed as part of a project on earthquake duration effects (Dusicka et. al. 2015). One of the tangent results provided limited, but tantalizing, data that pointed to a seismic performance that was better than anticipated, given the lack of modern detailing. The possible contributing factors of this surprising result may be the intermediate lap-splice lengths (between excessively short and modern long splice details) utilized in vulnerable ODOT bridges prior to the 1980s and the nearly constant axial load considered. More focused research is therefore needed to assess the influence of these variables. Specifically, on the types of detailing used in Oregon due to the potentially positive outcome on the overall seismic bridge design.

1.2 OBJECTIVE AND SCOPE

The main objective of this research is to identify the steel and concrete strain limits to be considered for the seismic assessment of existing reinforced concrete bridge bents considering the operational performance design criteria. Multi-column bents are typical for bridges in Oregon and are therefore more representative of the need to gather performance related data.

The proposed research is for experimentally evaluating large-scale reinforced concrete subassemblies representing critical parts of the bents. These primarily represent column-to-foundation and column-to-crossbeam aspects of the bent. Of key interest from the experiments are the monitoring of material strains and deformations as the bent reaches target performance levels.

The scope of the research is to revisit the definition of performance levels with respect to specific damage states and identify engineering demand parameters for individual performance levels. Experimental study consisted of three typical square RC bridge column-spread footing subassemblies; the full-scale specimens were detailed to represent conditions found in old bridge (pre-1990 bridges) construction in Oregon. The column-footing subassemblies were tested under reverse cyclic loading using standard laboratory and subduction zone loading protocols.

Finally, preliminary results of limit states for the performance-based seismic design are presented. The investigation focused on defining and quantifying structural performance and the corresponding limit state. The two performance levels required by ODOT were studied, namely Operational and Life Safety. Results from previous and current experiments were used to compare and assess the performance limit states in terms of material strains.

1.3 REPORT CONTENTS

Chapter 2.0 outlines a detailed summary of previous research on the topic and the effects of different variables on the strain limit state for bridge columns. Chapter 3.0 presents a statistical analysis for the establishment of typical bridge bent details representing pre-1990 bridges in the state of Oregon. Chapter 4.0 summarizes the development of an experimental program used for typical full-scale square reinforced concrete bridge column-footing subassembly subjected to a reverse cyclic earthquake loading protocol. Chapter 5.0 discusses the experimental evaluation of typical bridge column-footing subassemblies under reverse cyclic lateral loading protocols and analysis of the test results. Finally, Chapter 0 presents an assessment of the limit states for the performance-based seismic design adopted by the dual design criteria based on strains.

2.0 PREVIOUS RESEARCH RESULTS

2.1 INTRODUCTION

The performance-based seismic design philosophy is based on the approach that ensures certain performance objectives for new bridges or for retrofitting existing bridges. Performance objectives like operational and life safety are usually defined qualitatively based on the damage state in the structure. However, a quantitative definition of these damage states and hence the performance objective needs to be defined with respect to engineering deformation criteria such as strain, displacement, or curvature limits. Material strain values such as concrete compressive strain and steel tensile strain are inherent material properties that can be related to damage states. Past research has been dedicated for the development of strain-based limit states for reinforced concrete bridge columns. The following sections presents significant past research using material strain-limit states for reinforced concrete bridges.

2.2 LITERATURE REVIEW

In order to relate system to component level performance, five performance levels were proposed by (Hose, Silva and Seible 2000) as shown in Table 2.1. The assessment procedure developed was closely related to previous work done on buildings (Seismology Committee Structural Engineers Associat 1996). This parameterization of bridge components, sub-assemblages, and systems is useful for the development of a consistent performance-based design methodology for bridges in seismic zones.

Table 2.1: Bridge Performance Assessment (Hose, Silva and Seible 2000)

Level	Performance Level	Qualitative Performance Description	Quantitative Performance Description
I	Cracking	Onset of hairline cracks.	Cracks barely visible.
II	Yielding	Theoretical first yield of longitudinal reinforcement	Crack widths < 1 mm.
III	Initiation of Local Mechanism	Initiation of inelastic deformation. Onset of concrete spalling. Development of diagonal cracks.	Crack widths 1 - 2 mm. Length of spalled region > 1/10 cross-section depth.
IV	Full Development of Local Mechanism	Wide crack widths/spalling over full local mechanism region.	Crack widths > 2mm. Diagonal cracks extended over 2/3 cross-section depth. Length of spalled region > 1/2 cross-section depth.
V	Strength Degradation	Buckling of main reinforcement. Rupture of transverse reinforcement. Crushing of core concrete.	Crack widths > 2mm in concrete core. Measurable dilation > 5% of original member dimension.

Priestley (2000) outlined three different methods of performance-based design, including direct displacement-based design, and compared them with a traditional force-based design approach. Two performance limit states namely "Fully Operational" and "Damage Control" were presented under the direct displacement design approach. Concrete and steel strain values were used to define the structural damage states whereas residual drift ratio was used to define the non-structural damage levels. The "Fully Operational" limit state was defined by the onset of concrete crushing and/or formation of residual crack widths exceeding 1 mm. The "Damage Control" limit state was defined by core concrete compressive strain to avoid non-repairable damage due to core crushing and/or peak longitudinal steel tensile strain to avoid bar buckling and low cycle fatigue. The proposed strain limit-state values are summarized in Table 2.2.

Table 2.2: Strain Limit State Definition (from Priestley 2000)

Performance Level	Concrete Compressive Strain	Steel Tensile Strain
Fully Operational	0.004 cover concrete crushing	0.015 Residual crack widths within range of 0.5 – 1.00 mm
Damage Control	$\varepsilon_{cm} = 0.004 + 1.4\rho_s f_{yh} \varepsilon_{suh}/f'_{cc}$	$\varepsilon_{sm} = 0.6\ \varepsilon_{su}$ Bar buckling and low cycle fatigue

ρ_s = volumetric ratio, f_{yh} = yield strength, ε_{suh} = strain at maximum stress, f'_{cc} = compression strength of the confined concrete, ε_{sm} = maximum longitudinal reinforcement tensile strain, and ε_{su} = strain at maximum stress.

The research by (Kowalsky 2000) developed dimensionless curvature relationships for serviceability and damage control limit states based on concrete compressive and steel strain limits. The serviceability concrete compressive strain limit was defined as the onset of concrete crushing. On the other hand, the serviceability steel tensile strain limit was defined as the strain corresponding to a residual crack width exceeding 1.0 mm. The definition of the damage control concrete strain limit state was defined as the point up to repairable damage to core concrete. Whereas, the steel strain at damage control limit was attributed to peak tension strain in longitudinal reinforcement before any visible bar buckling takes place. The proposed strain limit state values are tabulated in Table 2.3. It should be mentioned that these strain limit state values were not verified by an experiment.

Table 2.3: Limit State Definition (from Kowalsky 2000)

Performance Level	Concrete Compressive Strain	Steel Tensile Strain
Serviceability	0.004 Concrete cover crushing	0.015 Residual crack widths > 1 mm
Damage Control	$\varepsilon_{cu} = 0.018$ Limit of economical concrete repair	0.06 Tension based bar buckling

The work carried out by (Sheikh et. al. 2012) correlated seismic performance objectives (both qualitative and quantitative) with engineering parameters that are based on experimental investigations and field investigations from recent earthquakes. The limit state values along with the corresponding qualitative and quantitative performance description are presented in Table

2.4. The authors utilized a simplified assessment methodology based on pushover analysis procedures incorporating a substitute structure approach. The substitute structure approach uses a modified linear model for the structure while considering the effect of energy dissipation in the nonlinear range of displacement. They found that the method was fully validated with available experimental data.

Table 2.4: Performance Limit State Definition (from Sheikh, et al. 2012)

Limit states	Performance Level	Quantitative Performance Description
1A	Fully Operational	$\sigma_c = f_{cr} = 0.4\sqrt{f_c'}$
1B		$\sigma_s = f_{sy}$
2	Delayed Operational	$\varepsilon_c = -0.004$ $\varepsilon_s = 0.007$ crack width = 2 mm
3	Stability	$\varepsilon_c = \varepsilon_{cc50}$ (initial core crushing) $\varepsilon_c = \varepsilon_{cu}$ (fracture of hoops) $\varepsilon_s = \varepsilon_{su} = 0.07$ (longitudinal reinforcement fracture) $\varepsilon_s = \varepsilon_{scr}$ (onset of buckling)

f'_c= concrete compressive capacity, ε_{cc50}= post peak axial strain in concrete when capacity drops to 50% of confined strength, ε_{cu}= ultimate strain of concrete, ε_s= average tensile strain in longitudinal reinforcement, ε_{su}= tensile strain at fracture, and ε_{scr}= steel strain at onset of buckling of longitudinal bars

The research undertaken by (Lehman, et al. 2004) assessed the seismic performance of 10 one-third scale models of well-confined, circular-cross-section, RC bridge columns. Key variables included were aspect ratio, longitudinal reinforcement ratio, spiral reinforcement ratio, axial load ratio, and length of the well-confined region adjacent to the zone where plastic hinging was anticipated. Data obtained from the tests were used to define different damage states, i.e. residual cracking, cover spalling, and core concrete crushing. These were defined with respect to engineering parameters such as concrete compressive strain and longitudinal steel tensile strain. Strains were obtained using foil strain gauges on the longitudinal and spiral reinforcement. Concrete compressive strains were approximated using external deformation measurements. All columns showed similar damage progression, i.e. concrete cracking, longitudinal reinforcement yielding, initial spalling of concrete cover, complete spalling of concrete cover, spiral fracture, longitudinal reinforcement buckling, and longitudinal reinforcement fracture. It was found that the residual crack width was insignificant below the yield strength of longitudinal reinforcement. In addition, it is unrealistic to define residual crack width in terms of maximum previous reinforcement strain due to large scatter in the data analyzed. However, concrete cover spalling and core concrete crushing were attributed to a range of measured strains of 0.0039 to 0.011 and 0.010 to 0.029, respectively. Lower spalling strains were observed for larger column aspect ratios whereas axial load ratio, reinforcement ratio, and confinement ratio were not found to have a significant influence on the considered range of damage. Finally, it was found that the longitudinal bar buckling/reinforcement fracture failure mode depends on the lateral loading history and can thus not be captured by a single strain limit.

(Moyer and Kowalsky 2003) Presented a hypothesis regarding the bar buckling mechanism which states that the buckling of reinforcing bars upon load reversal are directly influenced by the peak tensile strain. They have experimentally validated the hypothesis on influence of tension strain on the buckling behavior of longitudinal reinforcing bar in RC columns. It was also observed that a cyclic load history had a pronounced effect on peak tension strain prior to bar buckling. In addition, the nature of the effect of load history was investigated and it was found that either extensive cycles at low response levels or only one cycle at a higher level of response can cause an accumulation of this tension strain.

An experimental study by Goodnight, et al. (2013), investigated the effect of lateral displacement history on the bar buckling limit state of well-confined circular RC bridge columns. The results showed that the buckling of reinforcing bar can take place at a relatively low peak tensile strain under a lateral displacement history with a large enough compressive demand. This impact of the load history is mainly due to the accumulated strain within the transverse and longitudinal reinforcing bars. However, it was also found that the strain and displacement envelopes were independent of the effect of displacement history.

Feng et al. (2014a), (2014b) developed a hybrid fiber based and finite element model to investigate the effect of the seismic load history on bar buckling limit states in RC bridge columns. Their analytical investigations showed that the buckling of a longitudinal reinforcing bar depends on bar diameter and the spacing and diameter of the transverse reinforcement. It was also observed that when the transverse reinforcement experienced inelastic strain, this adversely affected the peak tensile strain corresponding to the bar buckling limit state.

The most notable recent experimental endeavor by Goodnight, et al. (2016) consisted of thirty full-scale circular, well-confined, RC bridge columns to investigate the strain limits for different damage states, namely serviceability, spiral yielding, and reinforcing bar buckling. Key variables included in this study were lateral displacement history, axial load, longitudinal steel ratio, aspect ratio of the columns, and transverse reinforcement detailing. Strains were measured using non-contact 3D position sensors through tracking a network of markers in the 3D space with an accuracy of 0.1 mm, which allowed accurate measurement of strains comparable to conventional surface-mounted sensors. The sequence of damage observed during the test was concrete cracking, longitudinal reinforcement yielding, cover concrete spalling, transverse reinforcement yielding, longitudinal bar buckling, and fracture of previously buckled bars. Material strains at the onset of the respective failure modes were recorded and presented with respect to the three performance limit states.

The “serviceability” limit state as defined by Goodnight, et al. (2016) as the point beyond which an interruption of use of a bridge is necessary without posing a safety concern and require some degree of intervention for the long-term serviceability of the structure. This limit state is attributed to cover concrete spalling or residual crack widths large enough to require epoxy injection to prevent future corrosion. The results from the experimental study showed that a concrete compressive strain limit of 0.0048 was reasonable to minimize the prediction error and measured crushing strains. However, a concrete compressive strain limit of 0.004 at the serviceability limit state was maintained. The conservatism in the strain limit value was counteracted by the equivalent moment curvature distribution proposed by Goodnight, et al. (2016) for calculating the target displacement. On the other hand, a steel tensile strain limit

value of 0.015 as defined by Kowalsky (2000) corresponding to a serviceability limit state with 1 mm crack width was found to be conservative and implies that the serviceability limit state is governed by the concrete crushing strain limit state.

Transverse reinforcement yielding was stated as a limit state by Goodnight, et al. (2016) that prompts changes in the repair strategy from cover concrete patching or epoxy injection to additional transverse stiffness in the plastic hinge regions. The onset of transverse reinforcement yielding was expressed in terms of concrete compressive strain. An empirical equation was formulated to predict the concrete compressive strain at the onset of transverse reinforcement yielding. The empirical relationship as presented by Equation 2.1 relates the effect of longitudinal reinforcement ratio to the expected yield strain of the transverse reinforcement. Moreover, data obtained from the experimental study of Goodnight, et al. (2016) it was found that localization of compressive demand can occur in the regions with inelastic transverse steel reinforcement.

$$\varepsilon_{c,\,spiral\,yield} = 0.009 - 0.3*(A_{st}/A_g) + 3.9*(f_{yhe}/E_s) \quad \textbf{(2-1)}$$

Where:

$\varepsilon_{c,\,spiral\,yield}$ = Concrete compressive strain at the onset of transverse reinforcement yielding, A_{st}/A_g = Longitudinal reinforcement ratio, f_{yhe}/E_s = Expected yield strain of the transverse steel.

The bar buckling limit state was defined by (Goodnight et. al. 2016) as the peak tensile strain in the longitudinal reinforcement prior to bar buckling. An empirical relationship was developed with respect to transverse steel ratio, expected yield strain of transverse reinforcement and column axial load ratio. Equation 2.2 presents the bar buckling limit state developed by Goodnight, et. al. (2016). However, buckling of the longitudinal reinforcement was observed to take place while the bar is under net elongation but compressive stress.

$$\varepsilon_{s,\,bar\,buckling} = 0.03 + 700*\rho_s*(f_{yhe}/E_s) - 0.1*(P/f'_{ce}*A_g) \quad \textbf{(2-2)}$$

Where:

ρ_s = Transverse volumetric steel ratio, $P/f'_{ce}*A_g$ = Column axial load ratio with expected material properties.

Also, the Oregon Bridge Design Manual (Oregon Department of Transportation 2019) and Canadian Highway Bridge Design Code (Canadian Standards Association Group 2013) have defined the material strain limit states for different performance criteria and are tabulated in Table 2.5.

Table 2.5: Material Strain Limit States (from Oregon Department of Transportation 2019 and Canadian Standards Association Group 2014)

Canadian Highway Bridge Design Code	**Material**	**Minimal damage**	**Repairable Damage**	**Extensive Damage**	**Probable Replacement**
	Concrete	0.006	-	Extensive concrete spalling is permitted but $\varepsilon cc \leq 0.8*\varepsilon cu$	Damage does not cause crushing of confined concrete core
	Steel	0.010	0.025	0.05	0.075 0.06 for 35M or larger
ODOT	**Material**	**Operational**		**Life Safety**	
	Concrete	$\varepsilon_{cc} = 0.005$		$\varepsilon_{cc} = 0.9* \varepsilon_{cu}$	
	Steel	$2*\varepsilon_{sh}$		ε^{R}_{su}	

Where:

ε_{cc} = the confined compressive strain, ε_{cu} = the ultimate confined compressive strain, ε_{sh} = Onset of strain hardening (values tabulated in BDM Table 2), ε^{R}_{su} = Reduced ultimate tensile strain (values tabulated in BDM Table 2)

Research conducted by Hose, Silva, and Seible (2000) classified the component performance into five distinct levels for bridges based on past experiments at the University of California, San Diego (UCSD). The five performance levels are presented in Table 2.6 and the corresponding performance objective based on ODOT requirements were corresponded. According to Hose, Silva, and Seible (2000) the 'operational' performance level corresponds to first yielding and minor cracking, whereas the 'life safety' performance level corresponds to the onset of concrete spalling. However, ODOT defines the 'operational' performance level as the onset of spalling and the 'life safety' performance level as the buckling/fracture of the longitudinal rebar.

Table 2.6: Component Performance Levels Adapted (Hose, Silva and Seible 2000)

Level	Damage Classification	Component Performance	Repair Description	Hose, Silva, and Seible Global Performance	ODOT's Performance
I	No	Cracking	No Repair	Fully Operational	-
II	Minor	First Yield	Possible Repair	Operational	-
III	Moderate	Effective Yield	Possible Repair	-	-
IV	Major	Onset of Spalling	Minimum Repair	Life Safety	Operational
V	Local Failure/Collapse	Buckling or Rupture	Replacement	Collapse	Life Safety

Research by Jean, et al. 2012 proposed new limit states for RC columns confined with CFRP. The experimental program comprised of four columns. The yielding of the longitudinal and transverse reinforcement, cracks in concrete and the rupture of the FRP were monitored in real time using the ultrasonic pulse velocity (UPV) method. A constant axial load ratio of $0.1A_g f'_c$ was used for all columns tested. Table 2.7 depicts the limits states for RC bridge columns confined with CRFP. The authors found that the damage sequence for RC bridge columns confined with FRP was different from the sequence for conventional RC columns. Yielding of the longitudinal and transverse reinforcement becomes the first step, followed by CFRP matrix rupture. Buckling or failure of the longitudinal reinforcement takes place at the end. Spalling of the concrete cover is no longer a limit state due to the confinement provided by the FRP wrapping. Moreover, cracks in concrete, yielding of the transverse reinforcement, and failure of the longitudinal reinforcement are all delayed and occur at larger displacements and ductility ratios. New values for moderate and severe damage levels were also proposed.

Table 2.7: Limit States for RC Bridge Column with CFRP (from Jean, et al. 2012)

Damage Level	**Recommended values in the literature and corresponding damage state**				**Proposed values and corresponding damage state for the tested columns**			
	Damage	**ε_c**	**μ**	**$I_w i/I_w$**	**Damage**	**ε_c**	**μ**	**$I_w i/I_w$**
Moderate	Spalling of Concrete	0.004 - 0.011	3	0.15	Yielding of transversal steel	0.02	4 - 5	0.40
Severe	Concrete core crushing	0.02	6	0.40	Failure of CFRP	0.035	8	1.00

3.0 REPRESENTATIVE BRIDGE SELECTION

3.1 GENERAL

The material strain limit states currently in use are based on experimental data generated for reinforced concrete columns having either modern detailing requirements or excessively poor detailing as compared to Oregon bridges. Moreover, a recent study by Dusicka, et al. (2015) reveals the somewhat unexpected better performance of Oregon bridges under earthquake loading. Hence, to understand the seismic performance of typical bridges in Oregon, deliberate data extraction is necessary to define the structural components with typical dimensions and detailing for bridges in Oregon.

3.2 OREGON BRIDGE INVENTORY

The National Bridge Inventory (NBI) database provides information about all bridges in United States of America (USA) with a span length of more than 20 ft. This database allows for general classification of bridges based on different information contained in 134 fields, referred to as items, in the NBI. In NBI Item 43, bridges are classified based on superstructure materials (Table 3.1), predominant type of design and/or type of construction (
Table 3.2), and number of spans. The coding guide for the Oregon Bridge Inventory and Appraisal serves as a guide to the NBI and lists superstructure materials and types of construction.

Table 3.1: Kind of Material and/or Design, NBI Item 43A (FHWA, 1995)

Description	
Concrete	Prestressed Concrete Continuous
Concrete Continuous	Wood or Timber
Steel	Masonry
Steel Continuous	Aluminum, Wrought Iron or Cast Iron
Prestressed Concrete	Other

Table 3.2: Type of Design and/or Construction, NBI Item 43B (FHWA, 1995)

Description		
Slab	Truss – Deck	Movable – Swing
Stringer/Multi-beam or Girder	Truss – Thru	Tunnel
Girder and Floor Beam System	Arch – Deck	Culvert
Tee Beam	Arch – Thru	Mixed Types
Box Beam or Girders – Multiple	Suspension	Segmental Box Girder
Box Beam or Girders – Single or Spread	Stayed Girder	Channel Beam
Frame	Movable – Lift	Other
Orthotropic	Movable – Bascule	

According to the 2014 NBI database, there are 8052 bridges and culverts in the state of Oregon. Among these, 3877 are multi-span bridges and 1802 of these bridges are owned by state agency, state park, forest or reservation agency, or other state agency. However, the number of state highway owned multi-span bridges built before the year 1990 is 1539. This research focuses on state-owned multi-span bridges in Oregon built prior to 1990, which are listed in Table 3.3.

Table 3.3: Classification of Multi-span Bridges in Oregon Built Prior to 1990, based on NBI item 43

Bridge Type	Number of Bridges 2014 Data
Prestressed Concrete Slab (PC Slab)	116
Concrete Continuous Stringer/Girder (CC SG)	448
Prestressed Concrete Stringer/Girder (PC SG)	210
Wood or Timber Stringer/Girder (Wood SG)	43
Concrete Continuous Slab (CC Slab)	133
Concrete Continuous Frame (CC Frame)	2
Concrete Continuous Multiple Box Beam (CC Multi-BB)	131
Steel Stringer/Girder (Steel SG)	46
Steel Continuous Stringer/Girder (SC SG)	67
Concrete Stringer/Girder (Concrete SG)	44
P/S Concrete Continuous Stringer/Girder (PC Continuous SG)	69
P/S Concrete Continuous Multiple Box Beam (PC Continuous Multi-BB)	75
Concrete Channel Beam (Concrete CB)	38
Steel Continuous Multiple Box Beam (SC Multi-BB)	16
Prestressed Concrete Multiple Box Beam (PC Multi-BB)	6
Steel Truss - Thru	9
Steel Continuous Girder – Floorbeam (SC GF)	10
Concrete Continuous Girder – Floorbeam (CC GF)	9
Steel Truss - Deck	9
Steel Continuous Frame (SC Frame)	12
Concrete Arch – Deck (CA Deck)	1
Other	45
Total	1539

The graphical representation of Table 3.3 is presented in Figure 3.1. It can be seen from Figure 3.1, concrete continuous stringer/girder bridges (CCSG) is the most common type of bridge in the state of Oregon.

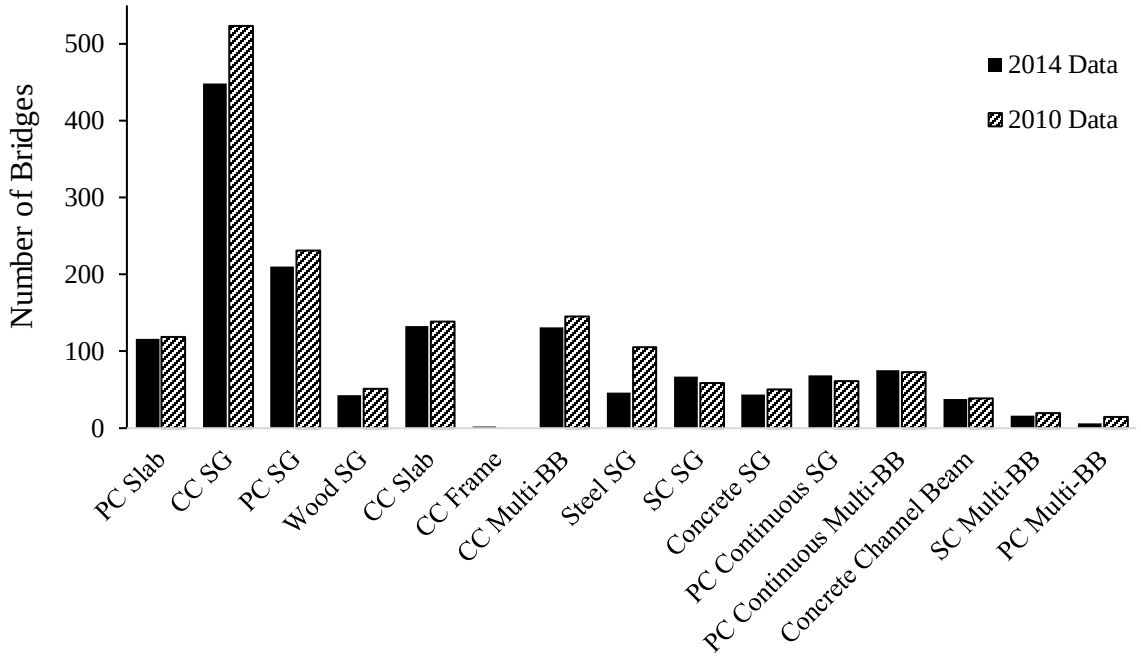

Figure 3.1: Classification of Oregon bridges

3.3 BRIDGE CHARACTERISTICS

The NBI provides different information about the bridges such as year built, number of traffic lanes carried on the structure, design load, maximum span length, deck width, condition rating of the structure etc. However, detailed drawings for each of the bridge classes are necessary to extract typical details for each bridge classes. Thus, the following part of this chapter focuses on the most common bridge characteristics for concrete continuous stringer/girder bridges (CCSG) bridges in Oregon built prior to 1990.

Probability mass functions (PMF) were generated for discrete variables to determine the most common characteristic. PMF is defined as the probability that a discrete random variable, X takes on a particular value x, or $P(X = x)$. For continuous variables, cumulative distribution functions (CDF) were computed. CDF gives the probability that a continuous variable, X takes a value less than or equal to x, or $P(X \geq x)$.

3.3.1 Number of Spans, NBI Item 45

For this case, the number of CCSG bridges with equal number of spans was grouped together and then each group was divided by the total number of CCSG bridges. Figure 3.2 shows the PMF for number of spans.

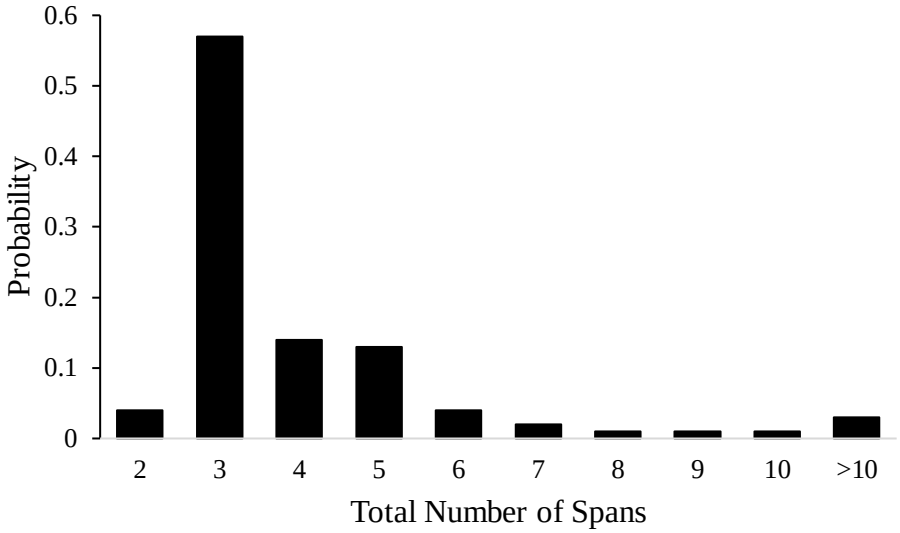

Figure 3.2: PMF for number of spans of CCSG bridges built prior to 1990

As can be seen from Figure 3.2, more than 50% of the bridges have three spans. Hence, it can be assumed that the most representative CCSG bridges is a three-span bridge.

3.3.2 Number of Lanes, NBI Item 28A

The PMF for the number of lanes on the structure was also generated and is presented in Figure 3.3. It can be observed from Figure 3.3 that over 80% of the CCSG bridges have two lanes on the main unit of the structure.

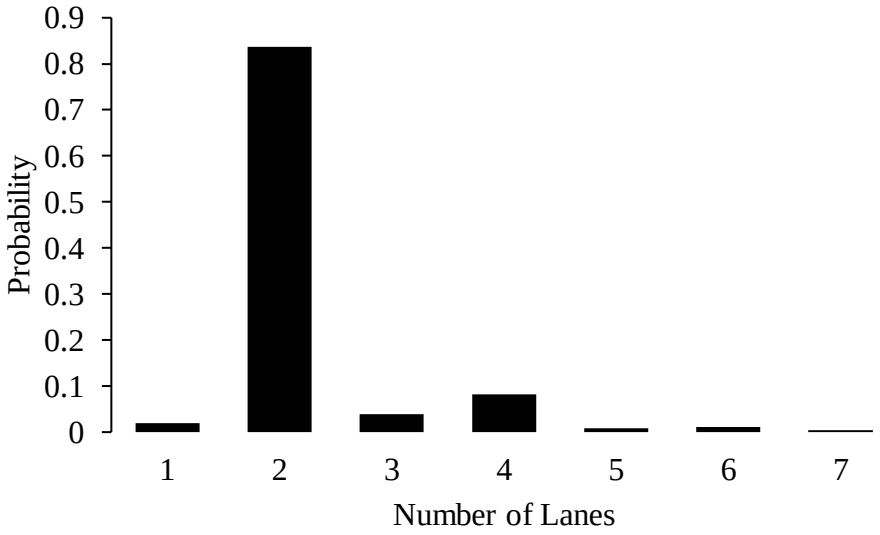

Figure 3.3: PMF for number of lanes of multi-span CCSG bridges built before 1990

3.3.3 Length of Bridge, NBI Item 49

The total length of the bridges can be found from the NBI database and an empirical cumulative distribution function (CDFs) for the total length of the bridges are useful to describe the distribution for bridge length of CCSG bridges. Figure 3.4 represents the CDF for the total length of the bridges. The average total length was found to be 176.5 ft with a standard deviation of 108.5 ft and a median value of 150 ft. In addition to the cumulative distribution function, the range of length for CCSG bridges are presented in Figure 3.5 using 20-foot bins. This shows the maximum of the bridges have span length between 120 ft – 140 ft.

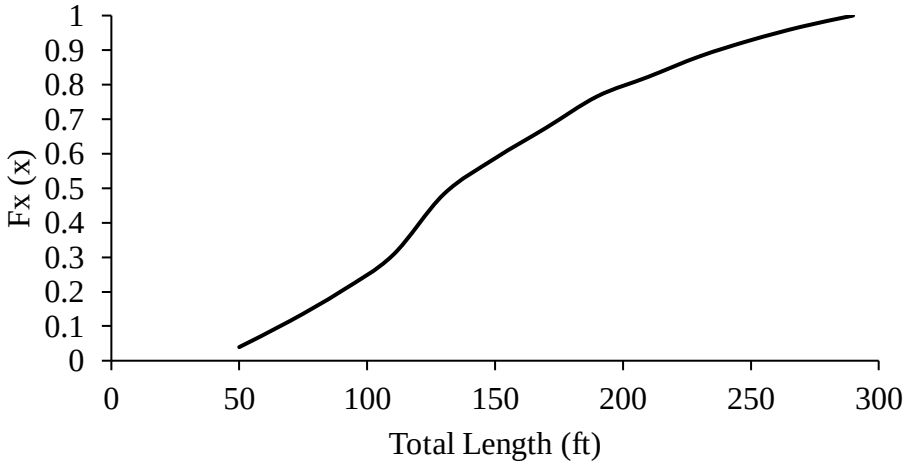

Figure 3.4: Cumulative distribution function for bridge length

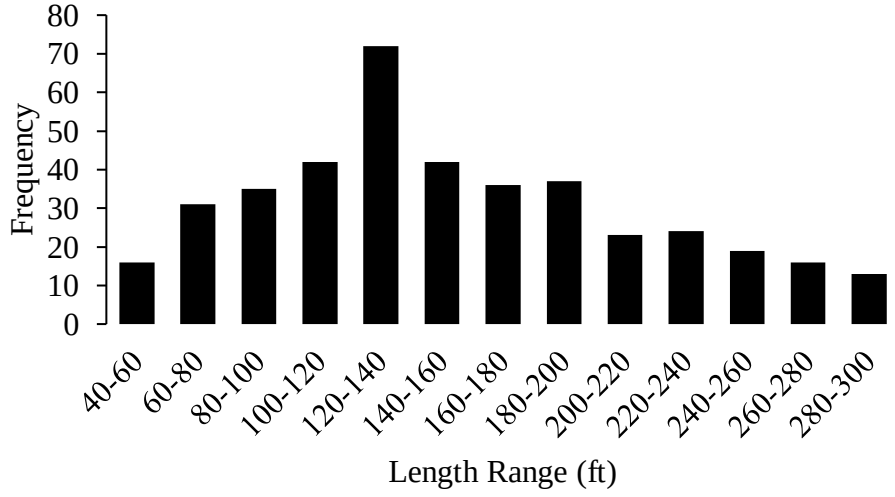

Figure 3.5: Frequency plot for bridge length of multi-span CCSG bridges built before 1990

3.4 TYPICAL BENT CHARACTERISTICS

The individual components of a bridge bent consist of columns, foundation, and cross beam. Geometric and reinforcing details for all of the components are of significant importance for seismic performance evaluation of a bridge substructure system. Hence, a detailed analysis from 113 available bridge drawings for concrete continuous stringer/girder bridges were conducted to establish the most representative bent details. The following sub-sections present the results obtained from the statistical data analysis for typical bent characteristics.

3.4.1 Number of Columns per Bent

The frequency of bridges with certain number of columns per bent as extracted from the available drawings for CCSG bridges are presented in Figure 3.6. It should be mentioned that only the intermediate bents were taken into consideration for counting the number of columns per bent.

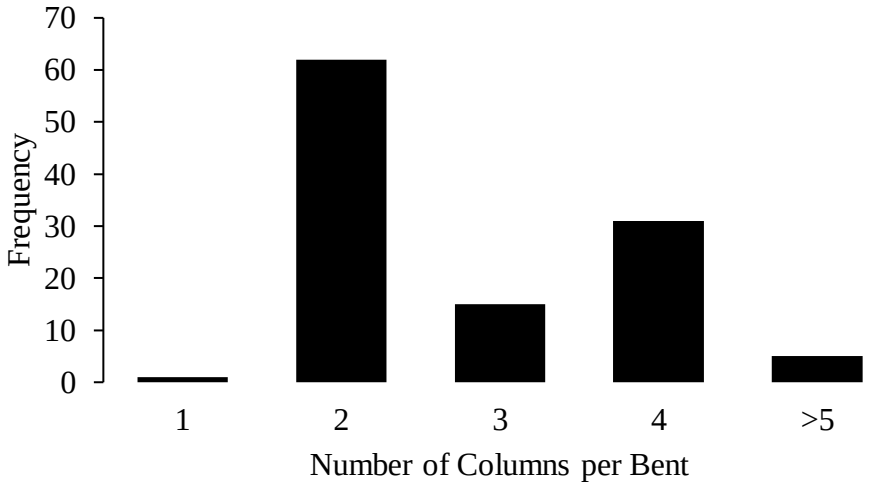

Figure 3.6: Number of columns per bent for multi-span CCSG bridges built before 1990

It was found that most of the CCSG bridges consist of multi-column bents as the substructure. Further investigation shows that almost 60% of all multi-column bridge bents have two columns per bent.

3.4.2 Column Height

Column height is one of the important parameters in this research as it greatly affects the earthquake response for bridge structures. Unfortunately, column height data are not tabulated in the NBI database and hence were extracted from the available bridge drawings. In many cases, column heights for end bents and intermediate bents differ greatly and are thus recorded separately. Figure 3.7 represents the frequency of CCSG bridges over a particular range of column heights for intermediate and end bents for bridges built before 1990. As can be observed, typical heights for intermediate bents are within a range of 20 ft. – 25 ft. However, the typical range of column heights for end bents are in the range of 15 ft. – 20 ft.

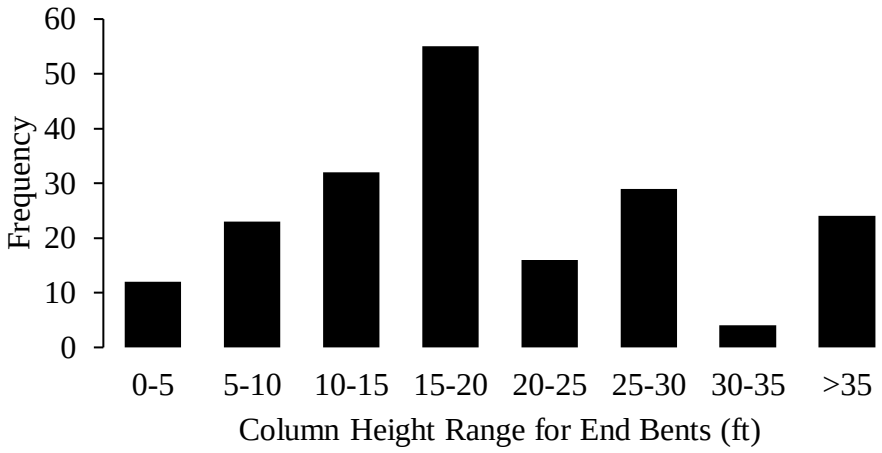

(a)

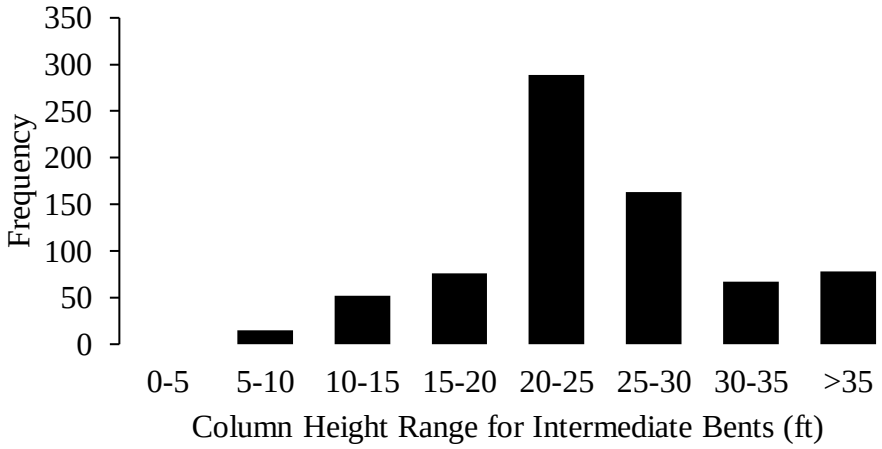

(b)

Figure 3.7: Variation of column heights for multi-span CCSG bridges built before 1990 (a) for end bents and (b) for intermediate bents

3.4.3 Column Details

Column details (i.e. cross sectional dimensions, reinforcement detailing, splice length etc.) were extracted from the available bridge drawings in order to reproduce a typical bent column for CCSG bridges in Oregon. From the data extracted, a typical bent for a CCSG bridge has a square concrete column with cross sectional dimensions of 24 in x 24 in. Most of the bridges have four longitudinal reinforcement bars in the column section. Further investigation shows that the majority of the columns with four longitudinal reinforcement bars have either #8 or #10 rebar as the longitudinal reinforcement. The transverse reinforcement is typically provided by #3 hoops (65% of the cases) with a center-to-center spacing of 12 in throughout the column height. The same longitudinal bars are spliced with the foundation reinforcement having a total length of 6 ft. – 7 ft. The majority of the columns have a concrete cover of two in. The cross sectional and elevation drawings of a typical column is presented in Figure 3.8.

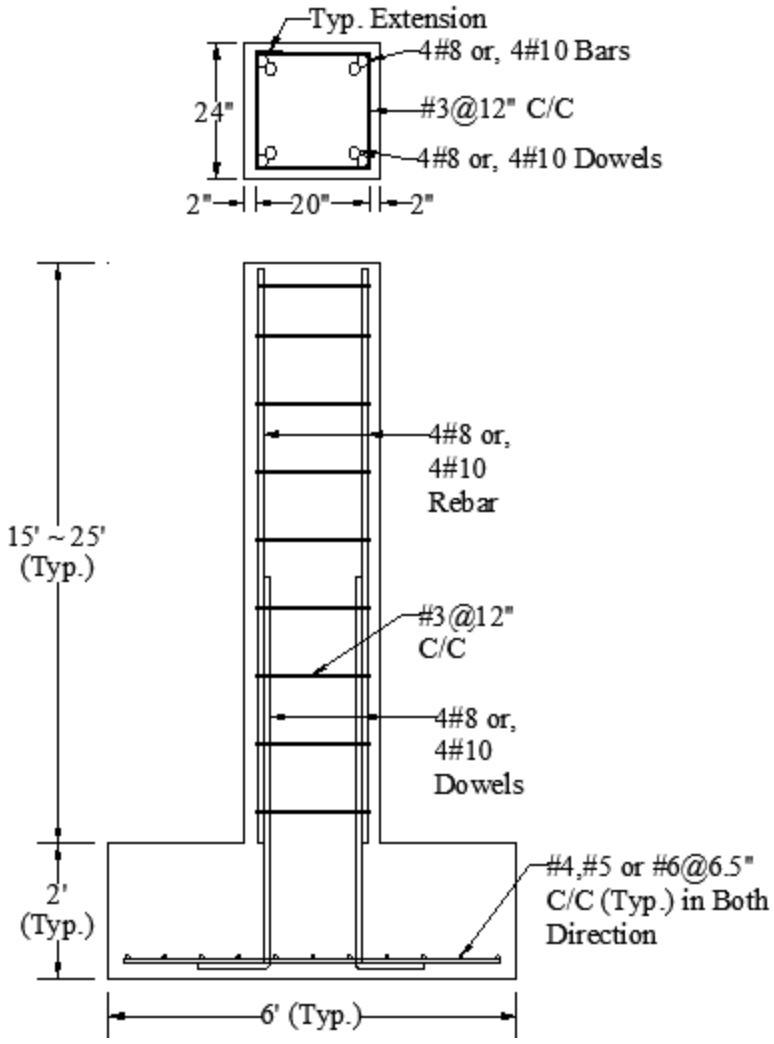

Figure 3.8: Cross section and elevation view of typical column-footing details

3.4.4 Splice Length

Most of the bridge columns have lap splices in the foundation-column joint region, which has a profound impact on the seismic performance of the bridges. Hence, a detailed screening based on the available drawings were conducted to investigate the variation of lap splice lengths for typical bridge columns. It was found that the splice length varies with the diameter of longitudinal reinforcement and hence only the splice length variation for #8 rebar is reported here, as #8 rebar are used as the longitudinal reinforcement in the test specimens of this research. Figure 3.9(a) shows the distribution of splice length multipliers (numerical multiplier with respect to diameter of the longitudinal rebar) and Figure 3.9(b) shows the cumulative percentage distribution for the splice length variation.

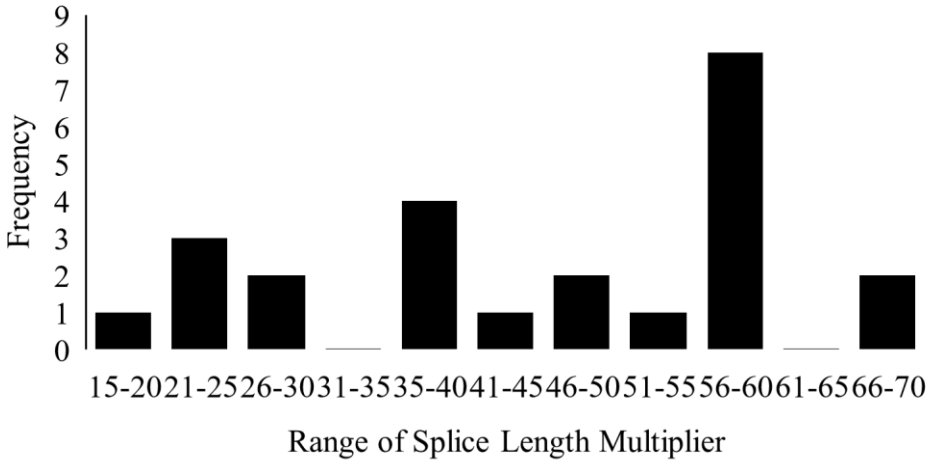

(a)

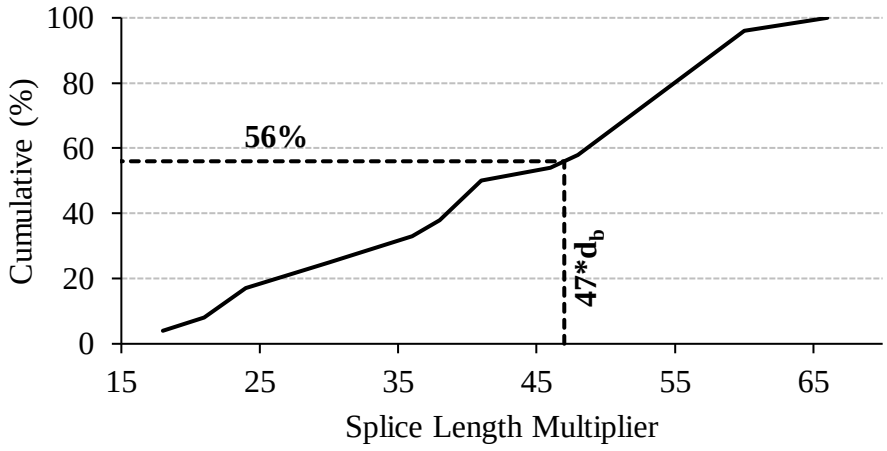

(b)

Figure 3.9: (a) Variation of splice length multiplier for #8 splice bars and (b) Cumulative percentage changes for splice length multiplier

3.4.5 Foundations Details

The majority of multi-span CCSG bridges with square concrete columns have a square/rectangular spread footing as the foundation. The cross sectional dimensions of the footings range from 6 ft. to 8 ft. (square spread footing) and for more than 50% of the cases the depth of the footing is 2 ft. Reinforcement detailing for the spread footing consists of only one bottom layer of reinforcement (in two directions) consisting of #4, #5, or #6 reinforcing bars. However, #5 reinforcing bars are most common and an investigation for the spacing of reinforcement with #5 rebar shows that majority of the foundations have a spacing of 6" – 7" (over 50% of the cases) in both directions. Figure 3.8 shows the elevation view of the foundation and the plan view is presented in Figure 3.10.

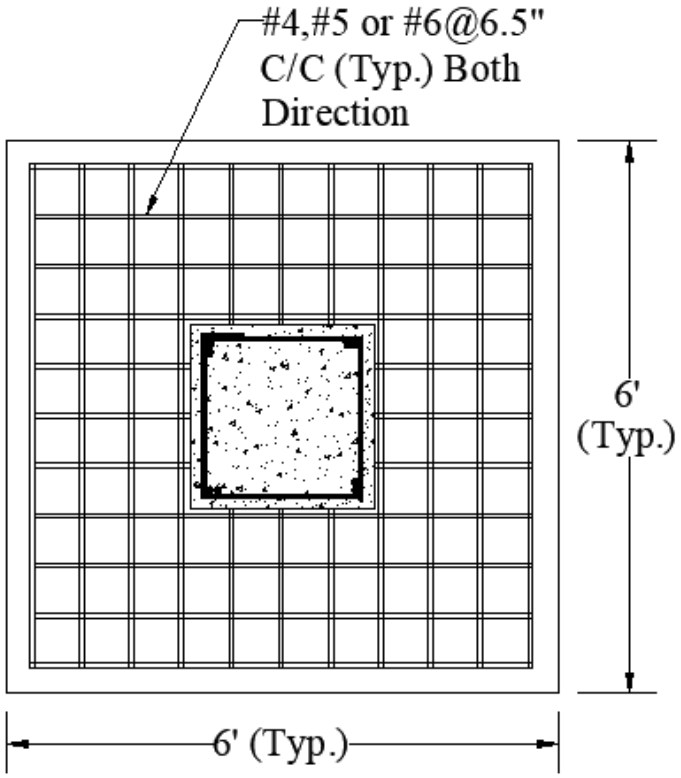

Figure 3.10: Plan view of a typical foundation reinforcing detail

3.4.6 Crossbeam Details

Typically, a crossbeam has a sectional depth of about 5-6 ft. and a width of 1.25 ft. - 2 ft. The longitudinal reinforcement used typically consists of #9, #10, or #11 rebar separately or in combination with each other. Most of the cross beams have #4 or #5 U-stirrups with a spacing of 6" – 9" near the column support and 12" – 15" in the mid-section. The concrete cover for the beam section is 2 in for the majority of cases. However, it should be mentioned that defining a typical crossbeam section is not justified because of the large variability of their cross sectional detail.

3.5 SUMMARY

A statistical data analysis of available data from the National Bridge Inventory (NBI) and the Oregon Department of Transportation (ODOT) were conducted to establish typical details for Oregon bridges built prior to 1990. Concrete Continuous Stringer/Girder (CCSG) bridges were found to be the most common bridge type in the state of Oregon. Further investigation established typical characteristics, i.e. number of spans, number of lanes on the bridge, length of bridges, etc. for CCSG bridges. It was found that a typical CCSG bridge has three spans with an average span length between 120ft – 140ft. In addition, the main unit of the structure usually has two lanes on the bridge.

A total of 113 bridge substructure drawings available from ODOT were studied to establish typical bridge bent characteristics including number of columns per bent, column height, and

geometry and reinforcing details for different components of the substructure, i.e. column, foundation, and cross beam. Multi-column bridge bents are the most common type with an average column height of 15ft – 25ft. Finally, sectional details and other design specific parameters were investigated and typical bent details for the most common bridge substructure components in the state of Oregon were developed. It was found that a square reinforced concrete column with a square spread footing having a single layer of reinforcement at the bottom is most common. Most of the columns have a lap splice reinforcing arrangement in the plastic hinge zone with a moderate splice length, which makes it substandard for earthquake-type loadings. In addition, the transverse reinforcement spacing lacks the seismic detailing requirements as per current seismic design practice.

4.0 EXPERIMENTAL PROGRAM

4.1 GENERAL

The following sections describe the experimental program for the tested reinforced concrete bridge column-footing subassemblies subjected to reverse cyclic lateral loading. Test setup, design & detailing, and construction of specimens are presented as well. Finally, specimen external and internal instrumentation along with the loading protocol used for the study are presented.

The experimental program was designed to study the behavior of a full-scale reinforced concrete bridge column-footing subassembly, measure local and global response quantities, and provide experimental evidence of different damage levels under longer duration shaking expected from a CSZ event.

4.2 TEST MATRIX

The experimental program was designed to investigate the performance limit states of substandard square RC bridge columns commonly found in the state of Oregon. Representative bridge bent details were formulated for the experimental research program and the test matrix was then developed based on the variables considered. The test matrix as shown in Figure 4.1 consists of three full-scale bridge column-footing subassemblies. The two main variables considered for the test matrix were (1) lateral displacement history and (2) axial loading history. In order to investigate the effect of axial loading variation, two sets of specimens were tested with constant and variable axial loading history when all other parameters (i.e. geometry, reinforcement and lateral displacement history) were kept constant. This is designated as "Test Series I" and are placed in the columns of the test matrix whereas the second test series is contained in the rows of the test matrix. The second series of test "Test Series II" investigates the effect of lateral displacement history on strain limit states for the bridge columns. Two sets of lateral loading protocol were used while keeping all other parameters identical. Table 4.1 summarizes the details of the test specimens included in the test matrix.

Each of the columns in the test matrix were assigned a name starting with three letters followed by a hashtag and a number (i.e. SCF#8). The first letter was either S or L, designating the lateral loading protocol (S – Subduction Zone Lateral Loading Protocol and L – Standard Laboratory Loading Protocol). The second letter of the nomenclature designates the axial loading protocol, which is either C (constant) or V (variable) and the last letter specifies the sub-assembly type. All three cases were column-spread footing subassemblies and hence are designated as F (footing). The last part of the name has a hashtag and a numerical value that represents the longitudinal reinforcement used for the specimen. All three specimens were built with 4 - #8 longitudinal reinforcing bars and have thus a designation of "#8" at the end.

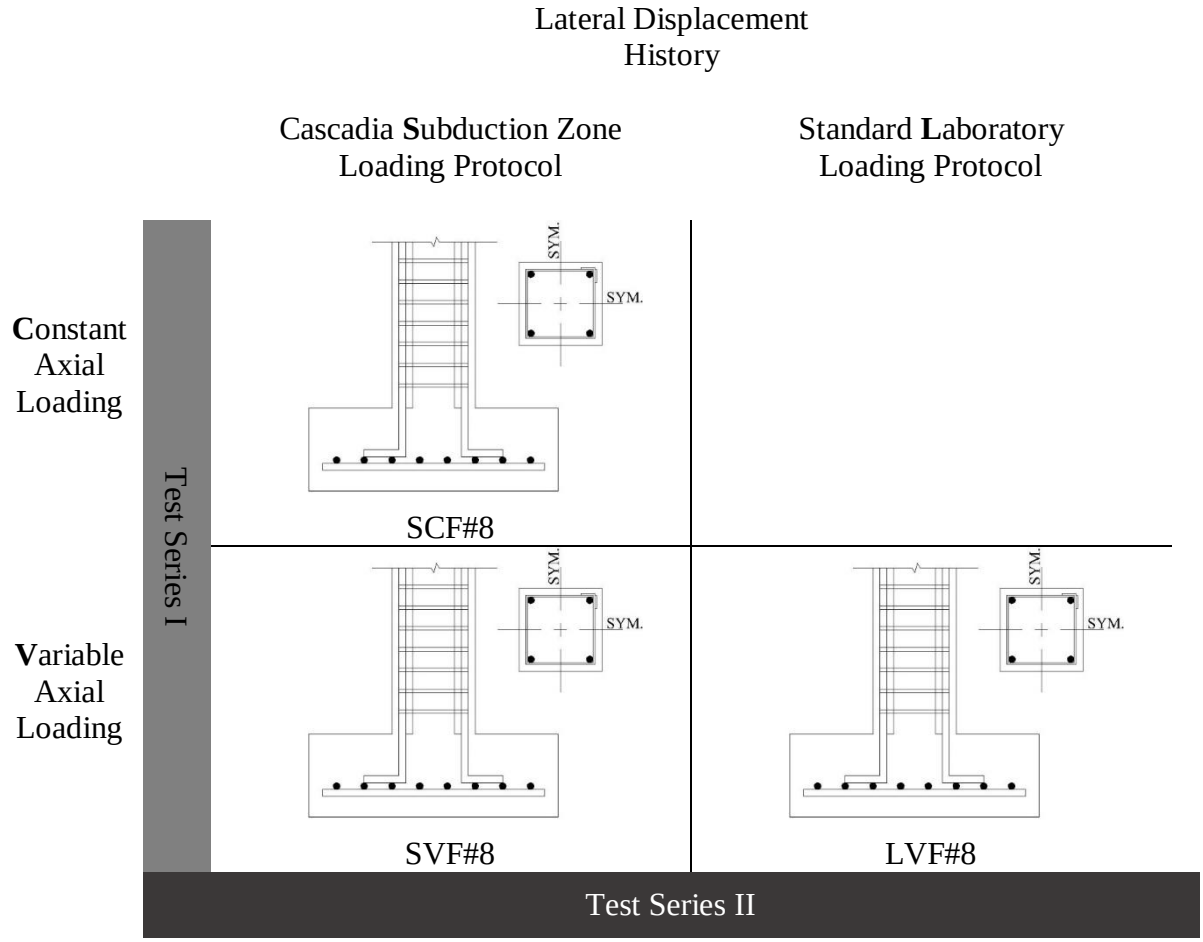

Figure 4.1: Test matrix

The first specimen in the test matrix (top row in the first column) has been designated as SCF#8, indicates that the specimen was a column-spread footing subassembly with 4 - #8 longitudinal reinforcing bars. The specimen was tested under subduction zone lateral loading protocol while the axial load was constant. The second specimen of "Test Series I" designated as SVF#8 has similar geometric and reinforcing detail with variable axial loading protocol while the lateral loading protocol was the same as SCF#8 (subduction zone loading protocol). The second specimen (SVF#8) was accounted into both test series I and test series II. The third specimen (LVF#8) was included in the test series II having different lateral loading protocol while keeping the same axial loading protocol as SVF#8.

Table 4.1: Test Specimen Details

Test	Specimen Designation	Lateral Load History	Axial Load History	Aspect Ratio (L/D)	Steel Content (ρ_l)	*Transverse Steel Details (ρ_s)	**$P/(f'c*A_g)$
1	SCF#8	Subduction	Constant	3.75	0.62%	#3 at 12" (0.17%)	9%
2	SVF#8	Subduction	Variable	3.75	0.62%	#3 at 12" (0.17%)	Min-6% Max-9%
3	LVF#8	Standard Laboratory	Variable	3.75	0.62%	#3 at 12" (0.17%)	Min-6% Max-9%

*The volumetric ratio of the transverse reinforcement for a square column section was calculated as $\rho_s = 4*A_v / (h_c*S)$ where A_v = Area of transverse reinforcement, h_c = Depth of core column concrete and S = Spacing of the transverse reinforcement.
**The axial load ratio was calculated considering the 28-day strength (4.74 ksi) of the column concrete.

4.3 GEOMETRY AND REINFORCEMENT

The geometry and reinforcing details of all the three foundation-column subassembly test specimens represents the critical portion of a typical multi-column bridge bent of concrete continuous stringer/girder bridges in Oregon. The 24-inch square column was reinforced with 4 - #8 longitudinal rebar on the four corners. Column longitudinal reinforcement bars were extended to the column-footing joint face and were then developed into the foundation through a lap splice with # 8 dowel bars. The lap splice length for the dowel bars starting from the column-footing joint was 47 inch, which is equivalent to $47*d_b$ (d_b = diameter of the longitudinal reinforcing bar). The spliced bars were developed to the top layer of the foundation slab reinforcement with a 90-degree bend at the end and then extended to 12 inch, which is equivalent to 12 rebar diameters.

The transverse reinforcement consists of #3 square tie bars with 90-degree hooks at both ends with an extension of 10 times the diameter of the tie bars (4½ inch). The concrete clear cover from the external face of the tie bars to the face of the column cross section was 2 inch for all specimens. The first tie at the bottom of the column region is located 6 inch from the column-footing joint, with subsequent ties spaced at 12 inch. However, the tie bars in the top 19¼ inch of the column were spaced at only 3 inch to provide better concrete confinement of the core concrete and hence to negate any possibility of concrete crushing due to close proximity of axial load application over the top of the column. The hooks of the tie bars were placed in opposite corners alternatively to prevent weak spots in any column corner.

The 6 x 6 ft square foundation has only a bottom layer of reinforcement in two orthogonal directions with a concrete clear cover of 3 inch from the face of the bottom layer reinforcement. All the bars used for the foundation reinforcement are #5 bars and are spaced at 6½ inch in both directions. The deformed bars were laid flat in the foundation without any hook or any extension upward. Details of the column-footing sub-assemblies are presented in Figure 4.2.

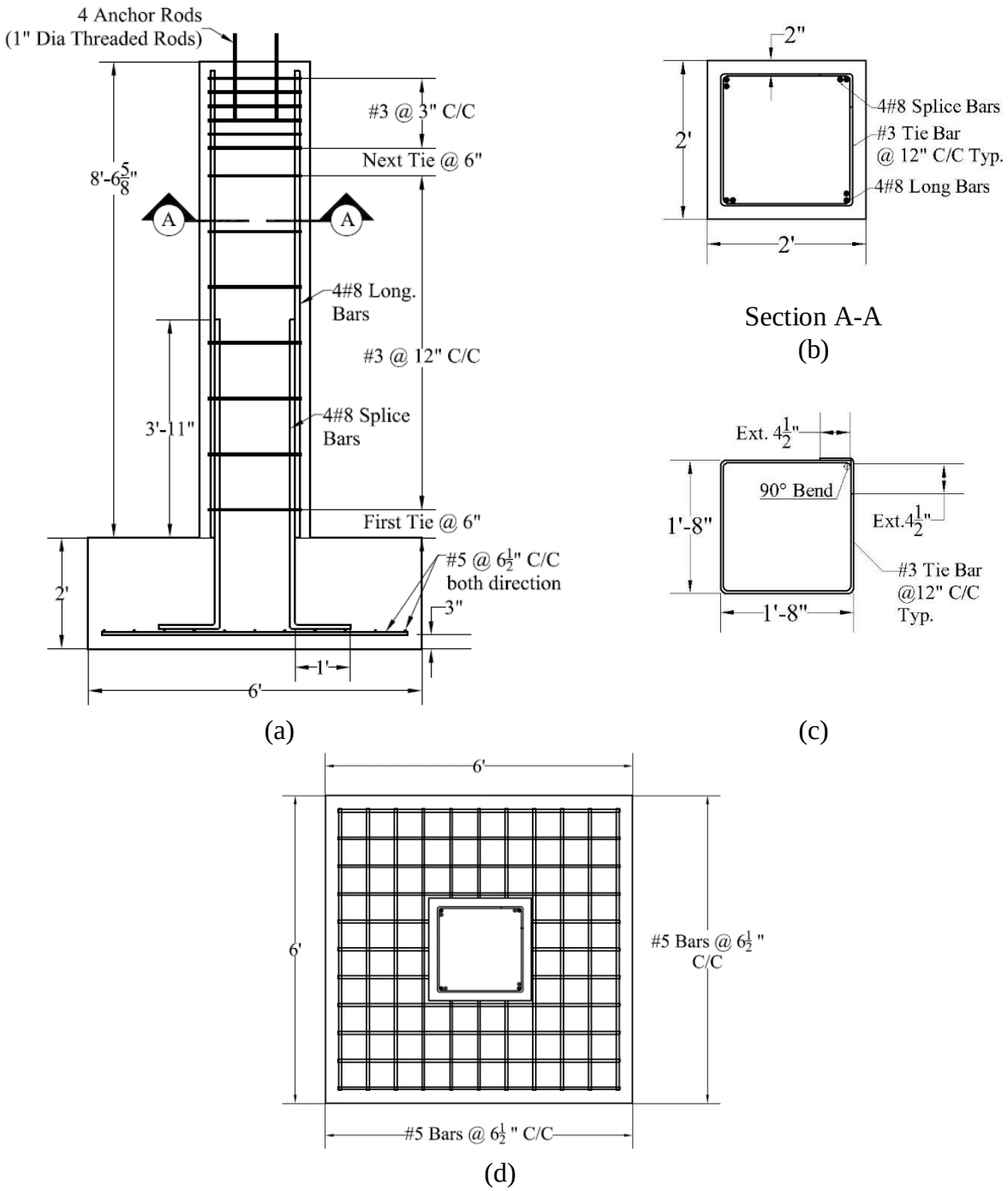

Figure 4.2: (a) Column-footing longitudinal section details (b) Column cross sectional details (Section A-A), (c) Tie bar details, (d) Foundation cross section details

4.4 MATERIAL PROPERTIES

The specimens were built using a normal weight normal strength concrete and Grade 60 deformed steel bars. The specification for the material properties as obtained from the available bridge drawings were 'Class A' concrete mix with intermediate Grade 40 steel reinforcing bars.

However, due to the unavailability of Grade 40 reinforcing bars, Grade 60 bars were used for the specimen construction.

4.4.1 Steel

ASTM (ASTM International 2018) Grade 60 deformed steel reinforcing bars were used for the construction of the specimens. In order to obtain the mechanical properties of the reinforcing bars, 36-inch-long test bars from each size and batch were tested under uniaxial tensile loading following the ASTM (ASTM International, 2019) standard. The test results are summarized in Table 4.2.

Table 4.2: Rebar Tensile Strength Result

Specimen	Diameter (inch)	Yield Strength (ksi)	Tensile Strength (ksi)
#8 (Long. Rebar)	1.00	69.4	96.5
#5 (Footing Rebar)	0.625	70.7	109
#3 (Tie Rebar)	0.375	75.6	105

4.4.2 Concrete

The expected 28-day nominal concrete compressive strength was 3300 psi. Due to the bulk volume of concrete, ODOT specified concrete was ordered from the ready-mix concrete company. 3311BVR (3300 psi) concrete mix design uses maximum ¾ inch aggregate size with a 4 inch slump. The water cement ratio for the ordered concrete mix was 0.47.

The concrete compressive strength for an individual concrete batch was determined through standard cylinder tests following ASTM (ASTM International 2020). 6 x 12 inch concrete cylinders were tested at 7, 21, 28, and on or near each test day. Three samples were tested for each test day and the average concrete compressive strength rounded to nearest ten was reported. The summary of the concrete compressive strength result are presented in Table 4.3.

Table 4.3: Concrete Compressive Strength Test Result

Specimen	Age (days)				
	7-Day	21-Day	28-Day	Test Day 2 (F-202/C-151)	Test Day 3 (F-286/C-234)
Footing Concrete (psi)	3,320	4,910	5,410	6,410	6,610
Column Concrete (psi)	3,340	-	4,740	5,880	5,790

Concrete cylinder compressive strength vs. age of concrete cylinder are plotted in Figure 4.3 (a) and (b). 28-day compressive strength for column and footing concrete were 4,740 psi and 5,410 psi, respectively. It can be seen from Figure 4.3(a), 7-day strength of both the column and footing concrete were comparable (≈ 3300 psi) and was almost the same as the expected 28-day nominal concrete compressive strength. However, a linear increase in compressive strength for both the column and footing concrete was observed up until the 28-day strength. It can also be observed that the 28-day compressive strength of the footing concrete was higher than the one for column concrete. This can be attributed to the different batches of concrete mix design and variations in water content between footing and column concrete. However, post 28-day

strength gain rate for the column concrete was almost twice the one for footing concrete [Figure 4.3(b)].

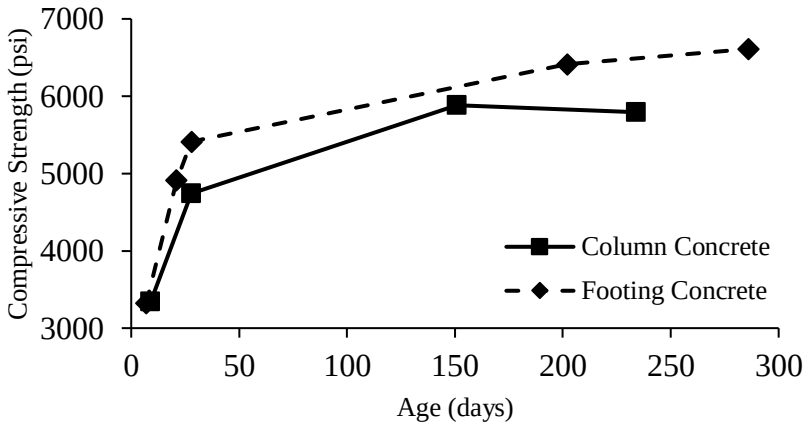

(a)

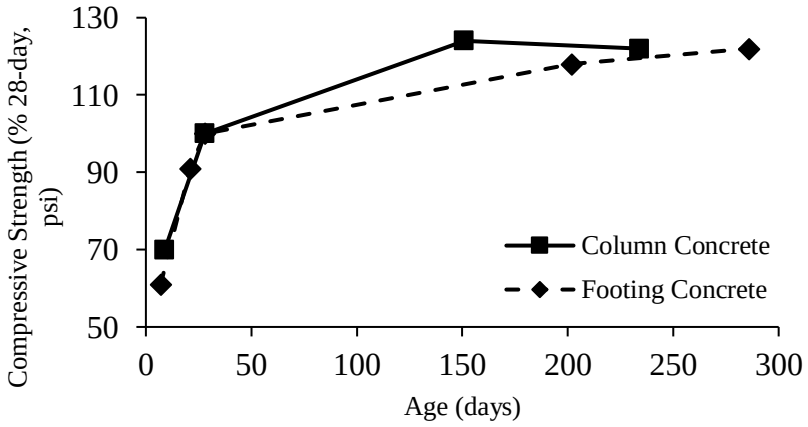

(b)

Figure 4.3: (a) Average concrete compressive strength vs. age of cylinder and (b) Average concrete compressive strength as percentage of 28-day strength vs. age of concrete

4.5 SPECIMEN CONSTRUCTION

All specimens were constructed in the iSTAR Laboratory at Portland State University and caution was taken to replicate the exact prototype column-footing subassemblies as described in Section 4.3. However, formwork for one of the specimens failed in the bottom corner during casting, which resulted in a slightly larger cross sectional area in that corner of the specimen. After removing the forms, reinforcement alignment and position of the transverse reinforcement were checked and found to comply with the detailing of the column specimen. Hence, only the concrete clear cover was increased due to the opening of the formwork in that corner. The

construction sequence of the specimen includes formwork preparation, rebar cage construction, instrumenting the rebar with foil strain gauges, placing the rebar cages in place, concrete casting and finally removing the forms off the specimens.

Concrete casting was done in two phases, starting with the casting of the foundation portion of the specimens. All three of the foundation specimens were cast at once and hence the same concrete mix was used. The ready mix concrete was provided by a local supplier with a truck that directly placed concrete via shoot into the forms. Workability of the concrete was measured through slump test and was recorded as 5 inch. The columns were cast in the second stage of construction with a similar concrete mix as used for the foundation construction. However, the column concrete was found to have higher workability than the foundation concrete.

4.6 TEST SETUP

The quasi-static reverse cyclic lateral load was applied at the column top (Figure 4.4.) using a servo-controlled hydraulic actuator with a maximum capacity of 220 kip in tension and 335 kip in compression. The maximum stroke length of the lateral actuator is ±10 inch. The lateral reverse cyclic load was applied in displacement-control mode. Built-in load cells were used to monitor applied load and displacement of the lateral actuator during the test. The column top was free to rotate and translate while undergoing the lateral displacement cycles.

Constant and variable axial loads were applied to the column to simulate the self-weight of the superstructure. The axial load was applied using a lever arm concept where the initial force was generated with an actuator oriented in vertical position (Figure 4.4.). The servo-controlled vertical actuator, having a maximum capacity of ±100 kip and a maximum stroke length of ±6 inch, was used for generating the axial force. In order to maintain the accurate load values, the vertical actuator was operated in force-controlled mode.

In addition to the lateral and vertical actuators, the test setup comprised of several different components, including a reaction frame supporting the lateral actuator, load transfer beams, and tension anchor rods. The detailed test setup is illustrated in Figure 4.4.

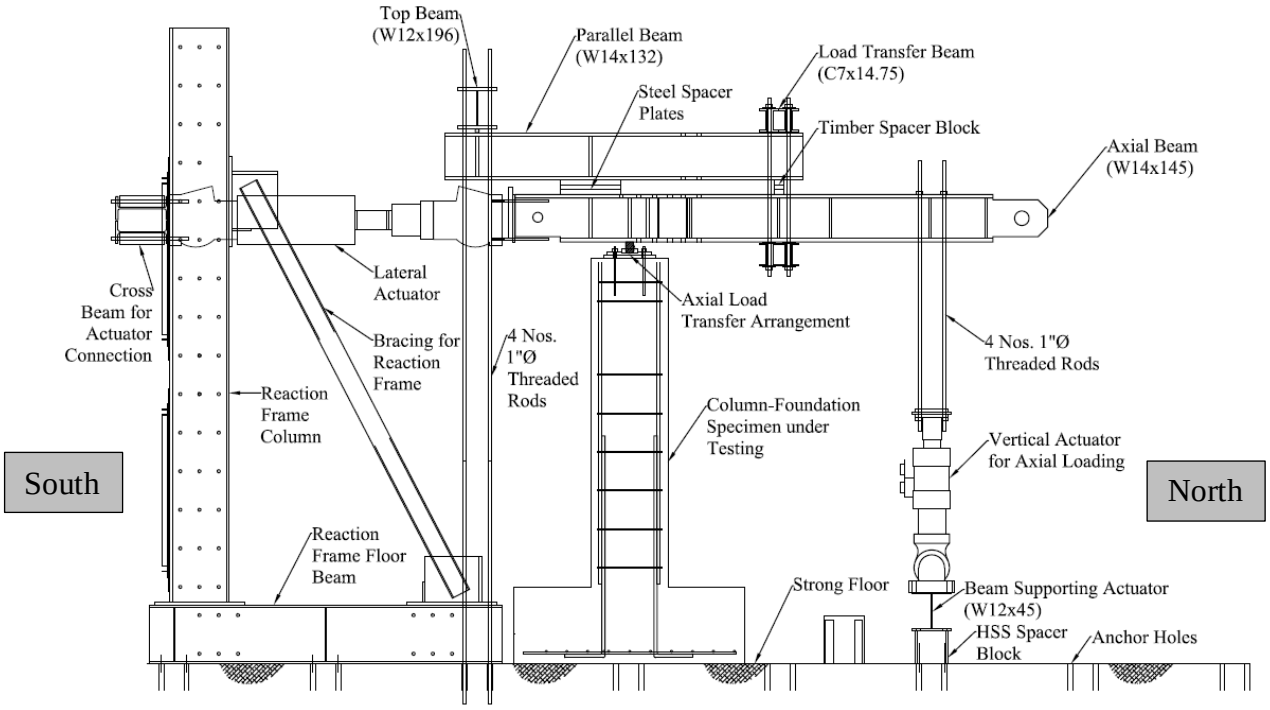

Figure 4.4: Elevation view of test setup

The reaction frame consisted of two column (W18x97) section resting on two floor beams (W18x97). The reaction frame column has holes spaced every 12 inch to facilitate the lateral actuator connection through a crossbeam. Two steel HSS diagonal braces were placed on the reaction frame as part of the load transfer mechanism. The floor beam of the reaction frame was post-tensioned and anchored to the laboratory strong floor. The lateral actuator was connected to the center of a cross beam, which was connected to the reaction frame column using threaded rods. In addition, the lateral actuator was vertically supported with a temporary wooden frame (not shown in Figure 4.4).

The test setup was designed to have the ability to vary the axial load in the column during the test for two of the specimens. The vertical actuator was placed on its own floor beam (W12x45), which was anchored to the strong floor and post-tensioned. Two Hollow Steel Section (HSS) of 10 inch height were placed between the floor and the beam to provide additional space for the vertical actuator connection with the floor beam. The vertical actuator was connected with the floor beam through four 1½-inch diameter threaded rods. The test setup was also designed to overcome the capacity of the vertical actuator using a lever arm system. The details of the lever arm in the test setup is illustrated in Figure 4.5.

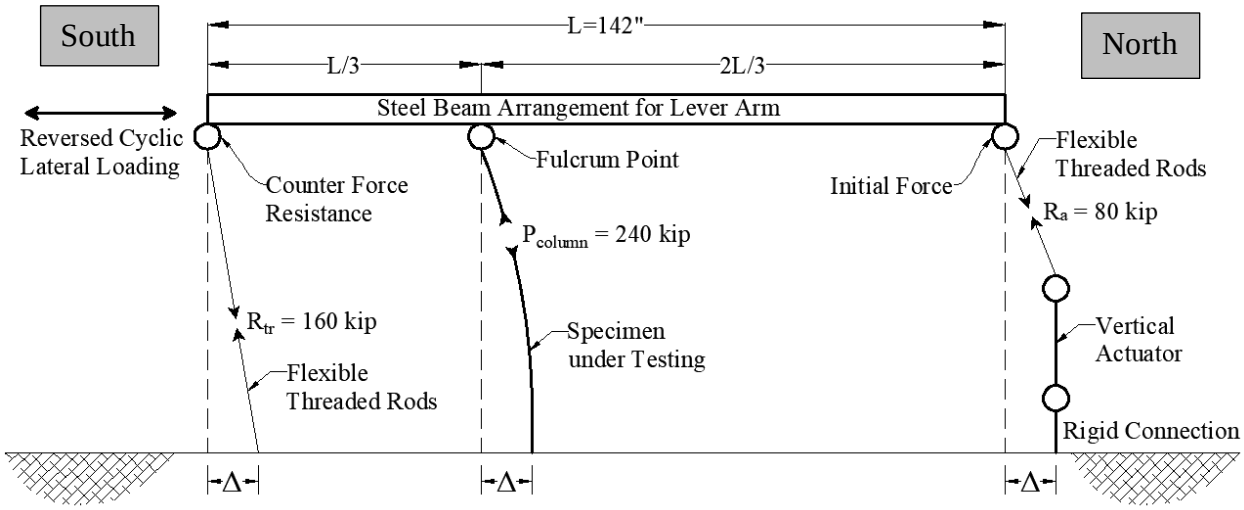

Figure 4.5: Illustration of lever arm arrangement for axial loading

The vertical actuator used for the application of axial load in the specimen column was limited to a maximum of ±100 kip. However, the maximum axial load on the column was determined to be 240 kip, which is significantly higher than the capacity of vertical actuator. Within the lever arm system, the center of the column-footing specimen was positioned at 2L/3 from the vertical actuator and the opposite side was restrained with threaded rods at L/3 distance from the column center point. The column top was acting as the fulcrum point for the lever arm system. Hence, the following maximum forces could exist in the setup:

Vertical actuator tension force, R_a = +80 kip

Reaction (tension) force in threaded rods, R_{tr} = (80*2L/3) / (L/3) = +160 kip

Axial compression load in column, $P_{column} = R_a + R_{tr}$ = -80 kip - 160 kip = -240 kip

The lever arm consisted of a complex beam arrangement as shown in Figure 4.6. "Axial Beam (W14x145)" was mounted on top of the column and connected with the lateral actuator in the south end. In addition, the north end of the "Axial Beam" was connected to the vertical actuator at the south end with threaded rods. A beam parallel to the axial beam was mounted on top of the "Axial Beam" and was used to provide the necessary lever arm length. It is referred to as "Parallel Beam (W14x132). Steel spacer plates of 1-3/4 inch thickness were used on the compression side and wooden lumber on the tension side of the "Parallel Beam" to provide sufficient clearing for the lateral actuator during testing. Once a tension force was applied using the vertical actuator, the two restraint ends of the "Parallel Beam" were in tension whereas the center (at the point of the steel spacer blocks) in compression. In order to achieve composite action between the "Parallel Beam" and the "Axial Beam", the north end of the "Parallel Beam" beam was restrained with a built up section and four threaded rods (two on each side). Figure 4.6, illustrates free body diagrams of the lever arm components. It can be observed that the threaded rods restraint end experiences twice the load generated by the vertical actuator. Hence, at any instant of time, the column top experiences three times the load generated by the vertical actuator, which is again the summation of the force generated by vertical actuator and the resultant resistance at the threaded rods end.

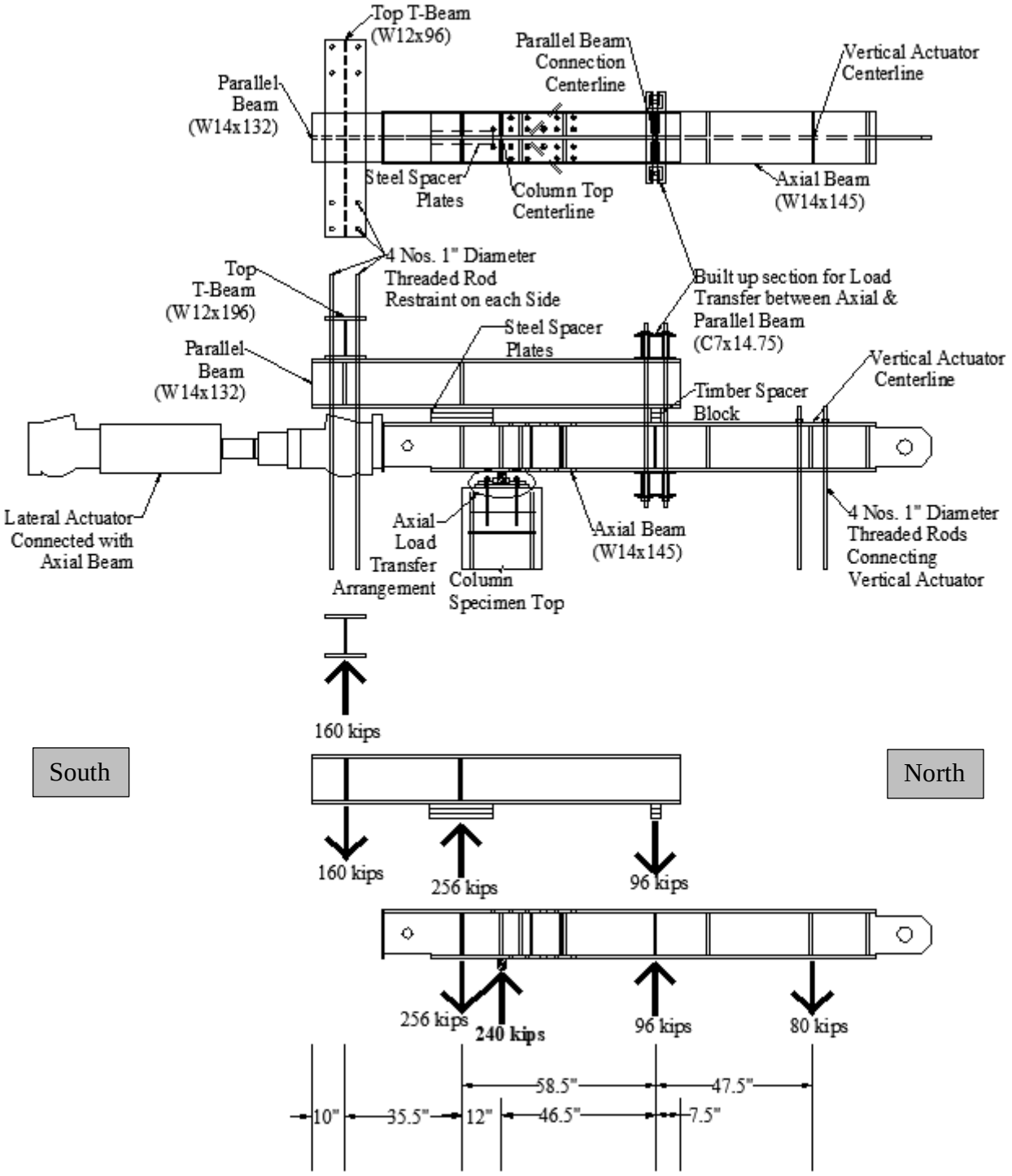

Figure 4.6: Beam arrangement for variable axial load application: Plan view, Elevation view, and Static equilibrium of the system

4.7 INSTRUMENTATION

The system and local behavior of the test specimen was captured using both external and internal sensors. The key global response quantities measured included the lateral column top displacement, column and foundation rotations, foundation uplift and sliding, applied lateral load, and applied vertical loads. The following subsection summarizes the details of the instrumentation employed during the laboratory tests.

4.7.1 Footing Instrumentation

The test specimen consists of a spread footing and column subassembly. Experimental evaluation of seismic performance of the bridge components often focuses only on the behavior of column elements and hence the footing is constructed as a capacity protected member to facilitate the application of lateral loading. In these cases, the footing is usually tied to the strong floor to prevent any deformation (i.e. sliding, rotation, uplift etc.). However, the current experimental program focuses on the behavior of the column-spread footing subassembly. Hence, the spread footing was instrumented with external and internal sensors to capture the global and local deformation response quantities. Details of the external and internal instrumentation used for the spread footing alone are discussed in following subsections.

4.7.1.1 *External Sensors*

The foundation of the specimen rested on the laboratory floor and was allowed to rotate and translate. In order to quantify the movement of the foundation during a test, its uplift and sliding were measured. Along with these, LVDTs were placed on the footing top surface to measure relative deformation to compute concrete compression and curvature demand in the foundation. Figure 4.7 shows the foundation instrumentation details. Two LVDTs were placed vertically and attached at the mid-length of the foundation north and south face to measure any potential uplift. In order to measure the sliding of the foundation, three LVDTs were positioned in the horizontal direction on east, west and north faces. All three LVDTs reacted against a reference aluminum angle section, which was glued to the floor and allowed a relative measurement of sliding with respect to the laboratory strong floor. In addition, five LVDTs were used to measure the foundation's extreme surface concrete compression and curvature along the direction of lateral loading. These LVDTs were also positioned in the horizontal direction to measure the relative displacement for a certain gauge length. To fix these LVDTs, five zinc-coated steel threaded rods of 5/16 inch diameter were embedded 6 inch into the foundation prior to concrete casting. The first threaded rod was placed along the center of the foundation length at a distance of 3 inch from the column face. The next threaded rod was placed at 12 inches (parallel to the column edge) and the next three at 5 inch intervals as shown in Figure 4.7.

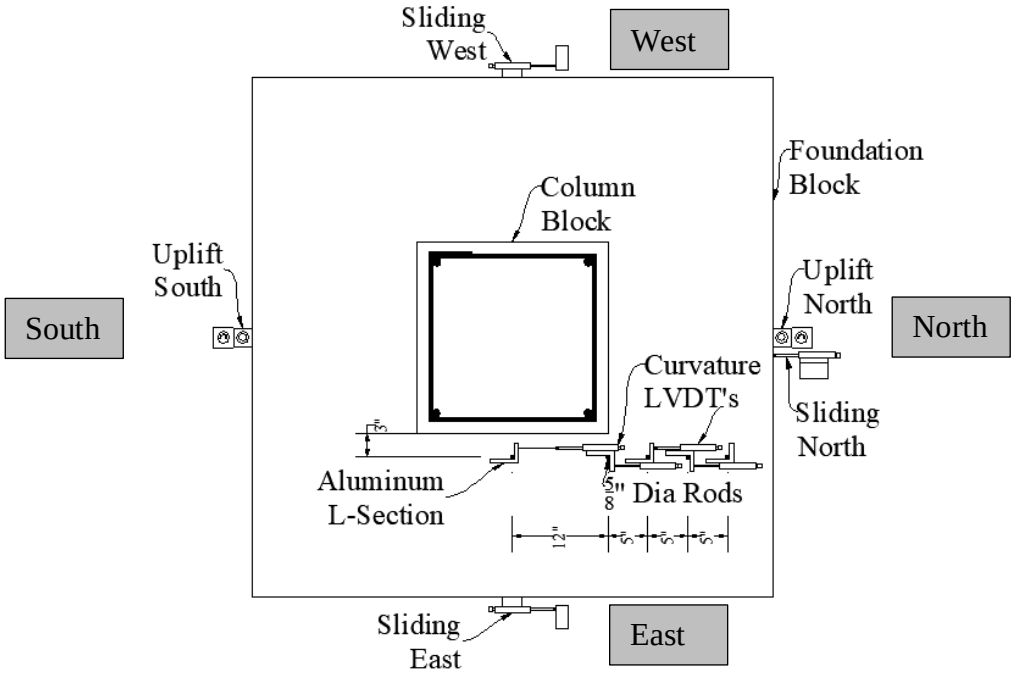

Figure 4.7: Typical external instrumentation for the foundation.

4.7.1.2 *Strain Gauges*

In order to measure the foundation rebar strain in the longitudinal and transverse direction of loading, several strain gauges were placed on select foundation rebar. The locations are presented in Figure 4.8. Four strain gauges were placed along the direction of lateral loading in the rebar running through the center of the foundation. The lateral load was applied in the N-S direction for all test specimens.

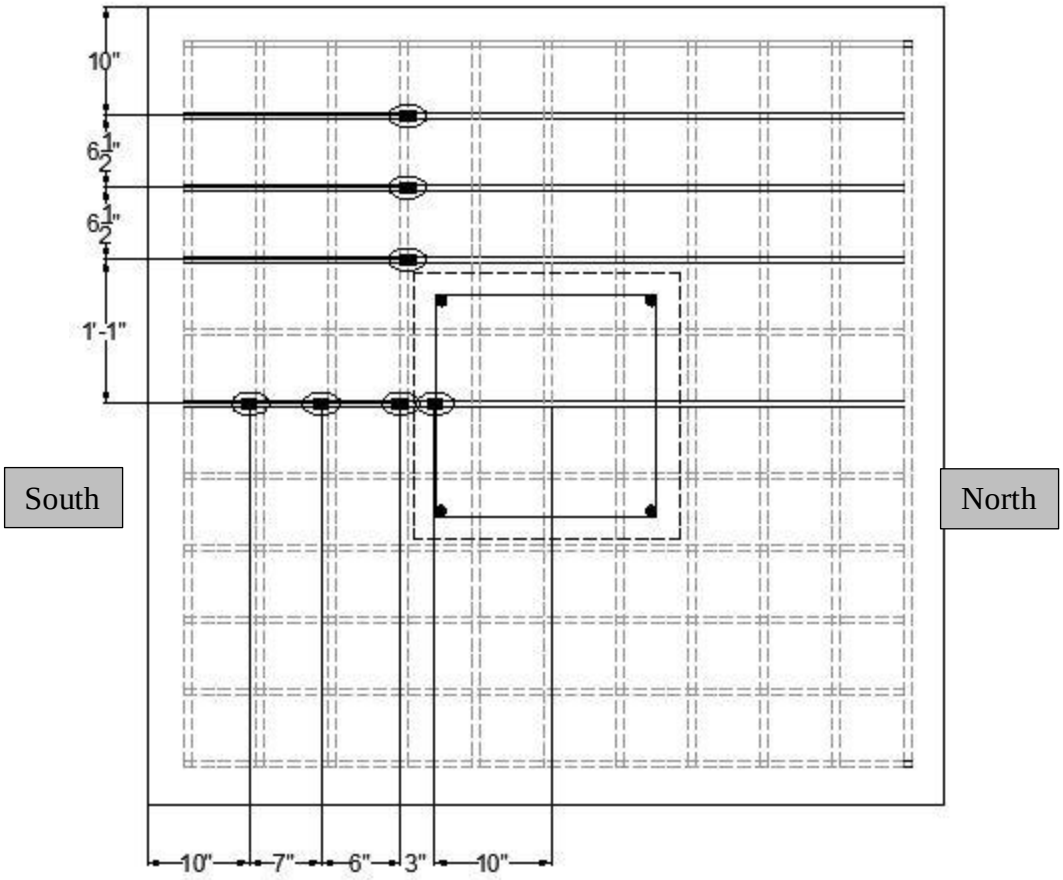

Figure 4.8: Internal instrumentation for the foundation. (Only the foundation reinforcement is shown for simplicity; rebar with no strain gauges are shown using dashed lines)

4.7.2 Column Instrumentation

The column was instrumented with several displacement transducers and strain gauges to monitor the global and local response of the column specimen. Following subsections summarize the details of column instrumentation.

4.7.2.1 *Global Behavior*

The global response was monitored using displacement sensors connected to the column. Lateral load and displacement imposed by the lateral actuator was recorded using the load cell and LVDT attached to the actuator. Column top displacements were measured with a string potentiometer (string pot) attached to a fixed reference frame. Since the string pot was recording absolute column top displacements, this measurement was not influenced by any relative movement of the test setup. However, because the foundation was not anchored to the floor and was allowed to rotate, slide, and uplift, measurements recorded by the string pot required post-processing in order to obtain column top displacements that correspond to applied lateral loads.

The lateral displacement recorded by the actuator LVDT was initially used to set the magnitude of the loading protocol displacement history. Again, column top displacements did not necessarily match the magnitude targeted in the loading protocol. Thus, to maintain an intended lateral loading protocol, the displacement history was updated based on the displacement recorded by the string pot attached to the column top. Figure 4.9 shows the instrumentation details employed for column global response measurements.

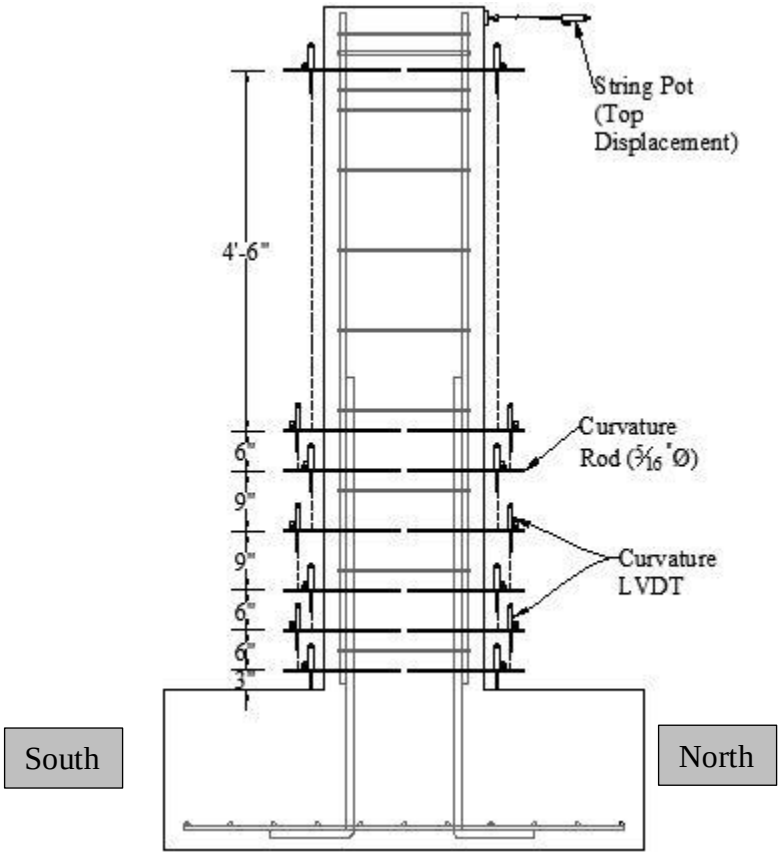

Figure 4.9: Typical column external instrumentation.

4.7.2.2 *Column Curvature*

Seven curvature LVDTs were mounted on each side of the column as illustrated in Figure 4.9. A smaller spacing was chosen for the plastic hinge region (bottom section) where the most significant damage was anticipated. The last LVDT was placed on top of the column section to capture average curvature for the top two thirds of the column, which was expected not to undergo any significant damage. Threaded steel rods of 5/16 inch diameter were embedded into the concrete core to facilitate the mounting of the LVDT's. Curvature rods of 36-inch length were cut in half and were inserted in two opposite sides along the centerline of the column as shown in Figure 4.9. Two thirds of each 18 inch long curvature rod was embedded and bonded into the concrete while the rest was sticking out from the face to facilitate mounting of LVDTs. L-shaped aluminum brackets were used to attach LVDTs with curvature rods. These LVDTs measure the relative

vertical displacement between two curvature rods from which the rotation angle between each curvature rod could be computed. Finally, average curvature between two rods was calculated based on the gauge length, i.e. the vertical distance between rods.

4.7.2.3 *Strain Gauges*

Strain gauges were used to measure strain in both longitudinal and dowel bars at critical locations. In addition, three strain gauges were placed at the transverse reinforcement to measure the strain of the tie bars resulting from cyclic displacement demand. Out of the four longitudinal and dowel bars, only two on each side were instrumented with strain gauges at select locations. A total of 10 strain gauges were mounted on the dowel bars, hence each bar having five gauges. A total of 12 gauges were placed on the longitudinal reinforcement, hence each bar having 6 gauges. Locations are shown in Figure 4.10. Strain gauges along the base of the column were closely spaced to have accurate resolution in the plastic hinge zone. Two of the dowel strain gauges in each bar were placed in the column footing to capture the strain profile within the foundation. The first three transverse tie bars starting from the base were instrumented with similar strain gauges at the center.

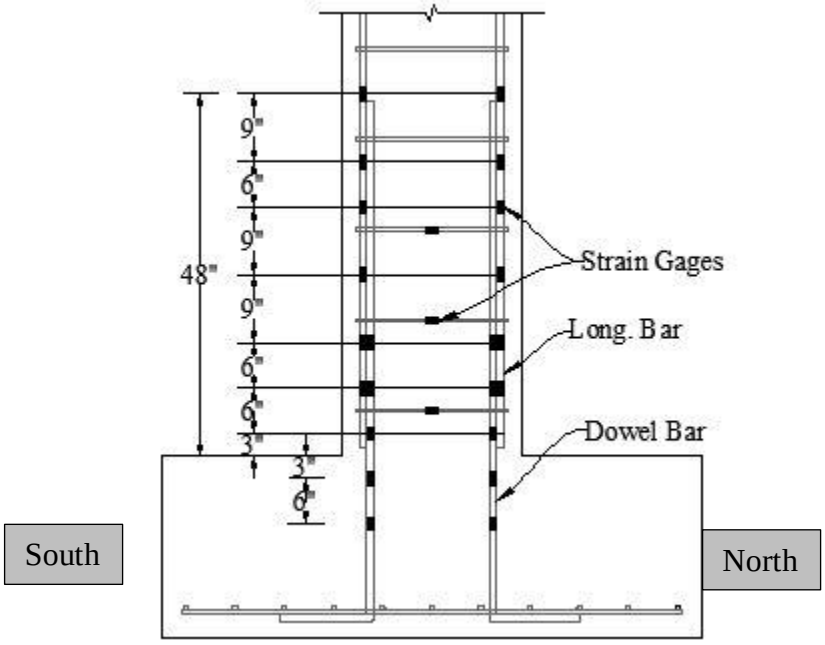

Figure 4.10: Typical column internal instrumentation.

4.8 LOADING PROTOCOL

Following sub-section describes the loading protocol used for the current experimental program.

4.8.1 Axial Loading Protocol

The reasoning behind varying axial loading due to lateral load reversal is illustrated in Figure 4.11: The self-weight of the bridge's sub and superstructure are considered as axial column

loads, which were found to vary between 50 kips to 275 kip for a typical bridge in Oregon. The average axial load was found to be 130 kip with a standard deviation of 48.5 kip. Because previous research has found that a higher level of damage is associated with higher axial loading, a maximum axial load of 240 kip was considered in the constant axial loading protocol for this research. The variation in axial load resulting from the lateral resistance of a two-column bridge bent was found to be 40 kip. Hence, a base axial load if 200 kip was selected for the variable axial loading protocol with a ±40 kip variation from the base value based on lateral strength at each ductility level. The variable axial loading protocol is illustrated in Figure 4.12.

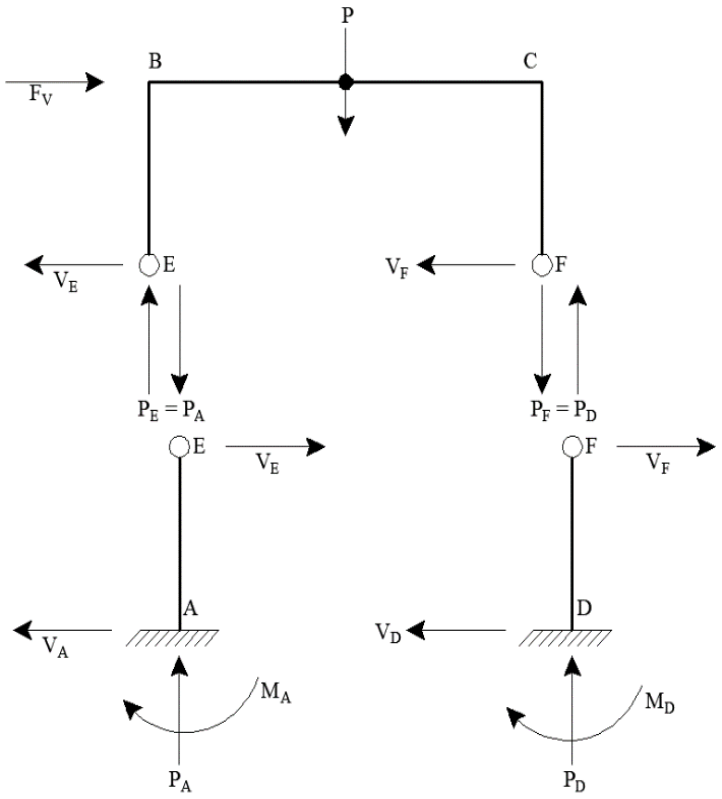

Figure 4.11: Free body diagram for variation of axial load in a two-column bridge bent.

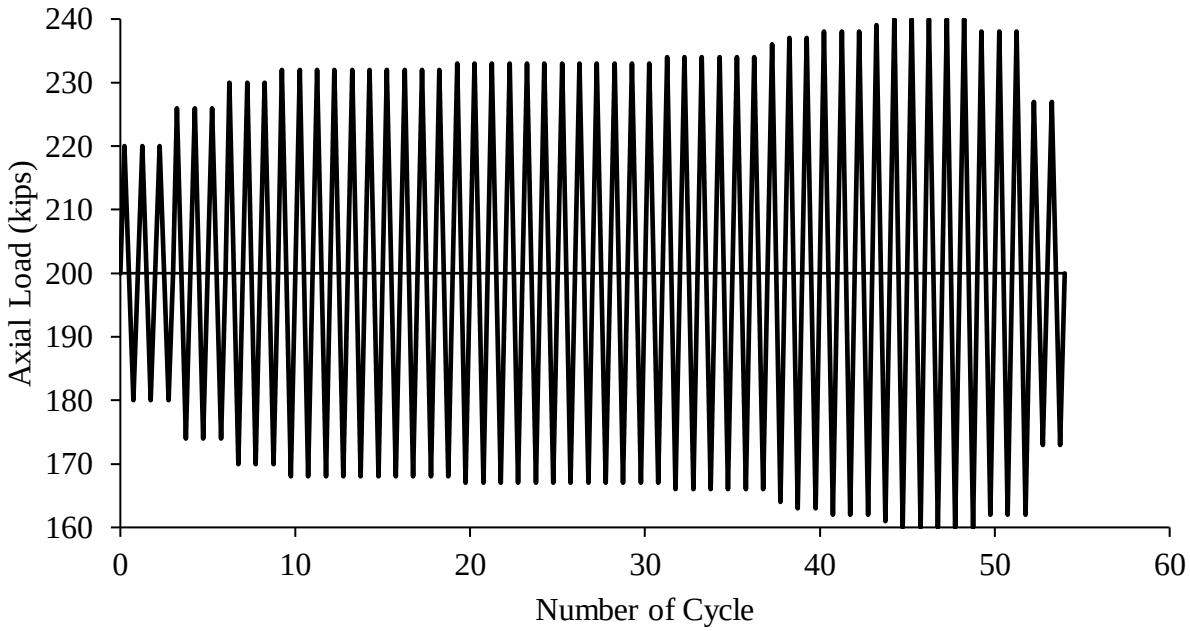

Figure 4.12: Variable axial loading protocol

4.8.2 Lateral Displacement History

Two different sets of lateral loading protocols were used in this research. For "Test series I", the parameter varied was axial loading and hence the specimens were tested using the same lateral loading protocol. However, for "Test Series II", the parameter studied was the lateral displacement history and hence two different loading protocols were used, namely the subduction zone loading protocol and the conventional laboratory loading protocol (Figure 4.13).

A symmetric three-cycle set loading history commonly known as standard (conventional) laboratory loading protocol was employed for specimen LVF#8. The loading protocol is divided into stages, starting with elastic cycles at 0.25, 0.50 and 0.75 multiples of the analytically predicted yield displacement and concluded with one cycle of the predicted yield displacement.

Contrary to the standard laboratory loading protocol developed for crustal earthquakes, the subduction zone earthquake would impose a significantly higher number of inelastic cycles. The subduction zone loading protocol that was used was developed by (Bazaez and Dusicka 2014) to reflect the increased inelastic demand in bridge columns subjected to a long-duration subduction zone earthquake. A higher number of cycles at the low ductility level and lower cycles at the higher ductility level characterizes this subduction zone loading protocol. The loading protocol consists of two stages where the first stage consists of three cycles, each having the following pre-yield displacement levels $0.25\delta_i$ (V_i), $0.5\delta_i$ (V_i), $0.75\delta_i$ (V_i), followed by one cycle at $1.0\delta_i$ (V_i), in order to capture the low damages states (i.e. first cracking, progression of crack, crack width etc.). Here, δ_i is the theoretical yield displacement as obtained from a moment curvature analysis of the column section. V_i is the theoretical strength at a concrete compressive strain of 0.004. The second stage of the subduction zone loading protocol consists of inelastic displacement cycles representing the high demands imposed by a subduction zone earthquake.

Figure 4.13 illustrates the subduction zone loading protocol where dotted and solid lines represent pre-yield displacement cycles and post-yield inelastic cycles, respectively.

For this research, the subduction zone loading protocol with a target displacement ductility, $\mu = 8$ and a fundamental period of 0.5 sec was used. This period was found to be representative of multi-column reinforced concrete bridge columns (Bazaez and Dusicka 2014).

The forces at the specified yield displacement were recorded (both directions) and the stiffness of the column was calculated based on the first yield displacement from moment curvature and these forces. The updated yield displacement was then calculated as the ratio between the theoretical strength at $\varepsilon_c = 0.004$ and the calculated stiffness.

Finally, the effective yield displacement was determined following equation (4.1) and used as the base ductility level ($\mu_\Delta = 1.0$) for the subsequent displacement cycles.

$$\Delta_y = \Delta'_y * (M_n/M'_y) \quad \textbf{(4-1)}$$

Where:

Δ_y is the effective yield displacement, M_n is the nominal moment capacity defined by compression strain of $\varepsilon_c = 0.004$ and M'_y is the moment capacity corresponding to ε_c.

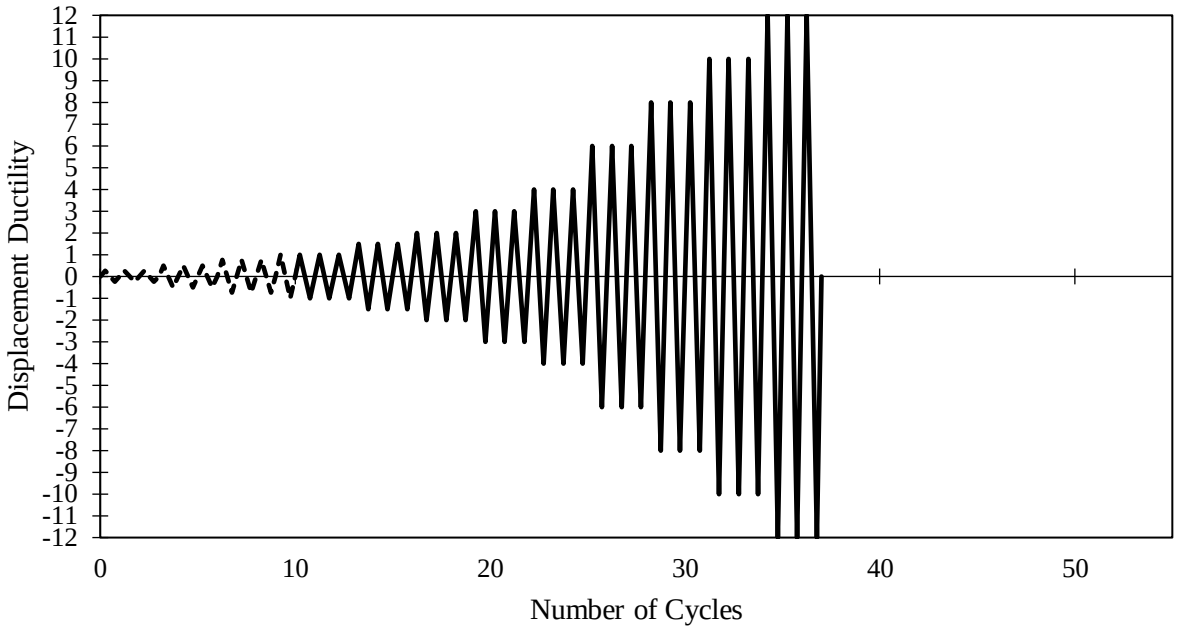

(a)

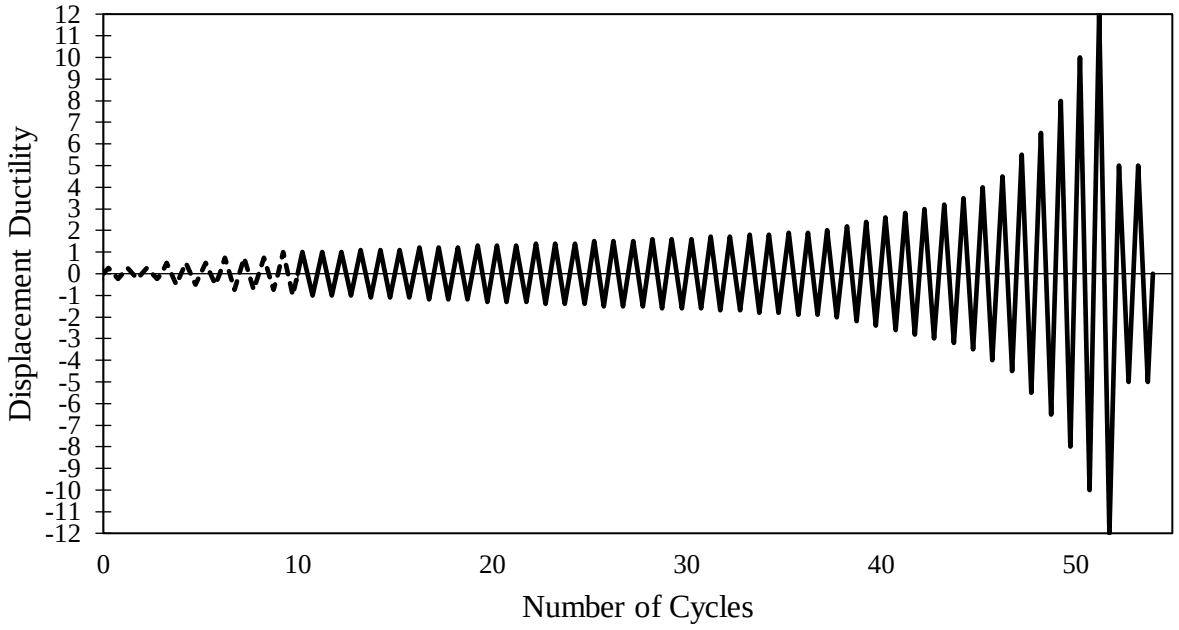

(b)

Figure 4.13: Lateral loading protocols: (a) Conventional laboratory and (b) Subduction zone loading protocol

4.9 SUMMARY

Chapter 4 presented details of the experimental program including test matrix, specimen construction, test setup, test variables studied, and instrumentation and loading protocols. The

specimen details including geometry, reinforcing details and loading conditions were established for the experimental program. Typical bridge bent details were first developed (Chapter 3) through statistical analysis of available bridge drawings and later used to define the test specimen.

Three full-scale representative bridge substructure subassembly specimens were constructed at Portland State University. A cantilever square reinforced concrete column with 4 #8 longitudinal rebar having a lap splice in the plastic hinge zone was selected for the test specimen. A square spread footer with single layer of #5 rebar spaced at 6½ inch was selected as the foundation supporting the square column. These test specimens were incorporated into a two-series test matrix designed to investigate the effect of axial and lateral load variation. A unique experimental setup was developed to facilitate the investigation of the variables considered. Local and global instrumentation including external LVDTs and strain gauges were placed to capture different force and deformation quantities.

Two sets of lateral loading protocols were considered for the test program, namely a subduction zone lateral loading protocol and a conventional three-cycle symmetric laboratory loading protocol. The standard laboratory loading protocol consists of three cycles at each displacement ductility whereas the long duration subduction zone loading protocol mimics the higher displacement demands imposed by a full-rupture subduction-zone earthquake. Two different axial loading protocols were used, the first having a constant axial load and the second variable axial loading resulting from lateral load reversal during an earthquake event.

5.0 EXPERIMENTAL RESULTS AND ANALYSIS

5.1 INTRODUCTION

The current chapter describes the results obtained from the experimental program of three reinforced concrete column-spread footing sub-assemblies. Test data was generated using external and internal instrumentation as described in Chapter 4.0. Visual observations of the damage for individual specimens are described in Sections 5.2.1 through 5.2.3. Measured data of global and local response quantities are described in Section 5.3.

5.2 VISUAL OBSERVATIONS

Each specimen was visually inspected for damage throughout the test. In order to monitor the formation and progression of concrete cracking, crack maps were generated after each cycle during the pre-yield cycles. During the post-yield cycles, only the end cycles for each ductility level were inspected unless any major damage occurred.

The lateral loading was applied along the north-south direction. The north face of the column was under tension during the pull cycle and under compression during the push cycle of lateral loading. Loading cycles mentioned here are half cycles. A half cycle of loading is considered as the load reversal from a push cycle to a pull cycle or vice versa. Whereas a complete full cycle represents load reversal from a pull cycle to another pull cycle of loading.

5.2.1 Specimen SCF#8

This specimen was tested under subduction zone lateral loading protocol with a constant axial load of 240 kip (see Section 4.2 for details). The sequence of damage for specimen SCF#8 was found to be concrete cracking, flexural yielding of longitudinal rebar, spalling/flaking of cover concrete, and rebar buckling. The following sub sections discuss the physical damage observed during the test.

5.2.1.1 *Concrete Cracking*

Hairline flexural cracks were first observed at the end of the 10^{th} loading cycle (2^{nd} pull cycle at target displacement ductility, $\mu = 0.5$) on the north face of the column. The maximum lateral displacement and force associated with this cycle was -0.24 inch and -28.7 kip (pull cycle), respectively. The first crack appeared at a height of 18 inch measured from the foundation face and extended across the entire north face of the column with an approximate length of 24.5 inch. Cracking at the column-footing joint interface was also observed at this cycle on the north face of the column.

5.2.1.2 *Rebar Yielding*

First yield of the north dowel bar was recorded at the end of 20th loading cycle (2nd pull cycle at target displacement ductility, μ = 1.0). The corresponding lateral displacement and load was -0.404 inch and -35.1 kip (pull cycle), respectively. Multiple cracks were observed on both the north and south faces along the height of the column prior to yielding of the dowel bar. The maximum height of crack formation observed at the end of this cycle was approximately 41 inch from the column-footing interface. In addition, a vertical crack with a height of 5.5 inch was observed on the east face of the column.

5.2.1.3 *Concrete Spalling*

Spalling of cover concrete was observed at the end of 94th loading cycle (1st pull cycle at target displacement ductility, μ = 3.5) on the southeast corner of the column. The maximum lateral force during this loading cycle was -41.04 kip and the column top displacement was -1.87 inch (pull cycle). The subsequent cycles at higher displacement ductility levels were associated with extensive spalling of cover concrete at the base of the column on the north and south faces. At the end of the displacement ductility, μ = 12.0 (push cycle), extensive cover spalling on the north face of the column was observed with a spalling height of 9 inch. In the following loading cycle, the concrete cover on the south face of the column was also completely lost.

5.2.1.4 *Rebar Buckling*

Visual observation of rebar buckling was observed in the southeast corner dowel bar of the column by the end of 104th loading cycle (1st pull cycle at target displacement ductility, μ = 12.0). The maximum-recorded lateral force at rebar buckling was -26.45 kip. The column top displacement corresponding to the bar buckling in the south side was recorded as -5.91 inch (pull cycle). It is noteworthy to mention that, the buckled bar was visually observed once the spalled cover concrete in the south face was removed at the end of 104th cycle. Therefore, it was not evident if the bar buckled during this loading cycle or it was already buckled from the previous pull cycle. However, since the concrete cover was not completely lost in the previous cycle (102nd cycle) so, the later cycle (104th cycle) was considered as the loading cycle associated with bar buckling damage state.

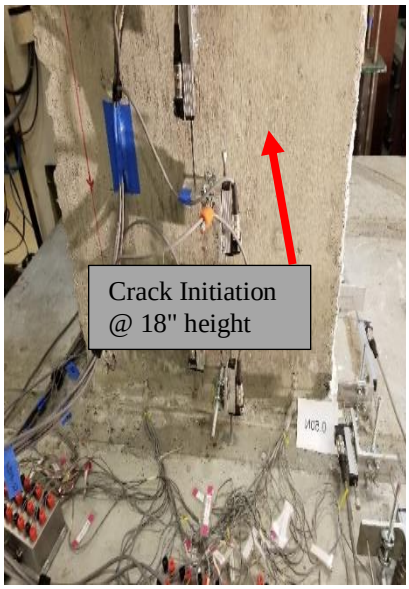

First Crack Appearance
μ_Δ = 0.46 (experimental)
ε_c = 0.0014
ε_s = 0.0013

First Bar Yield
μ_Δ = 0.81 (experimental)
ε_c = 0.0022
ε_s = 0.0023

Effective Yield
μ_Δ = 1.0 (experimental)
ε_c = 0.0029
ε_s = 0.0031

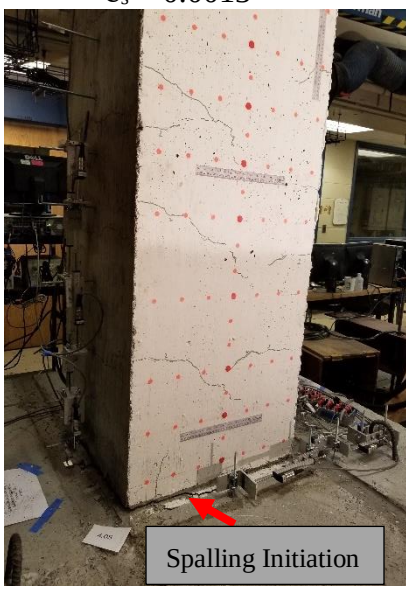

Spalling Initiation
μ_Δ = 3.59 (experimental)
ε_c = 0.0086
ε_s = 0.0347

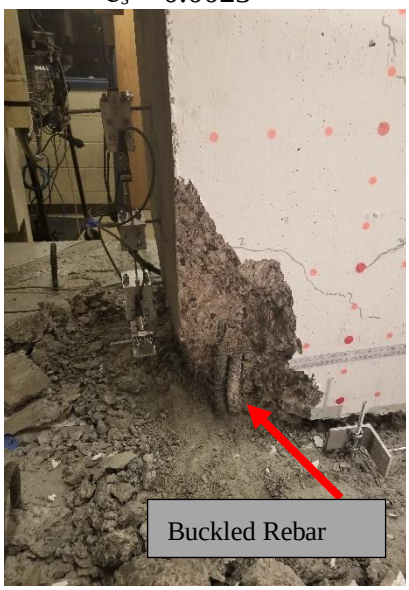

Rebar Buckling
μ_Δ = 11.37 (experimental)
ε_c = 0.074
ε_s = N/M

Ultimate Damage State
μ_Δ = 11.37 (experimental)
ε_c = 0.074
ε_s = N/M

Figure 5.1: Different damage states for specimen SCF#8.

5.2.2 Specimen SVF#8

Specimen SVF#8 was the second specimen in the test matrix. The column-footing specimen was tested under subduction zone lateral loading protocol, which was same as specimen SCF#8.

However, variable axial loading protocol was used for this specimen as described in Figure 5.2. Details of the physical damage observations are discussed in the following sub sections.

5.2.2.1 *Concrete Cracking*

Flexural crack appeared at the end of 6th loading cycle (3rd pull cycle at target displacement ductility, $\mu = 0.25$) in the north face of the column. The lateral load and top displacement measured at the end of this loading cycle was -21.55 kip and -0.12 inch respectively. The horizontal crack formed at 22 inch from the column-footing interface and extended 20.5 inch in the north face of column. Residual crack width measured at the end of this cycle was 0.002" (0.05mm). First diagonal crack started at the column-footing interface and extended 5.5 inch with a 45-degree angle along the length of the column. The appearance of the diagonal crack was observed at the end of 31st loading cycle at a target displacement ductility, $\mu = 1.1$.

5.2.2.2 *Rebar Yielding*

Yielding of longitudinal dowel bar was observed by the end of 19th loading cycle (1st push cycle at target displacement ductility, $\mu = 1.0$). Several cracks formed at different height along the column length prior to yielding of the dowel bar. Lateral load and displacement associated with the first rebar yielding was recorded as 38.54 kip and 0.46 inch respectively. The maximum residual crack width measured at the end of this cycle was 0.008" (0.20mm). It was also observed that, most of the cracks formed were concentrated at the location of transverse reinforcement.

5.2.2.3 *Concrete Spalling*

Spalling of cover concrete was observed at the end of 85th cycle (1st push cycle at target displacement ductility, $\mu = 3.0$). Spalling of cover concrete was observed on the east face of the column, which was oriented at right angle to the lateral loading direction. This evident that the spalling of cover concrete resulted from lap-splice failure in the northeast dowel bars rather than crushing of concrete. Lateral load and column top displacement recorded at the end of this loading cycle was 44.07 kip and 1.34 inch respectively. It was also observed that, the previously formed vertical crack in the east face was extended 10 inch along the height of the column in the prior loading cycle.

5.2.2.4 *Residual Crack Width*

The residual crack width greater than 0.04" (1.0 mm) was considered as the damage state when intervention is required for long-term serviceability of the bridges. Following an earthquake event, any bridge column having residual crack width greater than 0.04" (1.0mm) need to be repaired with epoxy injection to prevent long-term corrosion of reinforcing bars. The residual crack width exceeding 0.04" (1.0mm) was measured for this specimen at the end of 86th loading cycle (1st pull cycle at target displacement ductility, $\mu = 3.0$). Measured lateral load and displacement corresponding to the residual crack width exceeding 0.04" (1.0mm) was -36.43 kip and -1.18 inch respectively.

5.2.2.5 *Rebar Buckling*

The ultimate damage state was defined as 20% drop from the peak lateral load capacity and was recorded at the end of 104th loading cycle (pull cycle at target displacement ductility, μ = 12.0). The peak lateral load was measured to be 46.2 kips and the lateral load measured at the end of this loading cycle was -33.31 kip. Visible buckling of north dowel bar was observed at the end of this cycle. The lateral displacement associated with bar buckling loading cycle was -5.30 inch. However, considerable crushing of cover concrete was observed prior to this cycle with a spalling height of 12 inch from the column–footing interface. Different damage states for the test specimen SVF#8 is presented in Figure 5.2.

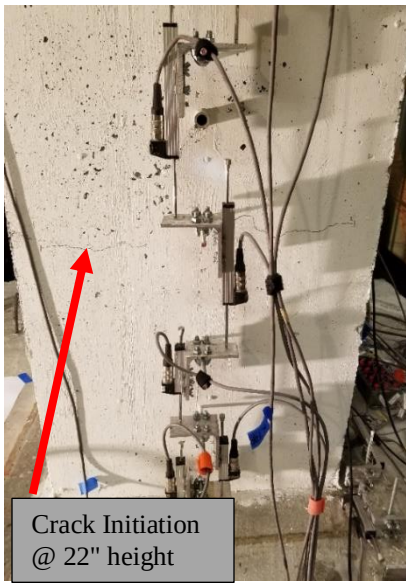

First Crack Appearance
μ_Δ = 0.21 (experimental)
ε_c = 0.0012
ε_s = 0.0017

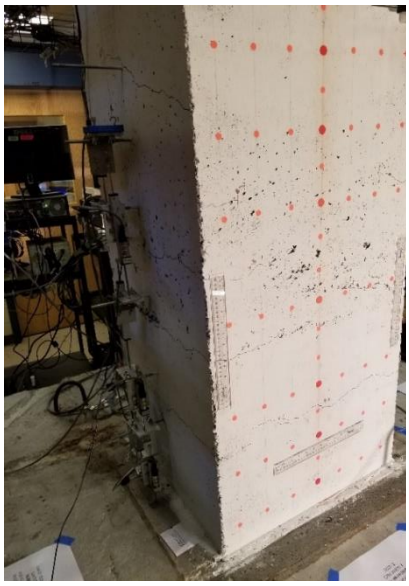

First Bar Yield
μ_Δ = 0.79 (experimental)
ε_c = 0.0029
ε_s = 0.0024

Effective Yield
μ_Δ = 1.0 (experimental)
ε_c = 0.0033
ε_s = 0.0027

Residual Crack Width>1mm
μ_Δ = 2.03 (experimental)
ε_c = 0.0047
ε_s = 0.0172

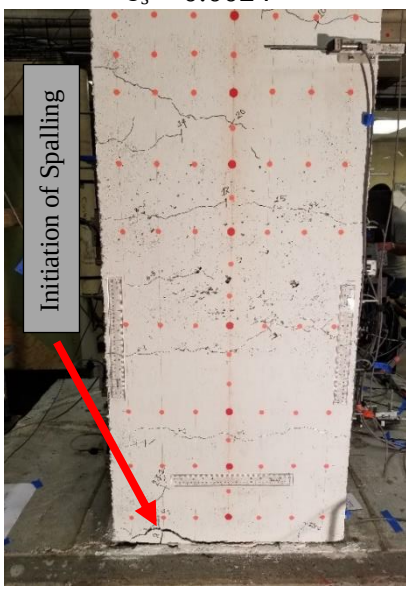

Spalling Initiation
μ_Δ = 4.62 (experimental)
ε_c = 0.0054
ε_s = 0.02

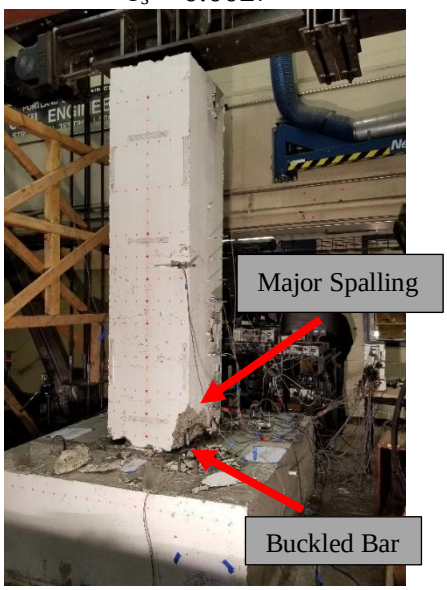

Ultimate Damage State
μ_Δ = 9.13 (experimental)
ε_c = 0.048
ε_s = N/M

Figure 5.2: Different damage states for specimen SVF#8.

5.2.3 Specimen LVF#8

LVF#8 was the last specimen tested under the current experimental program. In order to investigate the effect of lateral loading, the specimen was tested under symmetric three-cycle

laboratory loading protocol. The axial loading protocol was similar to the specimen SVF#8 and was variable in proportion with the amplitude of the lateral load. Details of the damage observed is presented in Figure 5.3 and are discussed in the following sub sections.

5.2.3.1 *Concrete Cracking*

A hairline flexural crack was observed in the north face of the column-footing interface during the 2nd cycle of loading (1st pull cycle at target displacement ductility, $\mu = 0.50$) at a height of 17 inch measured from the column-footing interface. Lateral load and column top displacement measured at the end of this loading cycle was -22.21 kip and -0.15 inch, respectively. In addition, a vertical crack was observed in the north face along the northeast corner. In the later stages of loading, spalling of cover concrete was observed along the line of this vertical crack.

At the end of the 9th cycle, the crack formation stabilized and no new cracking was found in the next three loading cycles. Three additional cracks were found at the 12th, 16th and 18th cycles of loading corresponding to a displacement ductility of 1.0, 1.5^{+1} and 1.5^{+2}, respectively. No new crack was found to form during the later stages of loading. However, the existing cracks were found to increase in width with almost each increasing loading cycle.

5.2.3.2 *Rebar Yielding*

The first rebar yielding was recorded based on the strain data obtained from the strain gauges at different locations in the column longitudinal and dowel bars. The dowel bar in the south-west corner of the column was first observed to yield at the end of the 5th loading cycle (1st push at target displacement ductility, $\mu = 0.75$). Considerable crack of the column in the south face was observed prior to yielding the south dowel bar. The maximum crack width during this cycle was found to be 0.008" (0.20 mm), and the residual crack width measured was 0.002" (0.05 mm).

Dowel bar at the north-west corner was found to exceed the theoretical yield strain in the following pull cycle (6th loading cycle at target displacement ductility, $\mu = 0.75$). Similar to the south face, considerable cracking of the north face was also observed before yielding the dowel bars. The maximum crack width recorded at this cycle was found to be 0.008" (0.20 mm). However, the crack at the column-footing interface opened up by 0.03" (0.76 mm). The residual crack width following the north dowel yielding was recorded to be less than 0.002" (0.05 mm).

5.2.3.3 *Residual Crack Width*

The residual crack width was measured at zero force while returning from a peak push or pull displacement cycle. Residual crack width measured at the first 6 cycles of loading was insignificant and were less than 0.002" (0.05 mm). At the end of the 7th cycle (1st push cycle at target theoretical displacement ductility, $\mu = 1.0$), the residual crack width was measured to be 0.004" (0.1 mm) whereas the maximum crack opening recorded at the peak displacement was 0.028" (0.70 mm).

At the end of target displacement ductility $\mu = 1.0$, the maximum recorded residual crack width during the push and pull cycle were 0.007" (0.18 mm) and 0.008" (0.20 mm) respectively whereas the maximum crack opening measured at the peak displacement level for these two cycles were 0.04" (1.02 mm) and 0.06" (1.52 mm) respectively. The residual crack width increased to 0.01" (0.25 mm) in push cycle and 0.014" (0.35 mm) in pull cycle at the end of displacement ductility $\mu = 1.50$. The maximum-recorded crack opening prior to measuring the residual crack width was found to be 0.1" (2.54 mm) and 0.13" (3.25 mm) in the push and pull cycles respectively. The residual crack width remained stable during the subsequent push and pull cycles at target displacement ductility $\mu = 2.0$. However, a trend in increasing residual crack width was observed starting from the beginning of displacement cycles at target ductility $\mu = 3.0$.

Finally, the serviceability limit state based on the residual crack width of 0.04" (1.0 mm) was found to be exceeding at the end of 32nd cycle (pull cycle at target displacement ductility, $\mu = 3.0$). The maximum-recorded residual crack width was found to be 0.04" (1.02 mm) in both the north and south side of the column. Lateral load and column top displacement associated with this cycle was -38.69 kip and -1.96 inch. Last recorded residual crack width at the end of target displacement ductility $\mu = 6.0$, was found to be 0.25" (6.50 mm) while loss of cover concrete was observed in both the north and south face of the column.

5.2.3.4 *Concrete Spalling*

Vertical crack in the column face was observed as early as 2nd cycle of loading at target displacement ductility, $\mu = 0.25$. The vertical cracks formed in the earlier cycles were found to be extending with subsequent loading cycles and later contributed to the spalling of cover concrete along these cracks. Initiation of cover concrete spalling was noticed at the end of the third push cycle at target displacement ductility, $\mu = 3.0$. The final push cycle at target ductility, $\mu = 6.0$ resulted in major spalling of cover concrete in the north face of the column with a spalled height of 8 inch and base width of 12 inch. The spalling in the north face of the column resulted in exposing the rebar in the northeast corner, which later facilitates buckling of the dowel bar in the subsequent loading cycle. South face of the column also experienced major spalling at the end of the second pull cycle (43rd cycle) while exposing the longitudinal and dowel bar in the south-west corner.

5.2.3.5 *Rebar Buckling*

Buckling of the dowel bars in both the south and north face was observed during the test at higher displacement ductility cycles. Bar buckling was first initiated by the loss of cover concrete in previous loading cycle. At the end of the final push cycle at displacement ductility, $\mu = 6.0$, the northeast corner of the column cover concrete was spalled off entirely and hence exposed the rebar in that corner. Observation showed no sign of bar buckling at the end of this cycle. However, the north corner was in tension while the south face was in compression in the subsequent loading cycle (final pull cycle at target ductility, $\mu = 6.0$). This resulted in cover concrete loss in the south face of the column. While returning from this cycle (also the beginning of push cycle at target

ductility, $\mu = 8.0$), the north face rebar was put in compression and resulted in buckling without the support of cover concrete. Similarly, the previously exposed bar in the south-west corner buckled following the end of first pull cycle at target displacement ductility, $\mu = 8.0$ when the south side bar was in compression. At the end of second pull cycle at target ductility, $\mu = 8.0$ the bar in the southeast corner was also found to be buckled and it is noteworthy to mention that the cover concrete in this corner was exposed in the previous pull cycle.

5.2.3.6 *Bar Fracture*

The final damage recorded for the column was bar fracture in both the north and south side. Significant drop in column lateral load carrying capacity was associated with the fracture of the bar. Previously buckled bar fractured shortly after the reversal of loading cycle. For instance, previously buckled bar in the north face fractured while reversal from push cycle to pull cycle at target displacement ductility, $\mu = 8.0$. Similarly, the buckled bar in the south-west corner fractured in the reversal of loading from pull cycle at displacement ductility, $\mu = 8.0$.

First Crack Appearance
μ_Δ = 0.46 (experimental)
ε_c = 0.002
ε_s = 0.0019

First Bar Yield
μ_Δ = 0.69 (experimental)
ε_c = 0.0027
ε_s = 0.0026

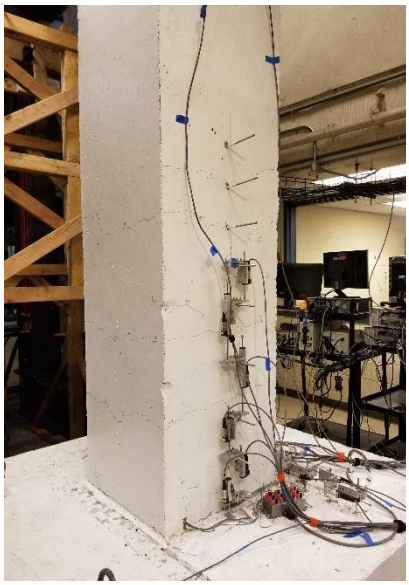

Effective Yield
μ_Δ = 1.0 (experimental)
ε_c = 0.0035
ε_s = 0.01

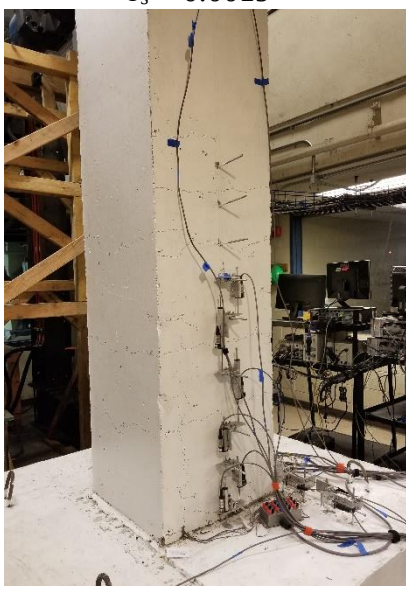

Residual Crack Width>1mm
μ_Δ = 3.0 (experimental)
ε_c = 0.006
ε_s > 0.03

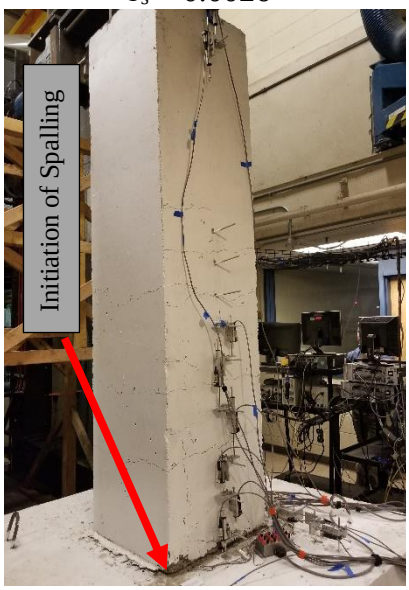

Spalling
μ_Δ = 4.0 (experimental)
ε_c = 0.0078
ε_s = 0.043

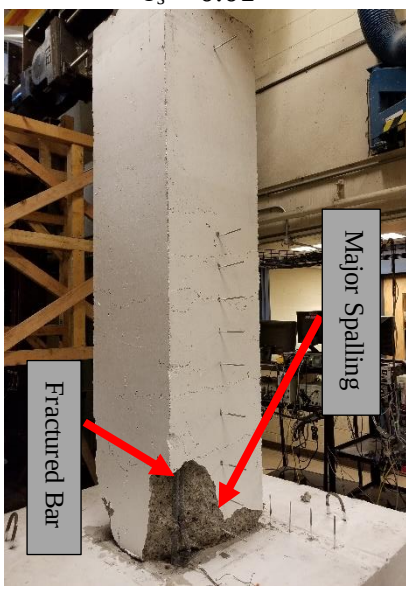

Ultimate Damage State
μ_Δ = 8.0 (experimental)
ε_c = 0.042
ε_s = N/M

Figure 5.3: Different damage states for specimen LVF#8.

5.3 MEASURED DATA

Recorded data from external and internal instrumentation were post processed to evaluate the behavior of the tested specimens under different lateral and axial loading condition. Both global

and local displacement quantities were evaluated to meet the objective of the experimental program. In this section, global behavior of the specimen (i.e. force-displacement relationship, strength and stiffness degradation etc.), effect of lateral and axial loading protocol and local response quantities (i.e. curvature profile, strain profile etc.) of the square column-footing specimens are discussed in detail.

5.3.1 Global Response

The global force-displacement behavior is one of the most important parameters to evaluate the performance of reinforced concrete subassemblies under lateral earthquake loading. Hence, the test specimen was instrumented with external instrumentation to capture the load and deformation quantities. Details of the instrumentation to capture the global load and displacement quantities are described in Section 4.7.2.1. However, the data measured was post-processed to capture the actual load-displacement behavior for the tested specimens and are discussed below.

The column top was free to rotate and translate, which resulted in a horizontal component of the axial load counteracting the applied lateral load. Hence, the actual lateral load that was applied to the column was determined by subtracting the horizontal force component, F_h from the recorded lateral load, $F_{actuator}$, as shown in Figure 5.4.

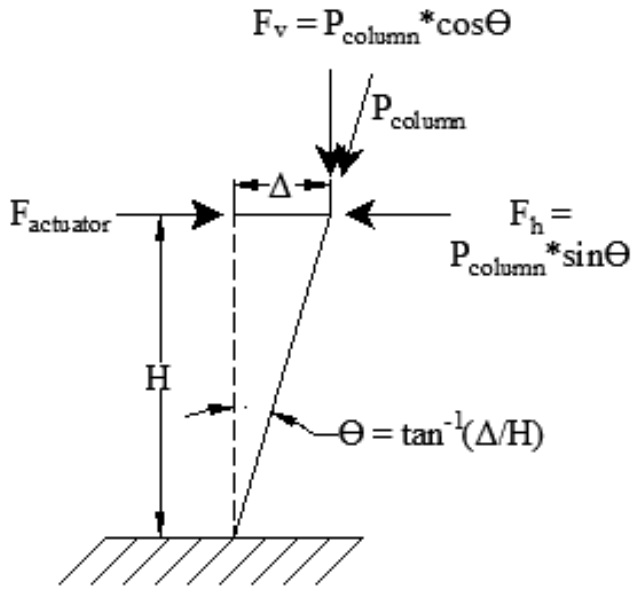

Figure 5.4: Computation of absolute lateral load with axial component correction

Where:

θ = column rotation, Δ = lateral column top displacement, H = height of the column, P_{column} = Applied column axial load, $F_{actuator}$ = Lateral load recorded by the actuator load cell, F_h = Horizontal component of the applied axial load acting in the lateral direction.

Unlike most of the laboratory testing performed by other researchers, the foundation used for these tests was an integral part of the specimen and was placed on the laboratory strong floor without anchoring it to the floor. Hence, the foundation specimen was allowed to rotate, uplift and slide. The data measured from the test showed negligible sliding of the foundation specimen but it experienced significant amount of uplifting. As the top displacement was measured with a string potentiometer attached to the column top, hence it does not exclude any contribution of the uplift in the measured lateral displacement. In order to account for the lateral column top displacement resulting from the foundation uplift, measured data was post processed to exclude the uplift contribution into measured lateral displacement. Figure 5.5 shows the schematic diagram for lateral displacement correction resulting from foundation uplift.

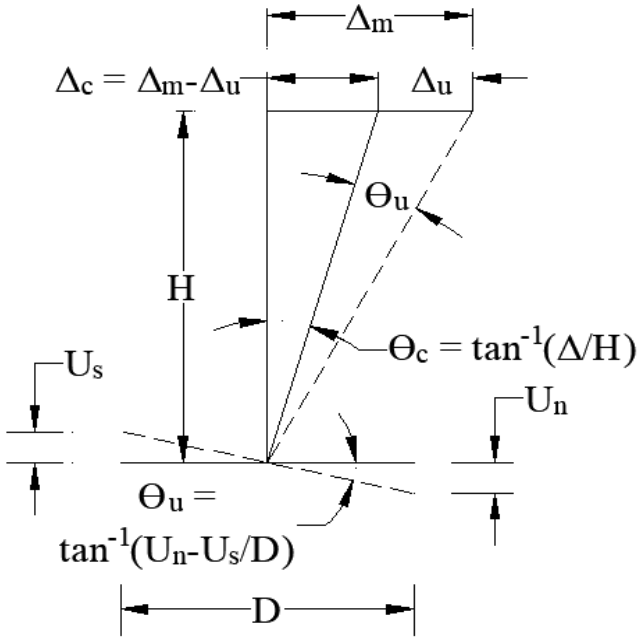

Figure 5.5: Measured lateral displacement correction due to foundation uplift

Where:

U_S = Foundation uplift measured in the south face; U_N = Foundation uplift measured in the north face; D = Horizontal distance between the LVDT mounted on the north and south foundation face; Δ_m = Measured column top displacement; θ_u = Column rotation due to foundation uplift; θ_c = Corrected column rotation without foundation uplift; Δ_u = Column top displacement due to foundation uplift; Δ_c = Corrected column top displacement without foundation uplift.

5.3.1.1 *Force-Displacement Response*

The force-lateral column top displacement response for the three specimens are shown in Figure 5.8. The ultimate capacity for the specimens were determined as 20% drop from the peak lateral capacity. For specimen SCF#8, the test was continued beyond 20% drop in lateral capacity to record bar buckling/fracture damage state. The sequence of failure

modes for the specimens was typically concrete spalling followed by lap splice failure, which at the end resulted in either buckling or bar fracture.

Specimen SCF#8

The lateral force-displacement response for SCF#8 is shown in Figure 5.6. The specimen was tested under a constant axial load of 240 kips ($\approx 0.09A_g f'_c$) and the subduction zone lateral loading protocol. The specimen showed a ductile behavior reaching an ultimate displacement ductility, μ_Δ = 10.1 (5.25 inch) and μ_Δ = -9.23 (-4.79 inch) in the push and pull cycle respectively. The peak lateral strength for specimen SCF#8 was 46.0 kips and -42.4 kips in the push and pull cycles, respectively. The displacement ductility corresponding to the peak strengths was μ_Δ = 2.41 (1.25 in) and μ_Δ = -3.52 (-1.83 inch), respectively.

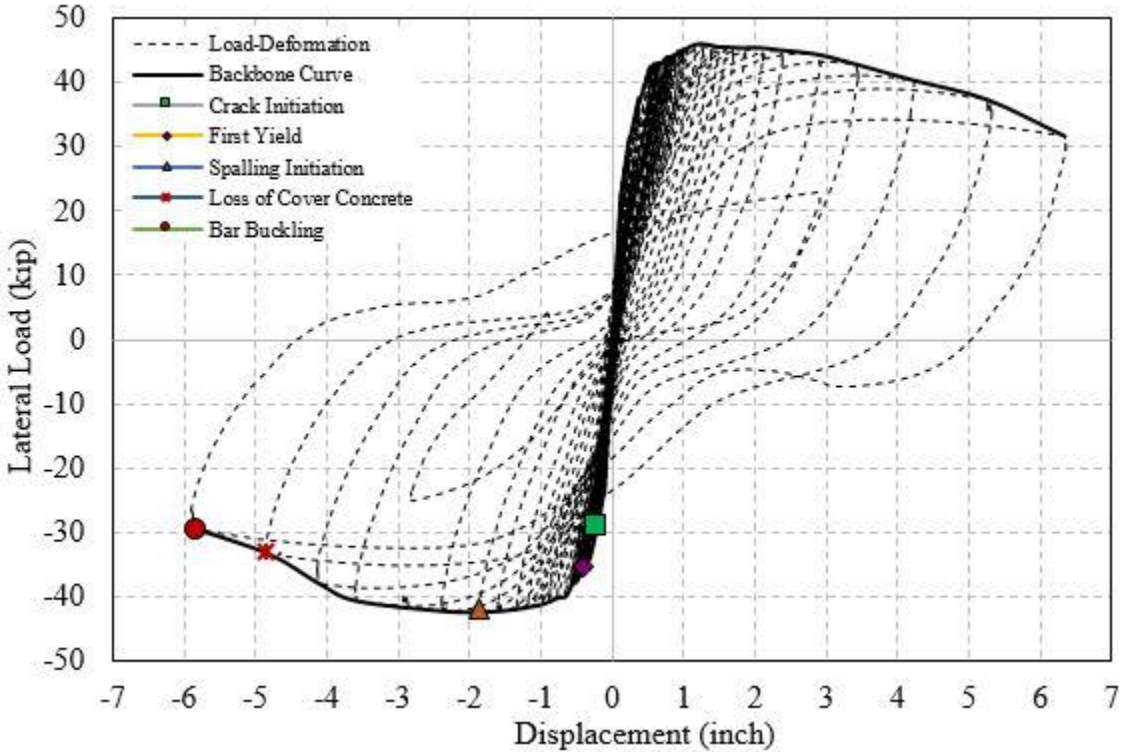

Figure 5.6: Force-Displacement response for specimen SCF#8.

The primary mode of failure for this specimen was concrete crushing at the base of the column with buckling of longitudinal reinforcement. Lap splice failure between the dowel bars and the column longitudinal bar was also evident prior to buckling of the dowel bars. Most of the damage was concentrated at the base of the column where a cold joint formed between footing and column. The formation of the cold joint at the column-footing interface resulted in significant slip between concrete and rebar at this location. The opening and closing of the cold joint along with slip in rebar resulted in a pinched hysteretic behavior for specimen SCF#8. The pinching effect in the hysteretic load-displacement response is pronounced at higher displacement ductility cycles.

Specimen SVF#8

Specimen SVF#8 was tested under variable axial loading and the subduction zone lateral loading protocol. The load-deformation response for the specimen as presented in Figure 5.7 showed that the peak strength achieved in the push and pull cycles was 46.2 kips and -39.6 kips, respectively. The displacement ductility corresponding to the peak strength in the push and pull cycles was μ_Δ = 3.07 (1.78 inch) and μ_Δ = -3.74 (-2.17 inch), respectively. The specimen showed ductile behavior reaching an ultimate displacement ductility of μ_Δ = 9.34 (5.42 inch) in the push cycle and μ_Δ = -9.03 (-5.24 inch) in the pull cycle.

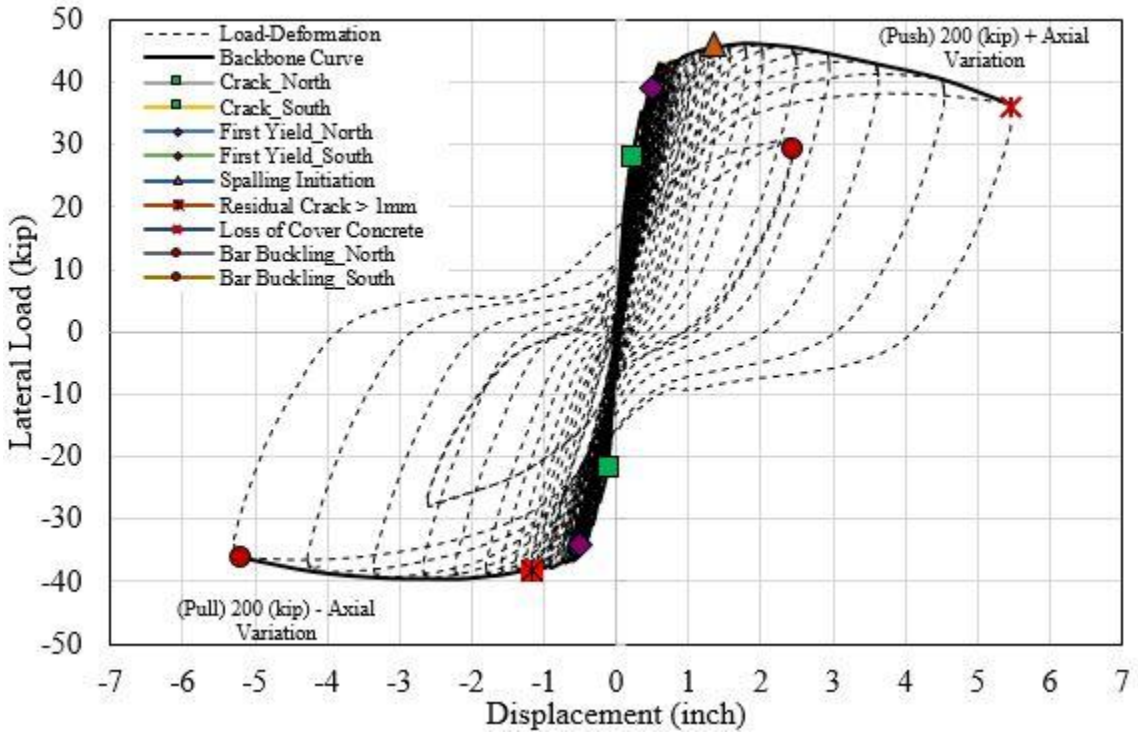

Figure 5.7: Force-Displacement response for specimen SVF#8.

The primary failure mode observed for this specimen was similar to the previous one, where damage was concentrated at the column-footing interface. Extensive concrete crushing at the base with bar buckling and splice failure led to the final damage state. The pinching effect resulting from gap opening and closing at the base along with bar-slip phenomena was also observed for this specimen.

Specimen LVF#8

The lateral force-displacement response for specimen LVF#8 is shown in Figure 5.8 along with different damage states under the reverse cyclic loading protocol. A pinched hysteretic response with a ductile behavior was reported for the column-footing specimen. The peak lateral strength during the push and pull cycles was 41.6 kips and -

40.7 kips, respectively. The displacement ductility corresponding to the peak column strength in the push and pull cycles was μ_Δ = 2.90 (1.88 inch) and μ_Δ = -2.97 (-1.93 inch), respectively. After the peak strength, specimen LVF#8 showed a ductile behavior with almost linear degradation in the subsequent loading cycles.

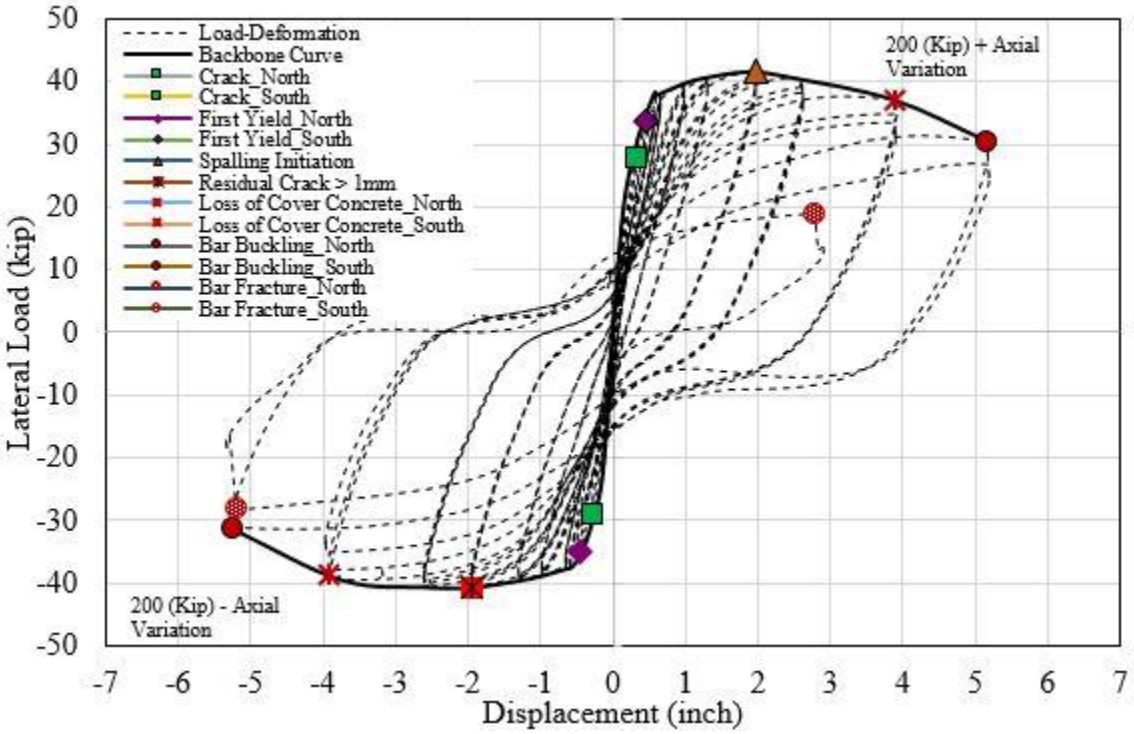

Figure 5.8: Force-Displacement response for specimen LVF#8.

The failure mode for this specimen was mainly crushing of concrete at the base, which resulted in bar buckling and finally fracture of the previously buckled bar. Lap splice failure between the dowel and longitudinal bar was also observed prior to buckling.

5.3.1.2 *Strength Degradation*

Strength degradation is in important parameter to describe the behavior of a system and compare its performance for different variables considered. Here, it was calculated as the percentage change from the peak lateral strength to the last cycle at each displacement ductility level. It is plotted against displacement ductility and shown in Figure 5.9.

Specimen SCF#8

The strength degradation from the peak lateral strength shown in Figure 5.9 reveals almost a linear pattern for the push cycle where maximum degradation was 18.8% at displacement ductility, μ_Δ = 10.1. On the other hand, the maximum degradation of 20.2% was observed in the pull cycle with a non-linear degradation pattern at higher displacement ductility levels. Visual inspection of the test specimen showed higher damage on the south side of the column (pull cycle) including concrete crushing and bar

buckling, which led to a rapid degradation after a displacement ductility, $\mu_\Delta = 8.0$ and is evident from the plot in Figure 5.9.

Specimen SVF#8

The strength degradation for specimen SVF#8 from the peak strength (Figure 5.9) showed a bi-linear behavior until the ultimate damage state was reached. However, the strength degradation in the push cycle was higher than the pull cycle because of higher axial load. The push cycle of loading was associated with higher axial loading where a maximum of 240 kips axial load was applied. On the other hand, the pull cycle was experiencing lower axial loading with a minimum of 160 kips at higher displacement ductility cycles. The strength degradation in the push cycle from the peak strength to the ultimate damage state was 20.7% whereas the degradation in the pull cycle was only 8.92%.

Specimen LVF#8

Strength degradation during the push cycle was higher than the pull cycle for specimen LVF#8. The strength degradation from the peak strength to ductility cycle 4.0, 6.0 and 8.0 in the push direction was 2.24%, 10.7% and 26.5% respectively. Higher degradation at displacement ductility cycle 8.0 can be attributed to the bar buckling in the north side of the column during the first push cycle. On the other hand, strength degradation in the pull cycle from the peak strength to displacement ductility cycle of 4.0, 6.0 and 8.0 was 0.02%, 2.83% and 22.8%. The pull cycle of loading was experiencing lower axial load as compared to the push cycle and hence smaller strength degradation in the pull cycle was expected. However, significant strength degradation from ductility cycle 6.0 to 8.0 can again be attributed to the south bar buckling at the end of first pull cycle at displacement ductility 8.0.

In-cycle strength degradation was also evident from the hysteretic load-displacement behavior of specimen LVF#8 where significant degradation in column strength was found between subsequent loading cycles at same displacement ductility level. It can also be inferred that the column experienced higher in-cycle degradation at higher displacement ductility levels as compared to the lower displacement ductility levels. For instance, the in-cycle strength degradation during the subsequent push cycles at displacement ductility levels 3.0 was 2.34% and 3.59%, whereas the degradation at displacement ductility 6.0 was 6.35% and 9.91%, respectively. It can be attributed to the higher level of damage sustained by the column at every new displacement cycle during the end of the test where higher displacement demand was imposed. The in-cycle strength degradation during the subsequent pull cycle at displacement ductility 3.0 was 1.03% and 1.94% whereas for displacement ductility 6.0 was 3.85% and 11.0%, respectively. Even though the in-cycle strength degradation for pull cycles was less than that experienced during the push cycle, the last pull cycle at displacement ductility 6.0 experienced higher degradation than the last push cycle at ductility 6.0. It was found that the south side of the column experienced major concrete spalling during the second pull cycle at a displacement ductility of 6.0, which resulted in higher degradation in the last pull cycle at ductility 6.0. On the other hand, the north side of the column experienced

major spalling during the final push cycle at a displacement ductility of 6.0 and hence experienced lesser degradation than the last pull cycle. However, the in-cycle strength degradation was not observed in the earlier two specimens as they were subjected to the subduction zone lateral loading protocol, which consists of only one cycle at higher displacement ductility levels.

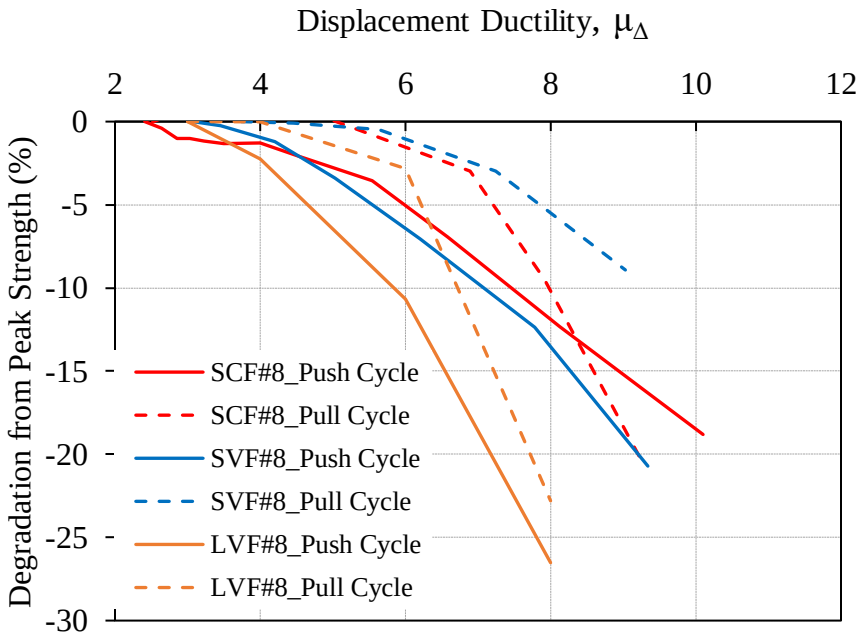

Figure 5.9: Strength degradation for tested specimens.

5.3.1.3 *Stiffness Degradation*

Secant stiffness (K_{sec}) at each displacement ductility cycle normalized against yield stiffness (K_y) is presented herein as the stiffness degradation parameter. The secant stiffness was calculated as the ratio of the force over displacement for the first cycle at each displacement ductility level, whereas the yield stiffness corresponds to the secant stiffness at the effective yield displacement level. Figure 5.10 shows stiffness degradation plotted against displacement ductility for both the pull and push cycle for all the three specimens.

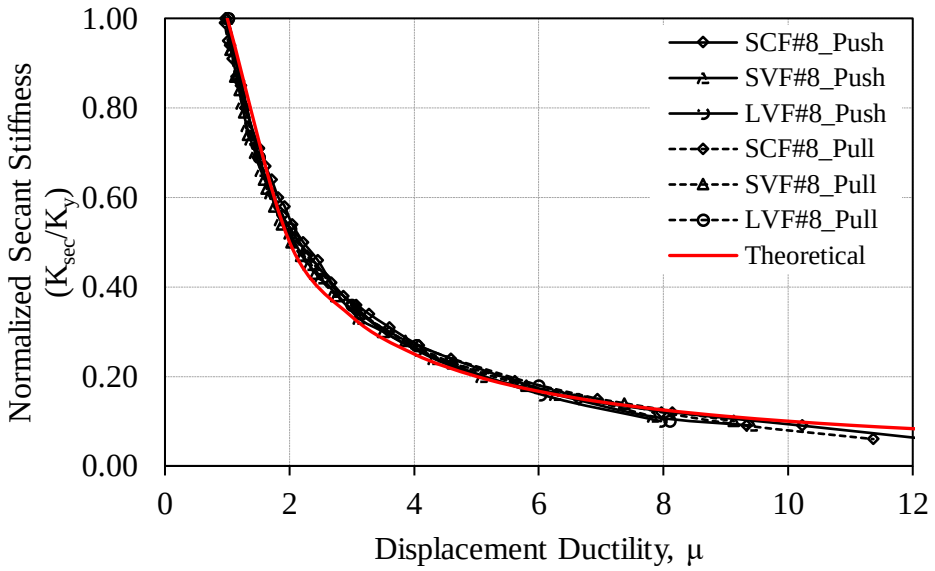

Figure 5.10: Stiffness degradation for tested specimens

All three specimens showed similar stiffness degradations for push as well as pull cycles of loading. Further investigation showed that the pull cycle of loading for specimen SVF#8 and LVF#8 resulted in lower stiffness degradation compared to the push cycle of loading after a displacement ductility of 3.00. This can be attributed to the higher axial load associated with the push cycle of loading for these two specimens. Conversely, push and pull cycles for specimen SCF#8 resulted in a similar stiffness degradation, where the axial load was constant for both cycles. It was also found that the rebar fracture occurring in specimen LVF#8 led to higher stiffness degradation after displacement ductility 7.0 compared to specimen SVF#8. Gulkan and Sozen (1974) proposed a relationship between displacement ductility and secant stiffness, as shown in Equation 5.1. This relationship, which is shown as the theoretical (red) curve in Figure 5.8, was found to agree well with the stiffness degradation for all tested specimens. However, it was also found that the relationship slightly underestimates the stiffness degradation for initial displacement ductility cycles up to 2.0 as well as for higher displacement ductility cycles after 6.0. On the contrary, the relationship slightly overestimates the stiffness degradation for displacement ductilities ranging from 2.0 to 6.0.

$$\left(\frac{K_{sec}}{K_y}\right)_{Theoretical} = \frac{1}{\mu} \leq 1 \qquad \textbf{(5-1)}$$

Finally, it can be concluded that the lateral loading protocol and the variation of axial load minimally influence the stiffness degradation for the specimens tested. The maximum variation in stiffness degradation due to axial load variation was less than 15% whereas maximum variation corresponding to different lateral loading protocol was within 20%.

5.3.1.4 *Effect of Variable Axial Loading*

A series of numerical moment-curvature analyses were conducted for the column section with different axial loads using Response-2000 (Bentz and Collins). This program models load-deformation of cracked reinforced concrete sections using modified compression field theory (MCFT) proposed by (Vecchio and Collins 1986). The yield and ultimate conditions as obtained from these analyses are presented in Figure 5.11(a) through (f). The maximum axial force used in these experiments, i.e. P = -240 kips, is shown for reference, along with the corresponding predicted value of interest. It was found that the higher axial load ratio results in higher peak strength as well as higher strength degradation. Note that Response-2000 is unable to capture stiffness degradation due to repeated loading. On the other hand, lower axial load ratios reduced the peak lateral capacity for the column and resulted in lesser strength degradation following the peak lateral strength.

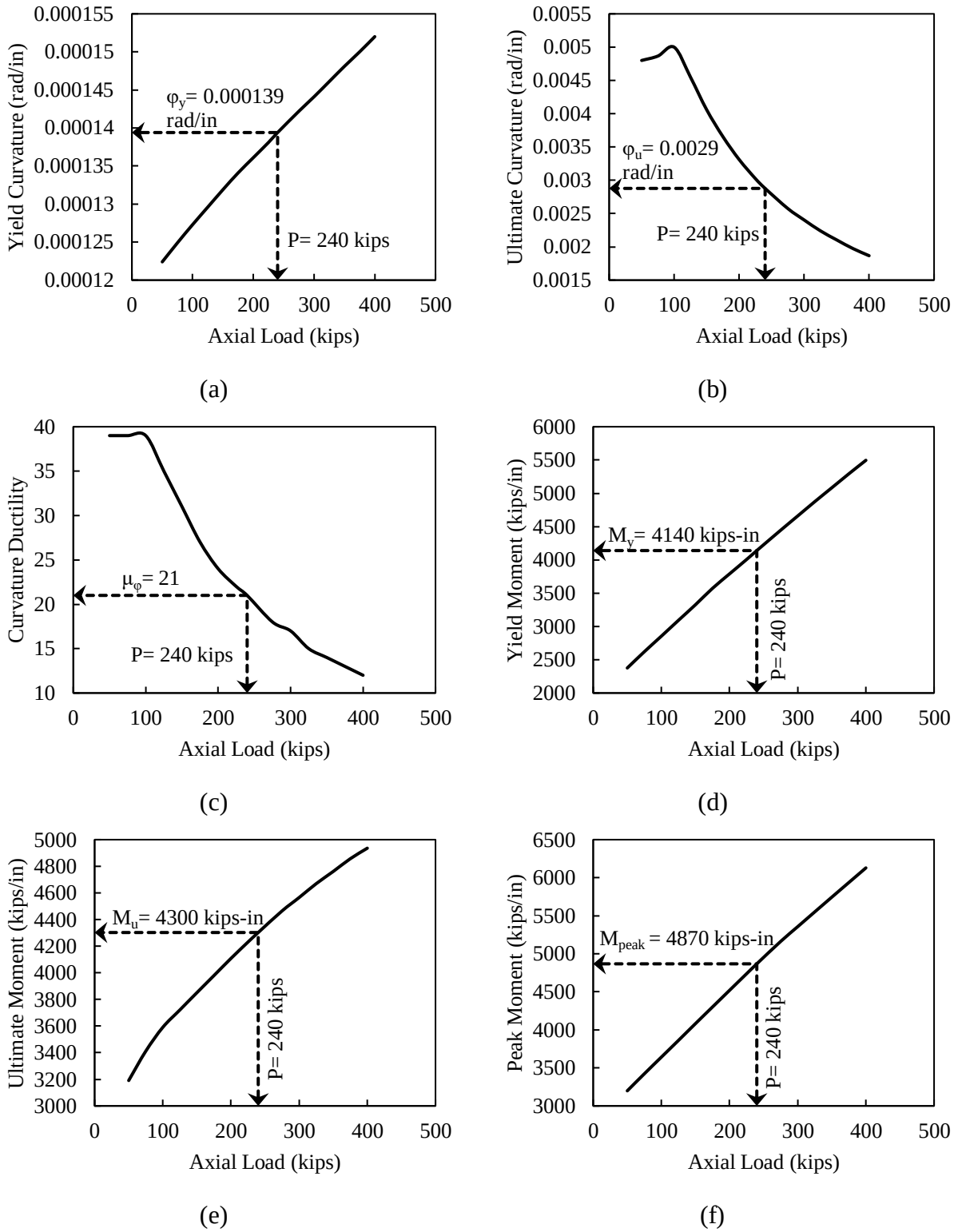

Figure 5.11: Effect of axial load variation on (a) Yield curvature, (b) Ultimate curvature, (c) Curvature ductility, (d) Yield moment, (e) Ultimate moment and (f) Peak moment capacity. All analyses performed using Response-2000.

Figure 5.11(a) and (b) shows the variation of yield and ultimate curvature values along with axial load variation. It can be observed that yield curvature increases linearly with an increase in axial load, whereas ultimate curvature decreases almost linearly following an axial load of -100 kips which correspond to 3.6% axial load index ($0.036\ A_g f'_c$) for the tested specimens. As a result, the difference between yield curvature and ultimate curvature reduces with the increase in axial load, which results in a reduction of curvature ductility for the column section. Figure 5-8(c) shows the variation of curvature ductility with respect to different axial load values. A trend similar to the ultimate curvature variation is evident where the curvature ductility reduces almost linearly with an increase in axial load. The effect of axial load on moment capacity for the column section is presented in Figure 5.11(d) through (f), where yield moment, ultimate moment, and peak moment are plotted against different axial loads. It can be seen that the moment capacity of the column section linearly increases with an increase in axial load. However, Goodnight et. al. (2016) reported no significant changes in strain values for bar buckling and spiral yielding limit state due to the variation of axial load index.

The backbone curves for all three tested specimens are shown in Figure 5.12, where specimens SVF#8 and LVF#8 experienced higher and lower axial loads in the push and pull cycles, respectively. On the other hand, specimen SCF#8 was tested under a constant axial load. Results show that specimen SCF#8 exhibited a symmetric load-displacement response, whereas specimen SVF#8 showed a lower capacity in the pull cycle of loading. The higher peak lateral strength for specimen SVF#8 in the push cycles is evident from the higher axial load, which also reiterate the findings of the numerical analyses. Moreover, the positive branch (push) of load-displacement response for specimen SVF#8 has a higher strength degradation, 20.7%, as compared to the negative branch (i.e. pull) of loading cycle, where the strength degradation was only 8.9% at the ultimate damage state. On the other hand, specimen SCF#8 has almost similar strength degradation with 18.8% and 20.2% in the push and pull cycles, respectively. However, almost a symmetric load-displacement envelope can be observed for specimen LVF#8, despite the variation in axial load. Hence, the effect of axial load variation on peak strength for the column section was insignificant. However, a variation in strength degradation was found with a maximum degradation of 26.5% in push cycle and 22.8% in the pull cycle. Moreover, specimen LVF#8 was tested under a different lateral loading protocol compared to specimen SCF#8 and SVF#8. Hence, a lack of asymmetry is arguable and need further investigation.

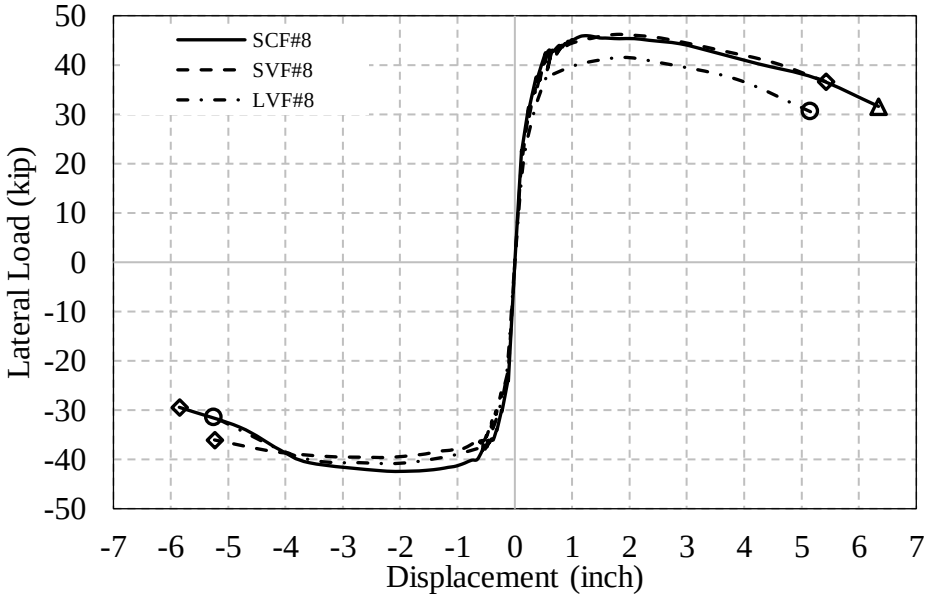

Figure 5.12: Backbone curve comparison for tested specimens

5.3.1.5 *Effect of Lateral Loading Protocol*

Specimens SVF#8 and LVF#8 were tested under two different lateral loading protocols, namely subduction zone loading protocol and conventional three cycle symmetric lateral loading protocol. Both specimens had same geometric and reinforcement details. They were tested under same axial loading protocol with the same magnitude of axial variation in the push and pull cycles.

Both specimens exhibited a ductile hysteretic load-displacement response. The maximum ductilities for specimen SVF#8 was 9.34 (5.42 inch) and -9.03 (-5.24 inch) in the push and pull cycles, respectively. On the other hand, the maximum ductility achieved by specimen LVF#8 was 8.0 (5.20 inch) for both the push as well as the pull cycle. However, higher strength degradation and higher level of damage was observed under the conventional three cycle lateral loading protocol as compared to the subduction zone loading protocol. The final damage state for specimen LVF#8 was fracture of previously buckled bars, where specimen SVF#8 only reached bar buckling in the final damage state. Peak strengths achieved for specimens SVF#8 and LVF#8 were 46.2 kips and 41.6 kips, respectively, for the push cycle. Peak strengths in the pull cycle was -39.6 kips and -40.7 kips, respectively. In the push cycle of loading, the peak lateral strength for specimen SVF#8 was 11.2% higher than for specimen LVF#8, where in the pull cycle the peak lateral strength was almost same.

5.3.2 Local Response

External Linear Variable Displacement Transducers (LVDT) were mounted on 5/16 inch diameter threaded rods inserted halfway into the column to measure the rotation and curvature along the height of the column. First of all, average rotation for any specific segment, *i* was

calculated based on the recorded displacement of the LVDT's mounted on two opposite side of the column as indicated by Equation 5.2 and as depicted in Figure 5.13. Later, average curvature for that particular segment was calculated as the segment rotation divided by the height of the segment as indicated by Equation 5.3.

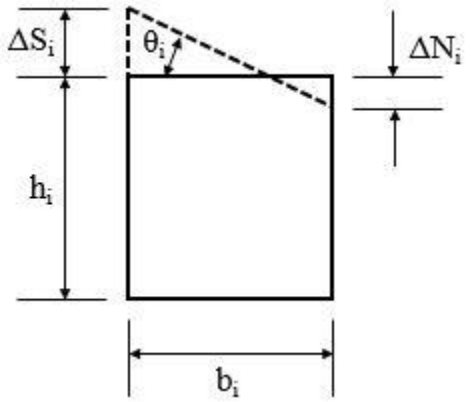

Figure 5.13: Measurement of average rotation.

$$\theta_i = (\Delta S_i - \Delta N_i)/b_i \quad \textbf{(5-2)}$$

$$\Phi_i = \theta_i/h_i \quad \textbf{(5-3)}$$

Where:

θ_i = average rotation for segment i, ΔS_i = vertical displacement measured by south LVDT, ΔN_i = vertical displacement measured by north LVDT, b_i = horizontal distance between north and south LVDT, Φ_i = average curvature for the segment and h_i = height of segment i.

5.3.2.1 *Curvature Profile*

The curvature profiles for all tested specimens are shown in Figure 5.14 (a) through (f). Both the pre-yield and post yield curvature profiles are presented to investigate the spread of plasticity along the column height. The pre-yield curvature profiles shown in Figure 5-11 (a), (c) and (e) implied that significant spread of plasticity along the column height exists, which imitate numerous crack formation at different heights in the column. For specimen SCF#8, the maximum height of flexural crack formation was 52 inch, which supports the curvature profile where significant curvature activity can be traced up to 45 inch from the column base. Similar trends were observed for specimens SVF#8 and LVF#8, where cracks were found up to 55 inch from the column base. Experimental observation showed stabilization of crack following the yield displacement cycles and damage started to concentrate at the base of the column. The post-yield curvature profiles imply similar results, where most of the plastic deformation is concentrated

within 10 inch height from the column base. For specimen SCF#8, the magnitude of column curvature in both the push and pull cycles was similar. On the other hand, the pull cycle of loading experienced higher curvature for specimens SVF#8 and LVF#8. It was mentioned in Section 5.3.1.4 that increased axial load reduces the ultimate curvature and hence reduces the curvature ductility. Hence, it can be inferred that higher axial load in the push cycles for the latter two specimens resulted in a reduced curvature for these cycles.

5.3.2.2 *Strain Profile*

The concrete strain profiles for all the three specimens as computed from the curvature instrumentation are shown in Figure 5.15 (a) through (f). All the strain values were computed at the face of the column for the push and pull cycles of loading. Only the compressive strain values are reported here and were used for limit state analysis. The pre-yield strain profile as shown in Figure 5.15 (a), (c) and (e) reveals considerable spread of concrete strain along the height of the column, where the post-yield strain profiled show that strains are concentrated within 15 inch from the column base. Visual observation during the experiment showed maximum concrete spalling up to a height of approximately 18 inch from the column base. It can also be observed that specimen SCF#8 exhibits lower ultimate strain values than the other two specimens. It should be noted that slip occurring in the column base is included in the computed strain for the first 3-inch segment from the column-footing interface. Therefore, the actual concrete strain values for the initial 3-inch segment is less than the herein reported concrete strain values and their impacts are well pronounced at higher displacement ductility level.

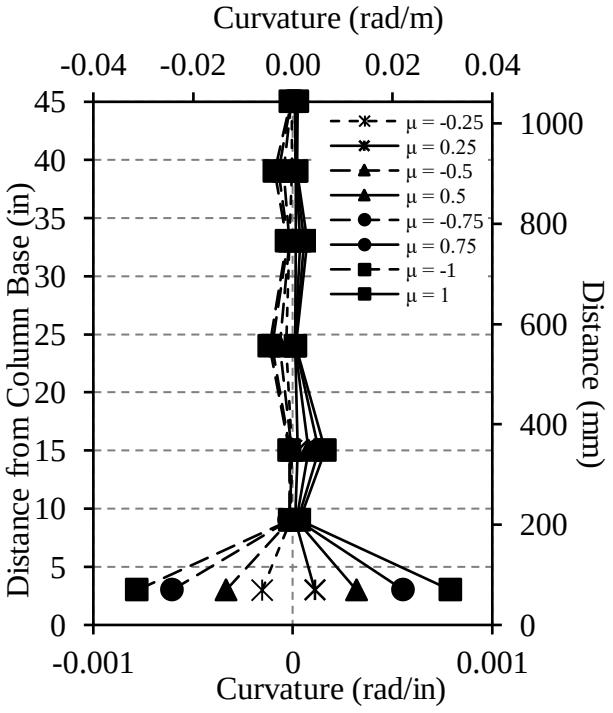

(a)

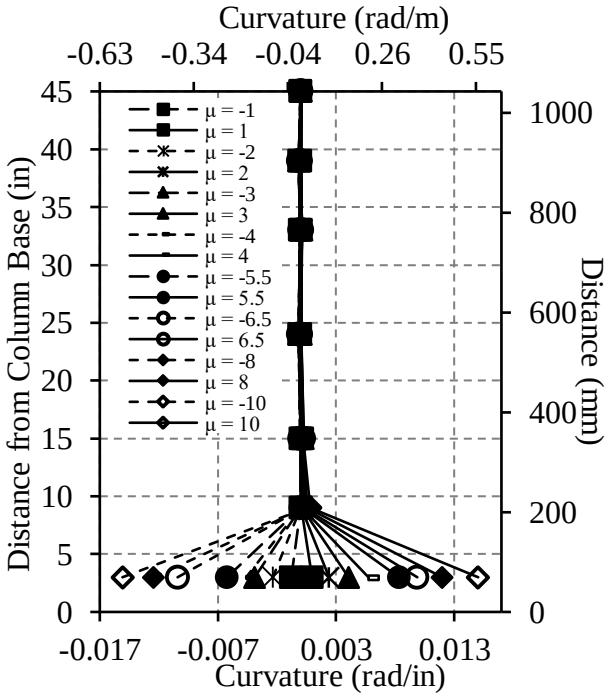

(b)

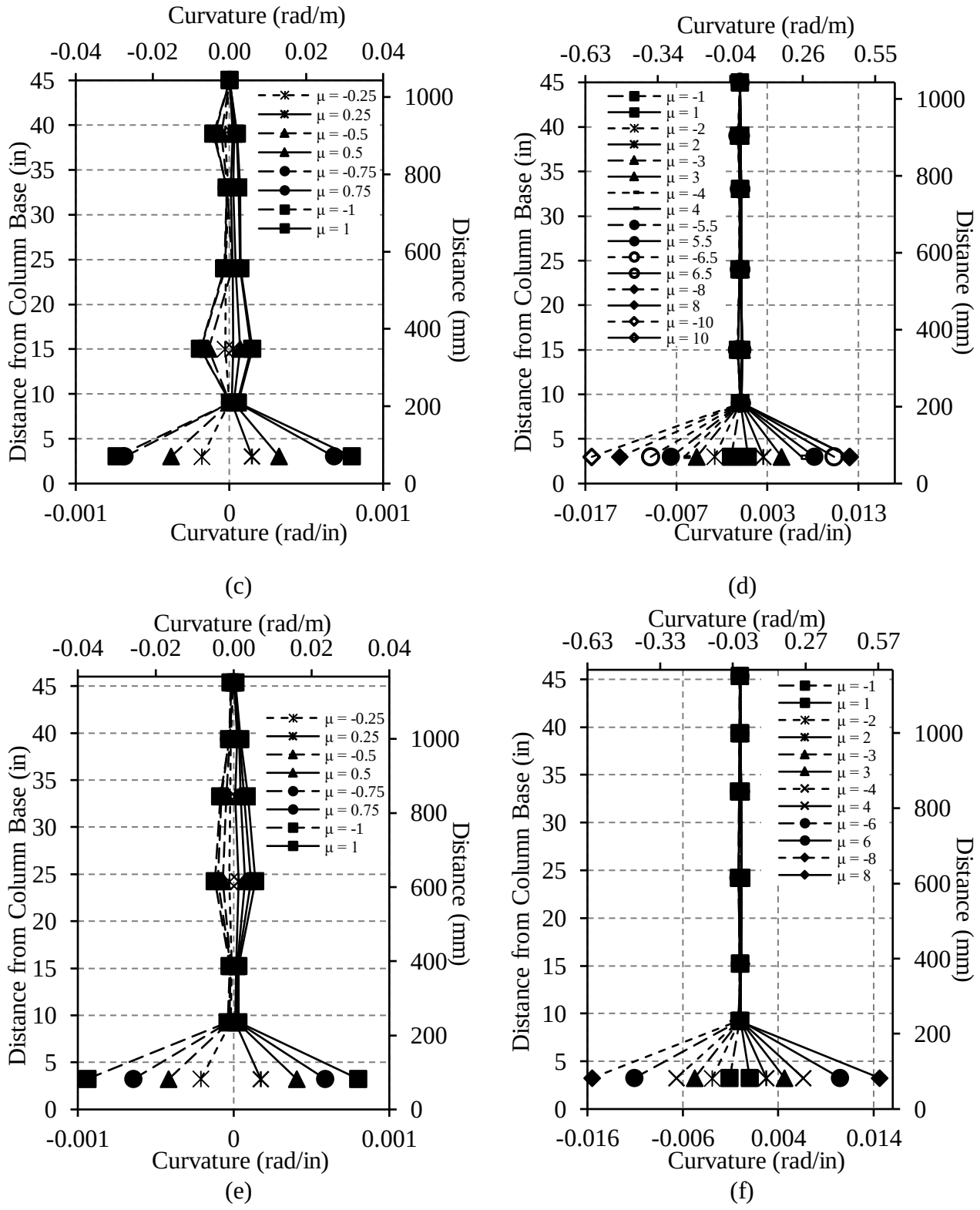

Figure 5.14: Curvature profile for (a) Pre-yield SCF#8 (b) Post-yield SCF#8, (c) Pre-yield SVF#8, (d) Post-yield SVF#8, (e) Pre-yield LVF#8 and (f) Post-yield LVF#8

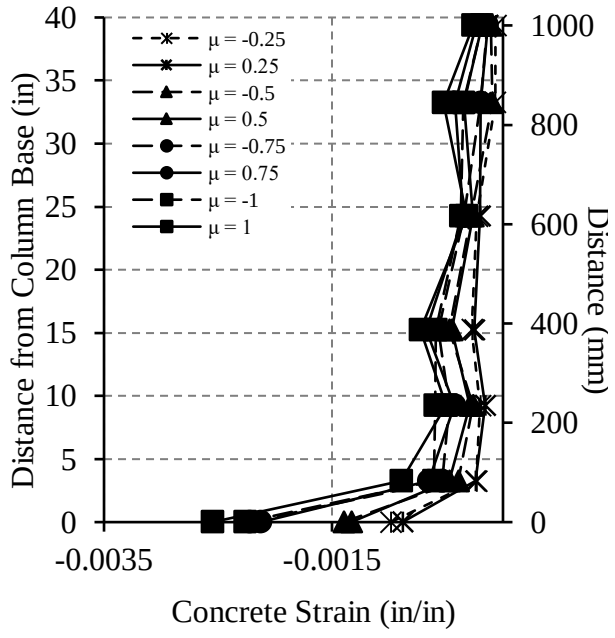
Distance from Column Base (in)
Distance (mm)
Concrete Strain (in/in)
μ = -0.25
μ = 0.25
μ = -0.5
μ = 0.5
μ = -0.75
μ = 0.75
μ = -1
μ = 1
0
5
10
15
20
25
30
35
40
0
200
400
600
800
1000
-0.0035
-0.0015

(a)

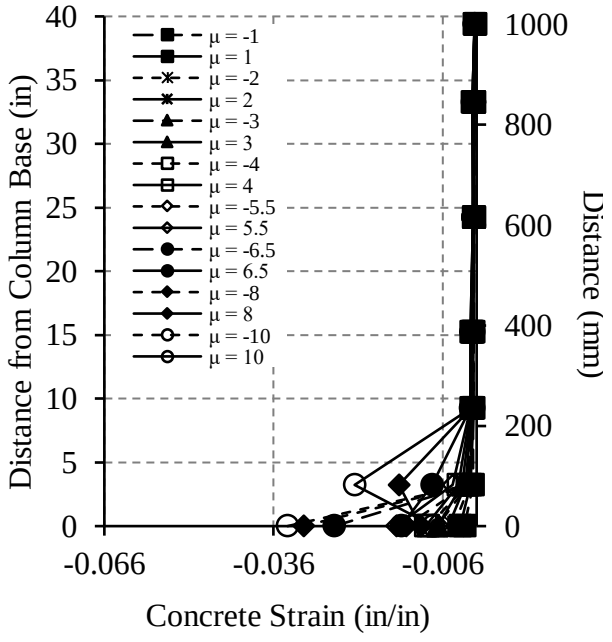
Distance from Column Base (in)
Distance (mm)
Concrete Strain (in/in)
μ = -1
μ = 1
μ = -2
μ = 2
μ = -3
μ = 3
μ = -4
μ = 4
μ = -5.5
μ = 5.5
μ = -6.5
μ = 6.5
μ = -8
μ = 8
μ = -10
μ = 10
0
5
10
15
20
25
30
35
40
0
200
400
600
800
1000
-0.066
-0.036
-0.006

(b)

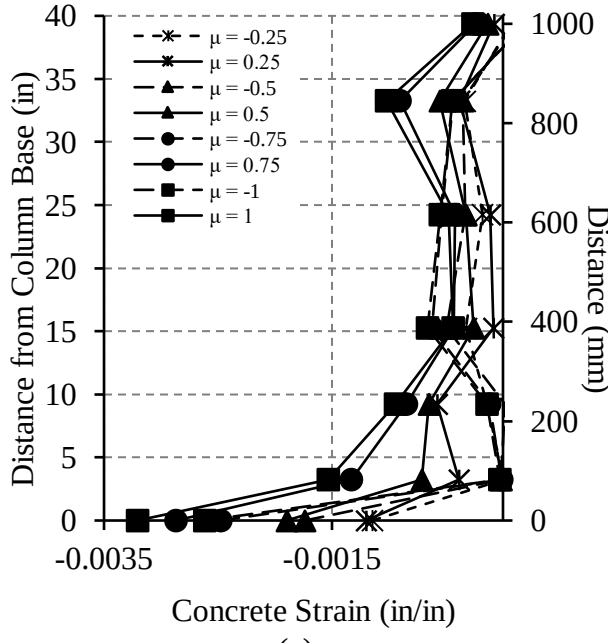
Distance from Column Base (in)
Distance (mm)
Concrete Strain (in/in)
μ = -0.25
μ = 0.25
μ = -0.5
μ = 0.5
μ = -0.75
μ = 0.75
μ = -1
μ = 1
0
5
10
15
20
25
30
35
40
0
200
400
600
800
1000
-0.0035
-0.0015

(c)

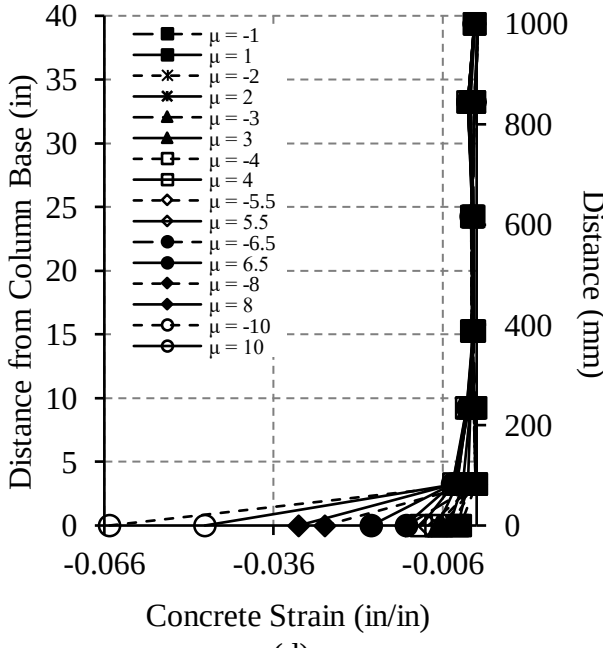
Distance from Column Base (in)
Distance (mm)
Concrete Strain (in/in)
μ = -1
μ = 1
μ = -2
μ = 2
μ = -3
μ = 3
μ = -4
μ = 4
μ = -5.5
μ = 5.5
μ = -6.5
μ = 6.5
μ = -8
μ = 8
μ = -10
μ = 10
0
5
10
15
20
25
30
35
40
0
200
400
600
800
1000
-0.066
-0.036
-0.006

(d)

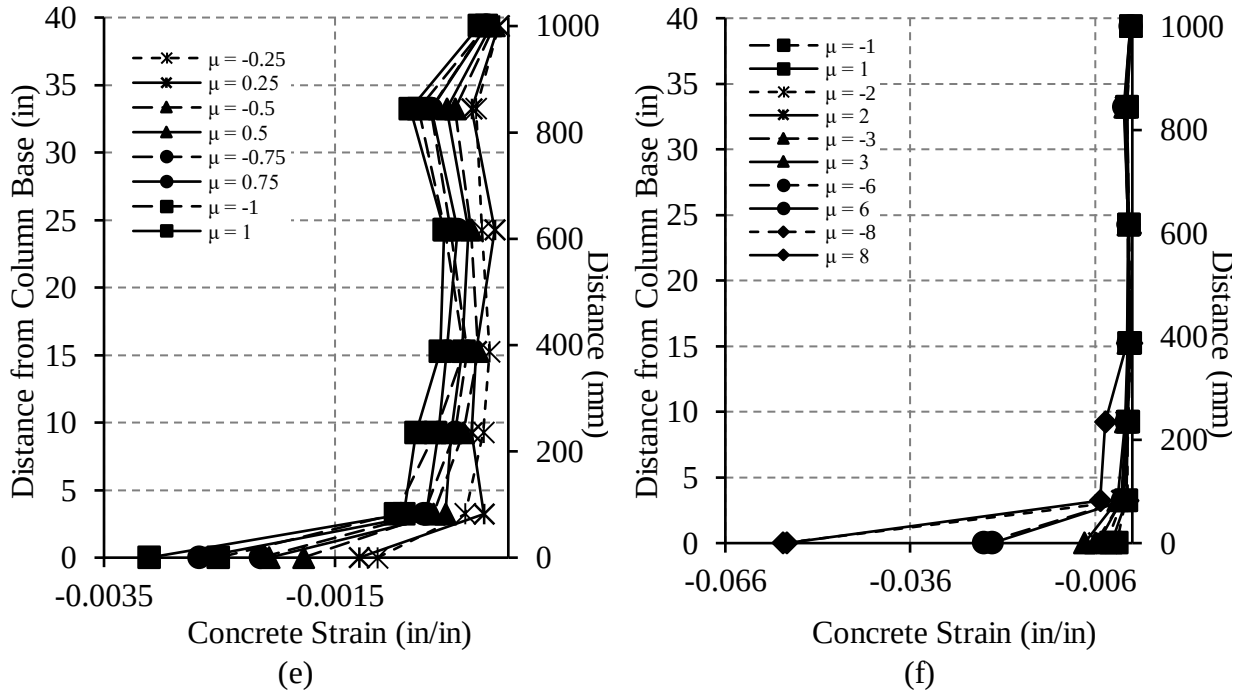

Figure 5.15: Concrete compressive strain profiles for (a) Pre-yield SCF#8 (b) Post-yield SCF#8, (c) Pre-yield SVF#8, (d) Post-yield SVF#8, (e) Pre-yield LVF#8 and (f) Post-yield LVF#8

6.0 IMPACTS ON DUAL DESIGN CRITERIA

6.1 GENERAL

The seismic design philosophy for new bridges or retrofit of existing bridges has evolved from strength-based design to a target performance-based design, which is also known as "Performance Based Seismic Design" (PBSD). PBSD is defined as the design methodology to reliably achieve a targeted performance objective for a specific bridge category (importance category). Each of these performance objectives are specified for a particular hazard level, which are usually referred to in terms of probability of exceedance. Moreover, the PBSD methodology uses performance for a wide range of hazard levels, whereas the traditional strength-based design follows a single hazard and performance level. The performance objectives are usually defined with respect to component parameters (e.g. rebar buckling) or, global structural parameters (e.g. stability). Both qualitative and quantitative definitions of performance levels are in use to define specific performance objectives. Engineering limit states (e.g. material strain limits) are usually used to define quantitatively each aspect of the performance level.

The growing need to define performance objectives in terms of engineering limit states has led to many studies that have resulted in a multi-level bridge design methodology. Such a methodology has been adopted and implemented by a few departments of transportation, such CALTRANS, Oregon DOT, and South Carolina DOT (National Cooperative Highway Research Program. 2013). In this section, the performance metrics for performance-based seismic design and retrofit of bridges based on ODOT's requirements are compared to the observations of the tested specimens.

6.2 ODOT DESIGN PHILOSOPHY

The Oregon DOT uses a displacement-based design philosophy with a two-level performance criterion, namely "Life Safety" and "Operational", for the seismic design of new bridges. In order to satisfy the life safety performance objective, new bridges should be designed for a 1000-year return period earthquake (7% probability of exceedance in 75 years), whereas a full rupture Cascadia subduction zone earthquake should be used to satisfy the operational performance objective. Hence, bridge performance is described with two discrete performance levels and two seismic hazards, as shown in Table 6.1.

Evaluation of existing bridges also uses material strain-limit values to identify the performance objective under stated seismic hazard levels. Values specified by ODOT are listed in Table 6.1. However, the strain limits at the operational performance objectives are defined in terms of concrete strain and do not account for residual crack widths, which are usually defined in terms of steel strain limit values. In addition to the gap in defining qualitative performance levels with respect to damage sequences for existing bridges, strain limit states at the operational performance objective lack an experimental basis.

Table 6.1: ODOT's Current Performance Criteria and Strain Limit States (Oregon Department of Transportation 2019)

Performance Objective	Seismic Hazard (Return Period)	New Bridge Design		Existing Bridge Evaluation	
		Steel Strain	Concrete Strain	Concrete Strain (Inadequate Hoops and Hoop Spacing)*	
				Inadequate Lap Splice**	Adequate Lap Splice
Operational	CSZE	$\varepsilon_s \leq 2\varepsilon_{sh}$	$\varepsilon_{cc} = 0.005$	0.002	0.002
Life Safety	1000-year	$\varepsilon_s \leq \varepsilon^R_{su}$	$\varepsilon_{cc} = 0.9\ \varepsilon_{cu}$	0.003	0.004

*As adequate hoops are qualified those that meet the definition of "seismic hooks" in Article 8.8.9 of (American Association of State Highway Transportation Officials (AASHTO), 2011) *Guide Specifications for Seismic Bridge Design* and are spaced no more than 6 inches apart.
** As adequate lap splice are qualified those that meet the requirements of Article 5.10.8.4.3a of AASHTO (2017) *LRFD Bridge Design Specifications* for Class B splice.

Where:

ε_s is the reinforcing steel strain; ε_{sh} is the reinforcing steel strain at the onset of strain hardening; ε^R_{su} is the reduced ultimate tensile strain in the reinforcing steel; ε_{cc} is the strain in the confined section of columns; ε_{cu} is the ultimate concrete strain computed using Mander's model

Figure 6.1 illustrates the four-level performance criteria adapted from (Moehle and Deierlein 2004) that satisfy ODOT requirements.

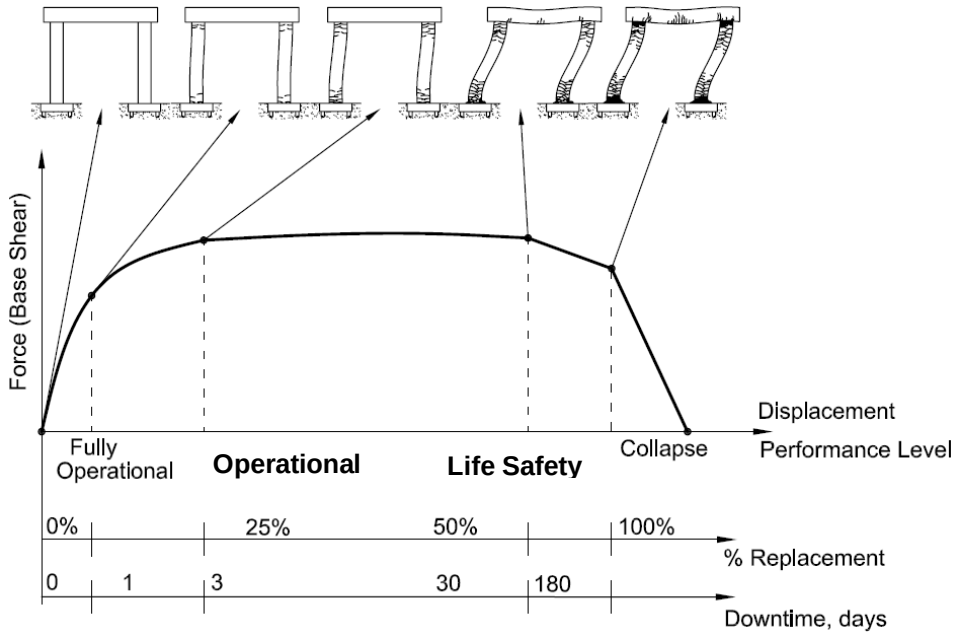

Figure 6.1: Visualization of PBSD (after Moehle and Deierlein 2004), adaptation to ODOT's requirements

On the other hand, for the seismic retrofit design of existing bridges, ODOT has adopted the design philosophy according to the publication "Seismic Retrofitting Manual for Highway Structures, Part 1-Bridges" (Federal Highway Administration 2006). The two-level performance objectives adopted by ODOT are presented in Table 6.2. It should be noted that the performance objectives for the lower-level ground motion as adopted by ODOT differs from the seismic retrofit manual guideline (Federal Highway Administration 2006).

Table 6.2: Minimum Performance Level for Retrofitted Bridges Adopted by ODOT

Earthquake Ground Motion	**Bridge Importance And Service Life Category**					
	Standard			**Essential**		
	ASL 1	**ASL 2**	**ASL 3**	**ASL 1**	**ASL 2**	**ASL 3**
Lower Level Ground Motion* Cascadia Subduction Zone Earthquake –Full Rupture	PL0	PL2	PL2	PL0	PL2	PL3
Upper Level Ground Motion 7 percent probability of exceedance in 75 years; Return period is about 1,000 years	PL0	PL1	PL1	PL0	PL1	PL2

*Requirements differ from the seismic retrofit manual guideline (Federal Highway Administration 2006).

Where:

ASL refers to Anticipated Service Life and the range of service life for ASL 1 is 0-15 years, ASL 2 is 15-60 years and ASL 3 is >50 years.

The stated performance levels (PL) are defined as follows:

- Performance Level 0 (PL0): No minimum level of performance is recommended.
- Performance Level 1 (PL1): Life safety. Significant damage is sustained during an earthquake and service is significantly disrupted, but life safety is assured. The bridge may need to be replaced after a large earthquake.
- Performance Level 2 (PL2): Operational. Damage sustained is minimal and full service for emergency vehicles should be available after inspection and clearance of debris. Bridge should be repairable with or without restrictions on traffic flow.
- Performance Level 3 (PL3): Fully Operational. Damage sustained is negligible and full service is available for all vehicles after inspection and clearance of debris. Any damage is repairable without interruption to traffic.

6.3 EXPERIMENTAL STRAINS

In this section, results obtained from past research at Portland State University are synthesized and compared with the results obtained from the current project.

6.3.1 Square RC Column Tests [Mehary & Dusicka (2015)]

Mehary and Dusicka (2015) experimentally investigated the performance of full-scale square reinforced concrete columns using four test specimens intended to represent typical bridge columns in the state of Oregon, as illustrated in Figure 6.2. All the four specimens had the same material properties, cross-sectional dimensions, and reinforcement ratios; and were tested under quasi-static reverse cyclic loading. The variables considered for the testing program included the lateral loading protocol (conventional laboratory and subduction loading protocol), applied axial loading (8% to 17% of the gross cross sectional strength), and the column conditions (as-built and retrofitted).

Each column specimen had 4 - #10 longitudinal reinforcement bars, on in each of the four corners. The specimens had #3 stirrups with 90^0 hooks, at 12 inches center-to-center spacing, and 2 inches of concrete cover confining the column core. Dowels extended through the footing to 36 inches from the top of the footing. The longitudinal rebar extended through the stubs to 0.6 inches from the end.

Normal weight concrete was used to construct the test specimens with a target 28-day strength of 3,500 psi. All reinforcing steel used to construct the test specimens consisted of ASTM (ASTM International 2018) Grade 60 deformed bar.

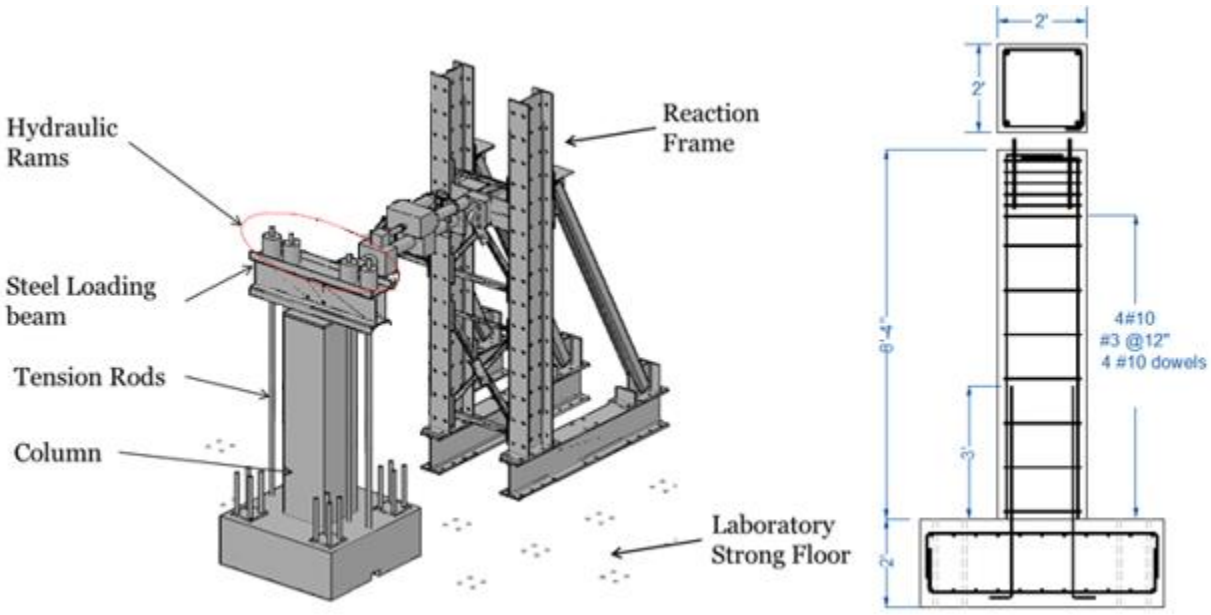

Figure 6.2: Test setup and geometry of RC column specimen [Mehary & Dusicka (2015)]

Figure 6.3 shows the lateral load vs. displacement response of the tested RC square column and Table 6.3 lists material values for specific performance parameters.

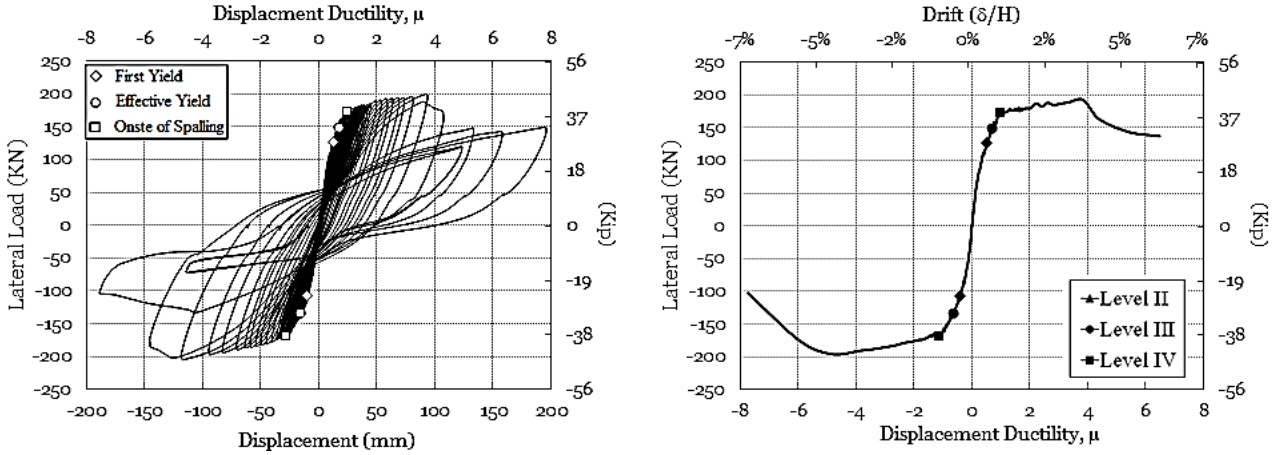

(a) (b)

Figure 6.3: RC square column performance. (a) Force-displacement hysteresis curve and (b) force-displacement envelope [Mehary & Dusicka (2015)]

Table 6.3: Bridge Performance Parameters (Limit States) for RC Square Column [Dusicka & Lopez (2016)]

Level	Limit State	Steel Strains (ε_s)	Concrete strains* (ε_c)	% Drift	Ductility (μ)
I	Cracking	0.00017	0.0004	0.26	0.4
II	First Yield	0.0024	0.0016	0.46	0.8
III	Effective Yield	x	x	0.60	1
IV	Onset of Spalling	x	x	0.86	1.4
V	Buckling/Rupture	x	x	x	x

* The extreme concrete compressive strains of the columns were obtained using curvature data.

Strain for performance levels III, IV and V could not be computed due to the failure of the strain gauges prior to these levels. Rocking at the base of the column was observed, where a cold joint between the column and footing exists, which made acquiring those strains impossible.

6.3.2 RC Bent Tests [Gallardo (2017)]

In this section, the performance of a half-scale RC bridge bent retrofitted utilizing Buckling Restrained Braces (BRBs) is summarized. The experimental program consisted of three tests evaluating half-scale models of a RC bridge bent as illustrated in Figure 6.4. The first two experiments consisted of different BRB options in an effort to assess the influence of BRB stiffness on the overall structural performance. In the third test, the bent was evaluated in the as-built non-retrofitted condition, hereinafter referred to as "As-built".

The longitudinal reinforcing steel used to construct the test specimens consisted of Grade 40, f_y = 40 ksi, f_u = 60 ksi following ASTM (ASTM International 2018). The average yield stress for the longitudinal reinforcement determined by standard coupon tests was 50 ksi. The transverse steel consisted of deformed wire D5 conforming to ASTM (ASTM International 2007).

Normal weight concrete was used to construct the test specimens with a target 28-day strength (f'_c) of 3,300 psi. Standard compression testing of 6-inch by 12-inch concrete cylinders was performed at 7-day, 28 days and at the day of test completion. The compressive strength at testing day was approximately 4,800 psi.

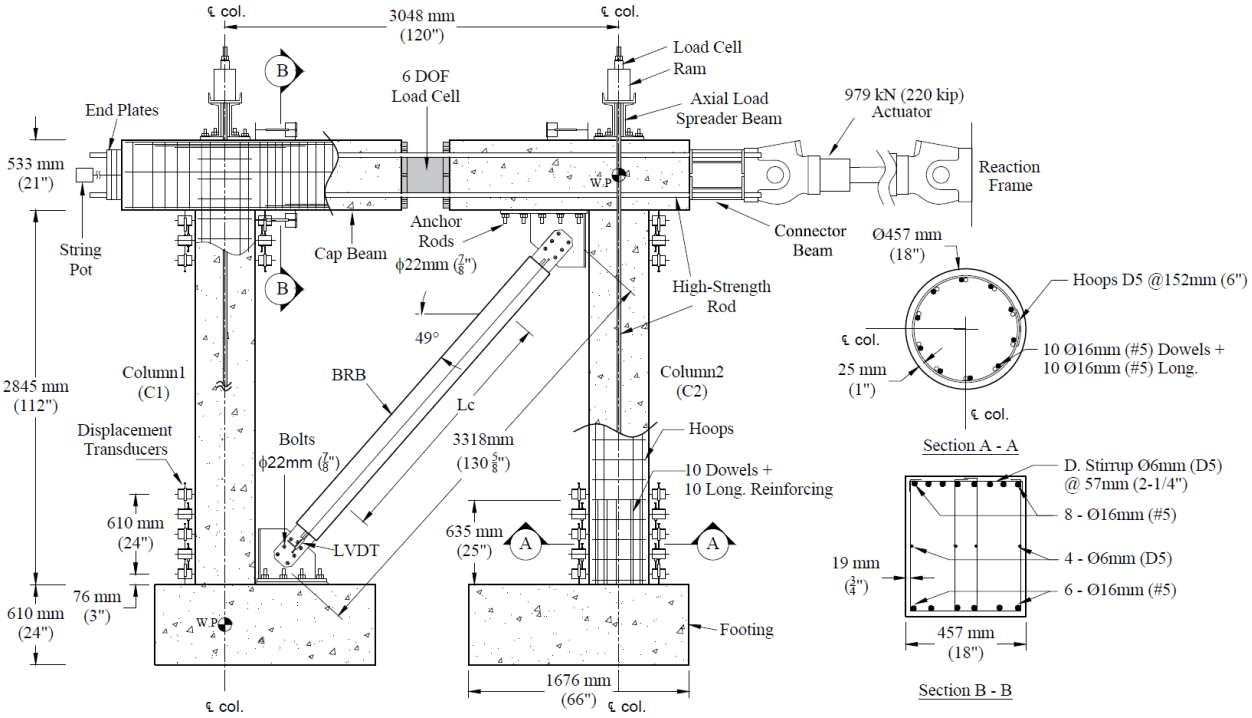

Figure 6.4: Reinforced concrete bent test setup [Gallardo (2017)]

Figure 6.5 shows the lateral load vs. displacement response of the tested RC square column and Table 6.4 lists material values for specific performance parameters.

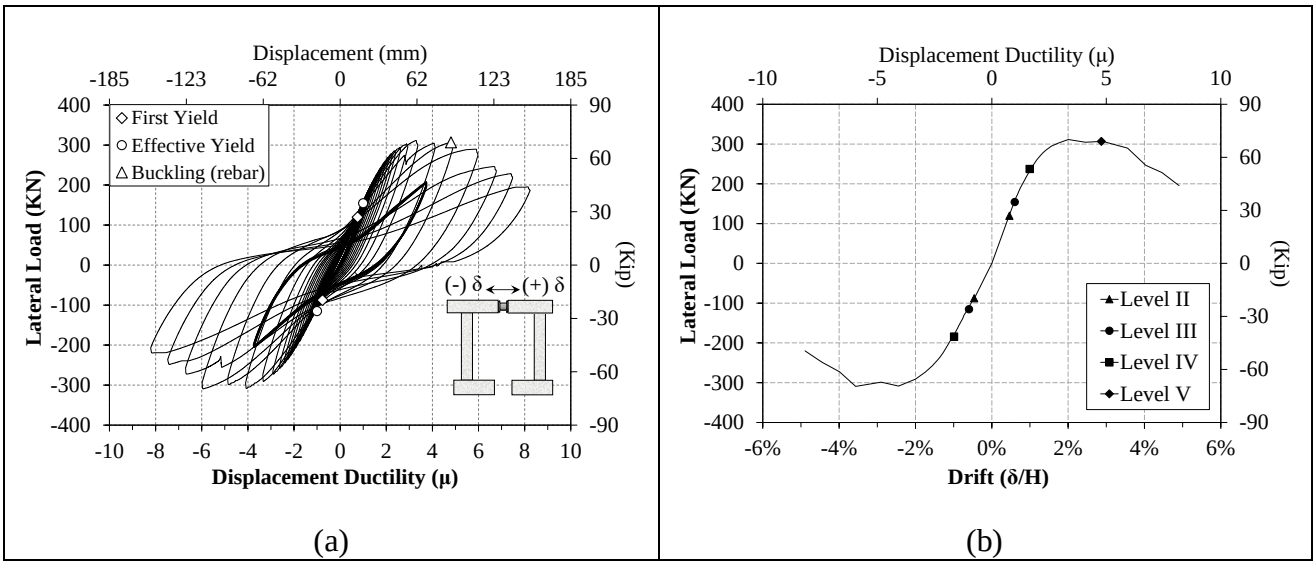

Figure 6.5: RC bent performance. (a) Force-displacement hysteresis curve and (b) force-displacement envelope [Gallardo (2017)]

Table 6.4: Bridge Performance Parameters (Limit States) for RC Bent [Gallardo (2017)]

Level	Limit State	Steel Strains (ε_s)	Concrete strains* (ε_c)	% Drift	Ductility (μ)
I	Cracking	0.0008	0.0007	0.21	0.3
II	First Yield	0.0017	0.0012	0.46	0.8
III	Effective Yield	0.0020	0.0017	0.60	1
IV	Onset of Spalling	0.010	0.0042	0.99	1.7
V	Buckling/Rupture	0.048	0.0080	2.87	4.8

* The extreme concrete compressive strains of the columns were obtained using the results from the strains in the reinforcing steel and a linear strain profile for a circular section. The actual values of concrete strain in the confined section are expected to be lower since these values are the maximum compressive strain and not the strain in the confined section.

6.3.3 Circular RC Column Tests [Dusicka & Lopez (2016)]

In this section, the dynamic performance of scaled circular RC bridge columns is summarized. The experimental program consisted of six test specimens intended to represent scaled models of typical circular bridge columns as illustrated in Figure 6.6. All six specimens had the same material properties, cross-sectional dimensions, and reinforcement ratios. The variables in the testing program were ground motion duration and lap splice length.

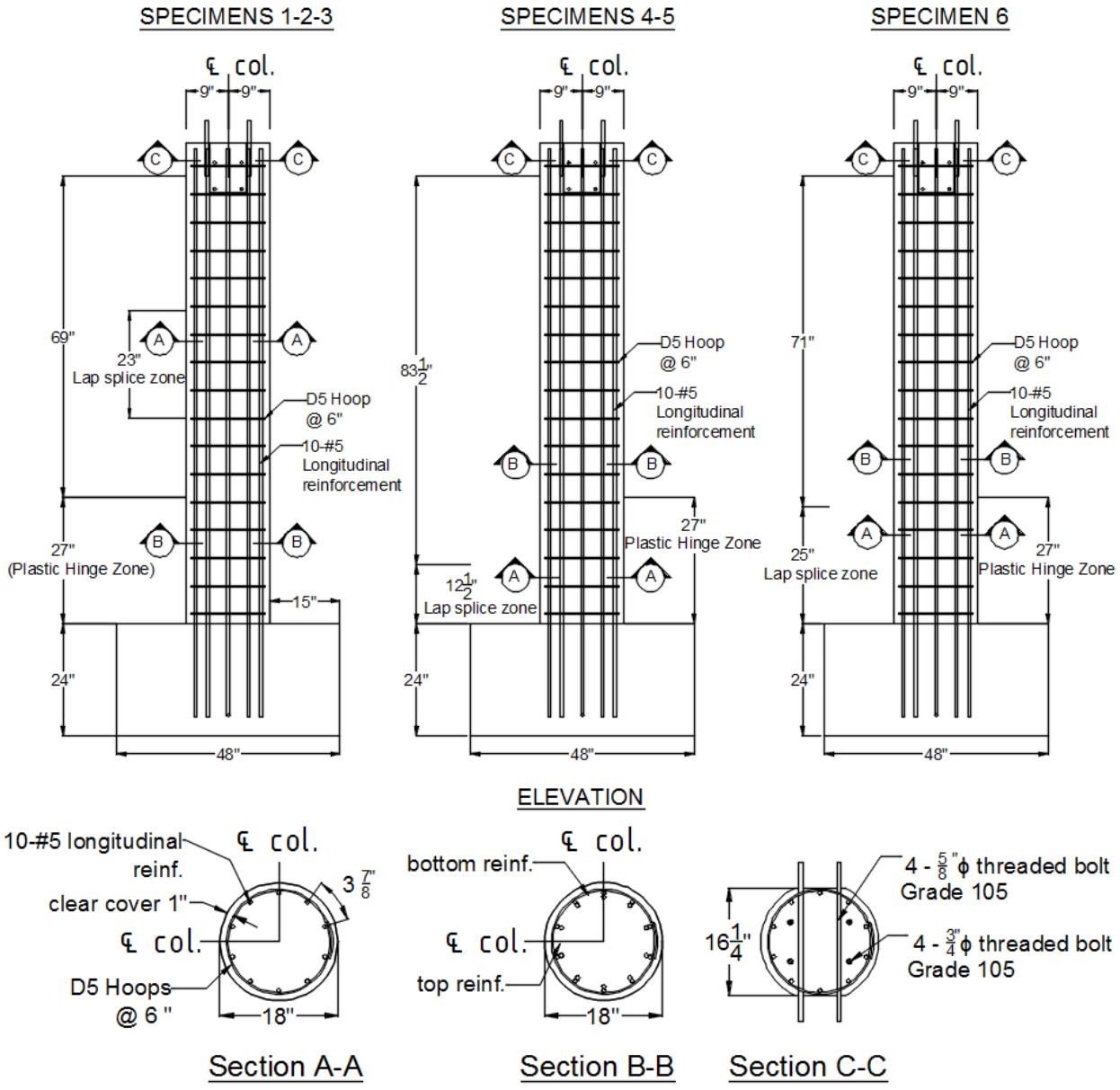

Figure 6.6: Geometry and reinforcement of RC Bridge column specimens [Dusicka & Lopez (2016)]

The longitudinal reinforcing steel used to construct the test specimens consisted of Grade 40, f_y = 40 ksi, f_u = 60 ksi conforming to ASTM (ASTM International 2018). The average yield stress for the longitudinal reinforcement determined by standard coupon tests was 50 ksi. The transverse steel consisted of deformed wire D5 conforming the ASTM (ASTM International 2018).

Normal weight concrete was used to construct the test specimens with a target 28-day strength (f'_c) of 3,300 psi. Standard compression testing of 6-inch by 12-inch concrete cylinders was performed at 7-day, 28 days and at the day of test completion. The day of testing the compressive strength was 4,700 psi approximately.

Figure 6.7 shows the lateral load vs. displacement response of the tested RC square column and Table 6.5 lists material values for specific performance parameters.

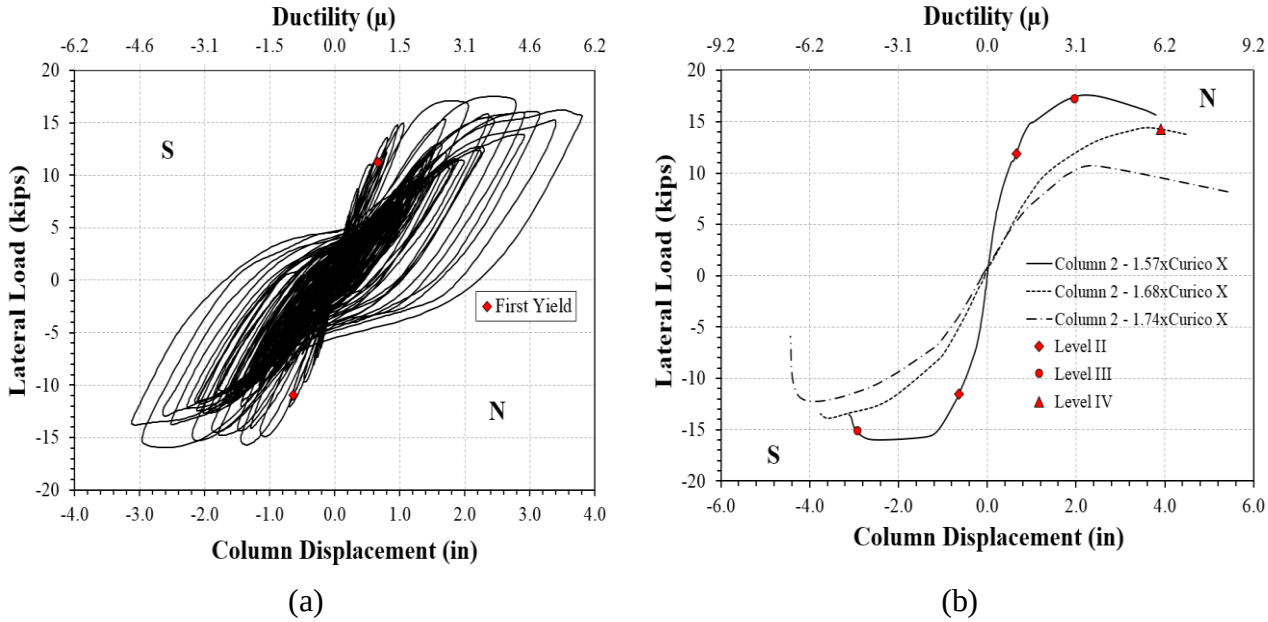

(a) (b)

Figure 6.7: Circular RC column performance. (a) Force-displacement hysteresis curve and (b) force-displacement envelope [Dusicka & Lopez (2016)]

Table 6.5: Bridge Performance Parameters (Limit States) for Circular RC Columns [Dusicka & Lopez (2016)]

Level	Limit State	Steel Strains (ε_s)	Concrete strains* (ε_c)	% Drift	Ductility (μ)
I	Cracking	0.0002	0.0004	0.20	0.3
II	First Yield	0.0013	0.0008	0.68	1.0
III	Effective Yield	-	-	-	-
IV	Onset of Spalling	0.0117	0.0046	2.55	3.8
V	Buckling/Rupture	0.0402	0.0099	4.08	6.0

* The extreme concrete compressive strains of the columns were obtained using the results from the strains in the reinforcing steel and a linear strain profile for a circular section. The actual values of concrete strain in the confined section are expected to be lower since these values are the maximum compressive strain and not the strain in the confined section.

6.3.4 Square RC Column Tests (This Research) (4 - #8 Rebar)

The current experimental program investigated the seismic performance of square RC column-footing sub-assemblies consisting of three test specimens as illustrated in Figure 4.2. All three specimens had the same material properties, cross-sectional dimensions, and reinforcement ratios. The variables in the testing program include lateral and axial loading protocols. The longitudinal reinforcement in each prototype column consisted of 4 - #8 rebar in four corners. These were combined with #3 stirrups with 90^0 hooks, at 12 inches center-to-center spacing, and

2 inches of concrete cover confining the column core. Dowels extend through the column to 47 inches from the top of the footing.

Normal weight concrete was used to construct the test specimens with a target 28-day strength of 3,300 psi. Standard compression testing of 6-inch by 12-inch concrete cylinders was performed at 7-day, 28 days and at the day of test completion. Average 28-day compressive strengths were 4,740 psi for the column and 5,410 psi for the footing. All reinforcing steel used to construct the test specimens consisted of Grade 60 conforming to ASTM (ASTM International 2018).

The concrete and steel strain values were computed for associated damage level and were finally used to define the performance limits based on the computed strain values. Lateral force and displacements associated with different damage levels are presented in Table 6.6.

Table 6.6: Lateral Force and Displacements for Different Damage Levels

Damage Level	SCF#8			SVF#8			LVF#8		
	Force (kip)	Disp. (inch)	μ_Δ	Force (kip)	Disp. (inch)	μ_Δ	Force (kip)	Disp. (inch)	μ_Δ
Cracking	-28.7	-0.24	-0.46	-26.9	-0.238	-0.41	28.0	0.318	0.49
First Yield	-41.9	-0.42	-0.81	39.0	0.483	0.83	32.6	0.446	0.69
Residual Crack > 1.0 mm	N/M	N/M	N/M	-36.4	-1.18	-2.03	-38.7	-1.96	-3.00
Onset of Spalling	-41.1	-1.87	-3.59	44.1	1.34	2.31	38.8	1.97	3.00
Bar Buckling	-26.5	-5.91	-11.4	-33.3	-5.30	-9.13	30.5	5.18	7.96
Bar Fracture	N/A	N/A	N/A	N/A	N/A	N/A	-27.9	-5.34	-8.21

The concrete and steel strain values as obtained from curvature instrumentation and strain gauges are presented in Table 6.7 for different damage levels. The steel strain values reported here are the tensile strain in the steel rebar recorded at the end of the loading cycle for each damage level. The maximum recorded strain from all of the gauges was considered. However, steel strain data for the higher damage levels were not reported as the strain gauges in the critical location of the column failed prior to these cycles. All rebar strain data reported here for specimen SCF#8 correspond only to the north side of the column. On the other hand, the concrete strain reported was the strain at the extreme fiber of concrete and was derived from the measurements recorded with linear potentiometer at different sections. The maximum concrete strain was observed at the bottom 3-inch section. The damage level and associated strain values were later used in Section 6.4 to define the performance objective for bridge plastic hinge region.

The strain values for initial damage levels (cracking and first yield) were comparable. However, a significant variation in strain values for the spalling damage level was observed. Specimen SVF#8 experienced the lowest rebar and concrete strain values and it was found that the definition for the spalling initiation point for this specimen was different from the others. Further investigation showed that the spalling in specimen SVF#8 was initiated by a vertical

crack generated at the southeast corner (column face perpendicular to loading direction) consistent with lap splice failure of the dowel bar. On the other hand, spalling in specimens SCF#8 and LVF#8 was due to the crushing of concrete in the north face (column face parallel to loading direction). The rebar and concrete strains for specimen SVF#8 at the onset of spalling due to concrete crushing were found to be 0.0379 and 0.00859, respectively. These values were comparable to the spalling strain values for specimens SCF#8 and LVF#8. However, the qualitative definition of damage levels in performance-based design ensure the functionality of bridges following an earthquake event and hence spalling (flaking on east face) of concrete due to lap splice failure cannot be neglected. It was observed that the southeast corner of the specimen SVF#8 was completely spalled off along with crushing of concrete in the later loading cycles, which exposed the rebar in the corner. Although the damage state started due to lap splice failure instead of concrete crushing, it later imitated a typical spalling damage progression scenario. Hence, it was decided to incorporate the flaking of concrete under a spalling initiation damage state instead of defining lap splice failure as an individual damage state.

Table 6.7: Measured Strains for Different Damage Levels

Damage Level	Steel Strain (ε_s)			Concrete Strain (ε_c)		
	SCF#8	**SVF#8**	**LVF#8**	**SCF#8**	**SVF#8**	**LVF#8**
Cracking	0.00134	0.00128	0.00191	0.00145	0.0017	0.00207
First Yield	0.00234	0.00235	0.00258	0.00222	0.00298	0.00268
Residual Crack Width > 1.0mm	N/M	0.0173	> 0.03	N/M	0.00473	0.00602
Spalling Initiation	0.0348	0.02	0.04333	0.00856	0.00542	0.00776
Loss of Cover	N/M	N/M	N/M	0.034	0.048	0.019
Bar Buckling	N/M	N/M	N/M	0.0741	0.0651	0.0417
Bar Rupture	N/A	N/A	N/M	N/A	N/A	0.0567

Each of the damage levels and corresponding strain values were scrutinized to define performance objectives and specific concrete and rebar strain limit values associated with them. While strain limit values for each of these damage states could be defined through statistical analysis using, e.g. the average minus two standard deviations, due to the scarcity of available data points, the lowest recorded strains from all three tested specimens was used. Table 6.8 lists recommended strain values for each damage state with a single concrete strain and rebar strain based on the lowest recorded strain values for individual damage level as listed in Table 6.7.

Table 6.8: Recommended Material Strain Values for Different Damage Levels in Substandard Square RC Columns

Level	Limit State	Steel Strains (ε_s)	Concrete strains* (ε_c)	% Drift	Ductility (μ)
I	Cracking	0.0012	0.0015	0.25	0.50
II	First Yield	0.0023	0.0022	0.43	0.75
III	Effective Yield	0.0025	0.0034	0.60	1.00
IV	Res. Crack Width > 1.0mm	0.017	0.0047	1.10~1.90	2.0~3.0
	Spalling Initiation	0.02	0.0054	1.30~1.90	2.0~3.5
V	Loss of Cover	N/M	0.019	3.50~6.50	>6.0
	Buckling/Rupture	N/M	0.042	5.0~6.0	>8.0

*The extreme concrete compressive strains of the columns were obtained using the results from the curvature instrumentation and considering a linear strain profile for a square section. The actual values of concrete strain in a confined section are expected to be lower since these values are the extreme fiber compressive strain and not the strain in the confined section.

For specimen SVF#8 and LVF#8, the onset of cover spalling was observed in the previous loading cycle of the specified residual crack width exceedance. However, for specimen SCF#8, residual crack width data were not recorded and hence the operational limit state for this specimen was considered as the onset of cover concrete spalling.

6.4 PERFORMANCE LIMIT STATES

The primary objective of this experimental program was to define different damage states in terms of material strain limits and hence to develop strain-based 'operational' and 'life safety' limit states. The Operational performance objective was defined to keep a bridge functional following an earthquake. Hence, the 'operational' performance limit was defined as the onset of cover concrete spalling and/or formation of a residual crack width exceeding the limit of 1.0 mm, which will require some level of intervention for the long-term serviceability of the bridges. On the other hand, the 'life safety' performance limit was defined to limit complete collapse of a bridge as the result of an earthquake event. The damage states associated with this performance limit are usually defined by extensive core concrete crushing and/or bar buckling/fracture of rebar. However, the 'life safety' performance level can be defined in a different fashion for existing reinforced concrete structures based on the progression of damage and ultimate failure mode. The 'life safety' damage state here was defined as the point of complete loss of cover concrete and buckling of longitudinal rebar. Subsequently, the two performance limits states are discussed in more detail.

6.4.1 Operational Performance Level

This experimental program defined the operational concrete strain as the extreme fiber compressive strain associated with the initiation of cover concrete spalling, whereas the operational steel strain was defined by the peak tensile strain reached before the exceedance of 1.0 mm residual crack width. The lowest recorded concrete compressive strain and steel tensile

strain values from the three different specimens as presented in Table 6.8 were later used to define the strain limits for two performance objectives. Table 6.9 presents the experimental concrete and rebar strain values for the two performance objectives and compares the strain values with the ODOT specified limit states for the design of new bridges and evaluation of existing bridges. It should be noted that the experimentally obtained concrete strain values are the compressive strain at the face of the column and do not represent the core concrete strain values. Whereas, ODOT specified concrete strain limits for the design of new bridges are the compressive strain at the core of the column.

The experimentally obtained steel strain values for the operational performance objective was lower than the ODOT specified steel strain value for design of new bridges. This experimental program defines the operational performance level in terms of residual crack width exceeding 1.0 mm whereas ODOT specified strain value correspond to the onset of cover concrete crushing. Further investigation showed that the average experimental steel strain value corresponding to the cover concrete crushing was 0.037 and was comparable to the existing steel strain limits ($\varepsilon_s \leq$ 0.03) at the operational performance objective specified by ODOT for new bridge design. The experimentally determined concrete compressive strain for the operational performance objective was 0.0054 whereas the ODOT specified concrete strain value for the design of new bridges was 0.005. It is important to mention that the experimental strain value was derived from the curvature rod instrumentation that account for the slip at the column-spread footing interface due to the strain penetration into the footing. It was further investigated and found that the average longitudinal concrete compressive strain measured without slip contribution was 0.0043. Rigid body rotation at the base of the footing-column interface was determined by integrating the strain over the rebar length embedded into the footing. Since the measured strain in the embedded rebar was below the yield-strain, a linear strain distribution along the length of the rebar was assumed.

The ODOT recommended concrete compressive-strain value of 0.002 for the operational performance objective was found to be conservative for existing bridges with inadequate lap splices. It was also found that the ODOT-recommended limiting-strain lacks the currently used performance-based design philosophy where a performance objective is usually defined with respect to both steel and concrete strain values. In addition, results from current experimental program shows that the steel strain value corresponding to the residual crack width exceeding 1.0 mm for the existing bridges was significantly lower than steel strain at cover concrete crushing. Hence, incorporating the steel strain value to define the operational performance objective could possibly ensure the long-term serviceability for the non-seismically detailed existing bridges.

Table 6.9: Comparison of Recommended Strain Limits for Different Performance Objectives

Performance Level	Experimental Data (Non-seismically Detailed Bridges)		Design of New Bridges		Evaluation of Existing Bridges	
	Steel Strain (ε_s)	Concrete Strain* (ε_c)	Steel Strain (ε_s)	Concrete Strain* (ε_c)	Concrete Strain* (ε_c) Non-seismic Hoops	
					Inadequate Lap Splice	Adequate Lap Splice
Operational	0.017	0.0054**	$\varepsilon_s \leq 2\varepsilon_{sh}$ (≈ 0.03)	$\varepsilon_{cc} = 0.005$	0.002	0.002
Life Safety	N/M	0.019**	$\varepsilon_s \leq \varepsilon^R_{su}$ (≈ 0.06)	$\varepsilon_{cc} = 0.9\ \varepsilon_{cu}$ (≈ 0.007)	0.003	0.004

*All the concrete strain reported are at the face of the column. Core concrete strain will thus be less than the reported values.
**Concrete strain data includes contribution of slip measurement at the base of the column.

The results from previous experimental investigations at Portland State University were considered along with the current experimental scheme to generate different data points for strain limit states and hence to generalize the performance objectives for typical bridge types in Oregon.

Despite the differences in test setup, loading condition and testing methods, geometry and reinforcing details are representative of existing bridges in Oregon. Hence, the component performance objectives and associated strain values reported in Sections 6.3.1 through 6.3.4 were incorporated in the current section. The strain values corresponding to particular performance objectives are tabulated in Table 6.10 to compare the variation for bridge columns with different detailing and/or loading conditions. It is difficult to generalize the strain limit states due to the wide array of variables used in different tests such as component detailing, boundary conditions, test setup, loading conditions etc. However, this will provide insight into the range of variation in strain limits for different experimental programs.

Table 6.10: Strain Limit State for "Operational" Performance Objective

Experimental Program	Steel Strain (ε_s)	Concrete Strain (ε_c)
RC Bent (1.5.2)	0.010	0.0042
Circular RC Column (1.5.3)	0.0117	0.0046
Square RC Column "#8" (1.5.4)	0.017	0.0054

The average steel strain for the operational performance objective as obtained from different experimental program was 0.0129 with a standard deviation of 0.003. On the other hand, the average concrete compressive strain for the past experimental investigation was 0.005 with a standard deviation of 0.0005.

6.4.2 Life Safety Performance Level

The life-safety limit-state aims to prevent complete collapse during an earthquake event. This performance state was defined by a complete loss of cover concrete, which led to the exposure of longitudinal rebar and buckling of the longitudinal/dowel bars. The life safety concrete compressive strain was defined as the point of complete concrete cover loss and the life safety steel strain value was defined as the peak tensile strain prior to the buckling of the rebar. The higher strain values associated with the specified damage levels were difficult to extract with conventional instrumentation. All strain gauges in the critical locations of the columns were lost well ahead of the higher damage cycles and hence no reliable steel strain data can been reported. On the other hand, computed concrete strain data from the curvature instrumentation showed higher strain values at the face of the column due to the inclusion of slip at the base of the column. Further investigation is thus recommended to define the strain values corresponding to the life-safety performance limit-state. Nevertheless, the results obtained from past experiments for circular concrete columns and RC bents with typical detailing for Oregon bridges are reported in Table 6.11.

Table 6.11: Strain Limit State for "Life Safety" Performance Objective

Experimental Program	Steel Strain (ε_s)	Concrete Strain (ε_c)
RC Bent (1.5.2)	0.048	0.0080
Circular RC Column (1.5.3)	0.0402	0.0099
Square RC Column "#8" (1.5.4)	N/M	0.019

The average steel strain corresponding to the life-safety limit-state is 0.0441 with a standard deviation of 0.0039. On the other hand, the average concrete compressive strain for the life safety is 0.012 and the standard deviation is 0.005.

6.5 SUMMARY

ODOT bridges are intended to meet two performance levels. This means that structural performance is described with two discrete performance levels and two associated seismic hazards. Results from experiments conducted as part of this research as well as previous research were incorporated to quantify various performance levels and associated material strain-limit values in order to initiate a discussion of these strain limits for bridge design or evaluation of existing bridges.

7.0 OVERALL SUMMARY AND CONCLUSION

7.1 CONCLUSIONS

The experimental program of this research consisted of three full-scale reinforced concrete bridge column-footing subassemblies representing non-seismically detailed substructure of concrete continuous stringer/girder bridges in Oregon. All specimens had the same material and reinforcing details. The specimens were tested under quasi-static reverse cyclic lateral loading and variable axial loading protocol. Lateral loading protocol consisted of long duration Cascadia Subduction zone protocol and three cycle symmetric laboratory loading protocol. Conclusions made from the test results of these specimens are as follows:

- The sequence of damage for the tested specimens were concrete cracking, yielding of longitudinal reinforcement, initiation of cover concrete spalling, exceedance of residual crack width beyond 1.0 mm, loss of cover concrete, and rebar buckling/fracture. However, specimen LVF#8 experienced a slightly different sequence of damage progression where initiation of spalling was observed earlier than the residual crack width exceedance of 1.0 mm. Lap splice failure was also evident for all specimens tested.

- Flexural cracks in the column were concentrated in the location of transverse reinforcement having a crack spacing similar to the spacing of the transverse rebar.

- Most of the damage was concentrated at the base of the column where a cold joint existed in the column-spread footing interface. No visible damage was observed in the lightly reinforced spread footing. Although, strain penetration into the foundation through dowel bars resulted in considerable slip of longitudinal reinforcement at the column-footing interface.

- Crack widths and residual crack widths recorded for specimen SVF#8 and LVF#8 were found to be significantly higher for pull cycles of loading than the push cycles where push cycles of loading were associated with higher axial loads. It was also found that the performance limit state, which has a residual crack width exceeding 1.0 mm, was taking place during the pull cycles of loading when lower axial load was applied. Hence, it can be concluded that the application of higher axial load will result in reduced crack widths and residual crack widths.

- The spread footing showed rocking behavior resulting from the uplifting under reverse cyclic lateral loading. It was also found that the specimens with greater uplifting resulted in achieving overall higher displacement ductility.

- In comparison with the behavior of previously tested columns at Portland State University, it can be concluded that the moderate splice length along with foundation rocking resulted in achieving higher displacement ductility for the column-footing

subassembly than the previously tested columns with lower splice length. It can also be concluded that specific damage states (i.e. concrete spalling, rebar buckling etc.) were delayed due to the rocking of the foundation as compared to the past test results that focused only in the column component behavior (i.e. footings were anchored to the floor).

- Despite having the substandard seismic detailing for pre-1990 bridge column-footing subassemblies, all tested specimens showed ductile behavior under reverse cyclic lateral loading. A minimum displacement ductility of $\mu = 8.0$ was achieved prior to failure.

- Higher strength degradation was observed for all three specimens during the loading cycles with higher axial load application (push cycles). It was evident from both experimental results and numerical analyses that the strength degradation depends on the level of axial load applied and increases with an increase in applied axial load. In addition, specimen LVF#8 was subjected to a symmetric three-cycle lateral loading protocol and experienced higher strength degradation compared to other two specimens.

- Stiffness degradation defined as the ratio of secant stiffness to effective yield stiffness was found to be minimally influenced by the variation of axial load and the type of lateral loading protocol used. All three specimens showed a smooth non-linear stiffness degradation pattern with a maximum variation of less than 20%.

- Constant axial loading resulted in a symmetric load-deformation response having almost the same peak lateral strength. The specimen tested under constant axial loading (SCF#8) achieved 46.0 kips and 42.4 kips peak lateral strength (7.5% lower) in the push and pull cycles of loading, respectively. In addition, the displacement ductility at which the peak lateral strength was achieved was within 4.5% variation in the push and pull cycles.

- Variation in axial load resulted in an unsymmetrical load-deformation response for specimen SVF#8, having a higher peak lateral strength corresponding to higher axial load. The peak lateral strength achieved with higher axial load cycle was 46.2 kips whereas the peak lateral strength corresponding to the lower axial load cycle was 39.6 kips (16.7% lower). On the contrary, higher damage and higher strength degradation was associated with higher axial load. The displacement ductility at which the peak lateral strength recorded was 3.07 for higher axial loading and 3.74 (21.8% higher) for lower axial loading cycles, respectively.

- Lower values of displacement ductility corresponding to different damage was found for the specimen tested under variable axial loading (SVF#8) in comparison with the specimen under constant axial loading (SCF#8). However, it should be mentioned that the bottom of the foundation for the latter specimen (SVF#8) was leveled using self-leveling grout, which resulted in reduced foundation uplifting compared to the first specimen (SCF#8).

- The specimen tested under the conventional laboratory loading (LVF#8) protocol achieved a lower peak lateral strength in the push cycles (10.1% lower) as compared to the specimen that were tested under the subduction zone lateral loading protocol. However, the peak lateral strength in the pull cycles of loading was comparable. Higher damage levels were observed with the specimen under conventional three cycle symmetric loading protocol.

- Strain values corresponding to different damage states were recorded for the specimens tested and the effect of axial and lateral load variation was scrutinized. The strain values corresponding to the lower damage levels (i.e. cracking and yielding) for different specimens were comparable. The average concrete and steel strain values for cracking were $\varepsilon_c = 0.0017$ (standard deviation = 0.00023) and $\varepsilon_s = 0.0015$ (standard deviation = 0.00028), respectively. Average concrete and steel strains for first yielding of the longitudinal rebar were $\varepsilon_c = 0.0026$ (standard deviation = 0.0003) and $\varepsilon_s = 0.0024$ (standard deviation = 0.00011), respectively.

- The operational performance limit state was defined with respect to the concrete strain at the initiation of cover concrete spalling and steel strain corresponding to the exceedance of a residual crack width exceeding 1.0 mm. The average concrete and steel strains corresponding to the operational performance limit state was $\varepsilon_c = 0.0072$ (standard deviation = 0.0013) and $\varepsilon_s = 0.023$ (standard deviation = 0.0063), respectively.

- The concrete and steel strain values for the operational limit state was higher for the specimen tested under the conventional lateral loading protocol. Hence, the strain-limit values for the operational performance level were found to be governed by the specimens tested under the subduction zone lateral loading protocol.

- The strain-limit state for the operational performance criteria, as obtained from the experimental results, were compared with the existing strain limit states specified by Oregon Department of Transportation (ODOT) for the evaluation of existing bridges. The ODOT recommended concrete strain value of 0.002 was found to be conservative, for bridge columns dominated by flexure with substandard seismic detailing.

7.2 RECOMMENDATIONS FOR FUTURE RESEARCH

This experimental program was designed to investigate the effect of axial and lateral load variation on the behavior of reinforced concrete bridge columns and the strain limit states for different damage levels. The following recommendations are proposed for further studies:

- Variation in column geometry and reinforcing details (i.e. aspect ratio, transverse reinforcement, volumetric ratio, spacing of transverse reinforcement, splice length, etc.) should be considered to investigate the strain limit values across a more generalized set of bridge columns.

- The effect of soil-structure interaction on the different damage states should be investigated.

- Residual crack width was considered in this experimental program as a limit state and was found to be controlling the operational performance criteria. Cold joint at the column foundation region resulted in residual concrete crack width that exceeds the prescribed limit for long-term durability of the bridge structures. Hence, a revision in the qualitative definition of the operational performance criteria should be considered and further investigation should focus on quantifying the strain values corresponding to the residual crack-width limit-state.

- Conventional instrumentation limits the evaluation of strain values for different damage states. Advanced measurement approaches (i.e. three dimensional position sensors) could be used to capture the strain values more accurately, especially for higher damage levels.

- Limited confidence exists in the strain values for the life-safety performance criteria due to the difficulties in capturing strain data at higher displacement levels. Further studies could be used to investigate the material strain values at life-safety performance criteria for existing bridge types in the state of Oregon.

8.0 REFERENCES

American Association of State Highway Transportation Officials (AASHTO). (2011). *Guide Specifications for LRFD Seismic Bridge Design* (Publication No. LRFDSEIS-2). Washington, D.C.: American Association of State Highway Transportation Officials. Retrieved from https://store.transportation.org/Common/Download ContentFiles?id=1037.

American Association of State Highway Transportation Officials (AASHTO). 2017. *LRFD Bridge Design Specifications* (Publication No. LRFD-8). Washington, DC: American Association of State Highway and Transportation Officials.

American Concrete Institute. (2004). *Guide to formwork for concrete* (347-04). Detroit: American Concrete Institute.

ASTM International. 2007. *Standard Specification for Steel Wire, Deformed, for Concrete Reinforcement* (Standard No. A496/A496M-07). West Conshohocken, PA.

ASTM International. 2018. *Standard Specification for Carbon-Steel Wire and Welded Wire Reinforcement, Plain and Deformed, for Concrete* (Standard No. A1064/A1064M-18a). West Conshohocken, PA.

ASTM International. 2018. *Standard Specification for Deformed and Plain Carbon-Steel Bars for Concrete Reinforcement* (Standard No. A615/A615M-18). West Conshohocken, PA.

ASTM International. 2019. *Standard Test Methods and Definitions for Mechanical Testing of Steel Products* (Standard No. A370-19). West Conshohocken, PA.

ASTM International. 2019a. *Standard Test Methods and Definitions for Mechanical Testing of Steel Products* (Standard No. A370-19e1). West Conshohocken, PA.

ASTM International. 2020. *Standard Test Method for Compressive Strength of Cylindrical Concrete Specimens* (Standard No. C39/C39-20). West Conshohocken, PA.

Bazaez, R., & Dusicka, P. (2014). Development of Cyclic Loading Protocol for Bridge Columns Considering Subduction Zone Mega Earthquakes. In *Tenth U.S. National Conference on Earthquake Engineering*. Anchorage, AK: Frontiers of Earthquake Engineering. doi:10.4231/D3M61BQ54

Bentz, Evan C., and Michael P. Collins. 1998. *RESPONSE 2000, Reinforced Concrete Sectional Analysis using the modified compression field theory.*

Canadian Standards Association Group. 2014. *Canadian Highway Bridge Design Code* (Standard No. S6-14). Ontario, Canada. Retrieved from https://www.techstreet.com/mss/products/preview/1892344

Dusicka, P., & Lopez, A. (2016). *Impact of Cascadia Subduction Zone Earthquake on the Seismic Evaluation Criteria of Bridges* (Publication No. FHWA-OR-RD-17-04). Salem, OR: Oregon Department of Transportation.

Dusicka, P., Bazaez, R., & Knoles, S. (2015). *Bridge Seismic Retrofit Measures Considering Subduction Zone Earthquakes* (Publication No. FHWA-OR-RD-16-01). Salem, OR: Oregon Department of Transportation.

Federal Highway Administration. (1995). *Recording and Coding Guide for Structure Inventory and Appraisal of the Nation's Bridges.* (Publication No. FHWA-PD-96-001). Washington, D.C.: US Department of Transportation Federal Highway Administration.

Federal Highway Administration. (2006). *Sesimic Retrofitting Manual for Highway Structures: Part 1-Bridges* (Publication No. FHWA-HRT-06-032). McLean, VA: US Department of Transportation Federal Highway Administration.

Feng, Y., Kowalsky, M. J., & Nau, J. M. (2014). Effect of Seismic Load History on Deformation Limit States for Longitudinal Bar Buckling in RC Circular Columns. *Journal of Structural Engineering, 141*(8). doi:10.1061/(asce)st.1943-541x.0001153.

Feng, Y., Kowalsky, M. J., & Nau, J. M. (2014). Finite-Element Method to Predict Reinforcing Bar Buckling in RC Structures. *Journal of Structural Engineering, 141*(5). doi:10.1061/(asce)st.1943-541x.0001048.

Gallardo, R. A. (2017). *Achieving Operational Seismic Performance of RC Bridge Bents Retrofitted With Buckling-Restrained Braces* (Master's thesis, Portland State University, 2017). Portland: PDX Scholar.

Goodnight, J. C., Kowalsky, M. J., & Nau, J. M. (2013). Effect of Load History on Performance Limit States of Circular Bridge Columns. *Journal of Bridge Engineering, 18*(12), 1383-1396. doi:10.1061/(asce)be.1943-5592.0000495

Goodnight, J. C., Kowalsky, M. J., & Nau, J. M. (2016). Strain Limit States for Circular RC Bridge Columns. *Earthquake Spectra, 32*(3), 1627-1652. doi:10.1193/030315eqs036m

Gulkan, P., & Sozen, M. (1974). Inelastic Responses of Reinforced Concrete Structure to Earthquake Motions. *ACI Journal Proceedings, 71*(12), 604-610. doi:10.14359/7110

Hose, Y., Silva, P., & Seible, F. (2000). Development of a Performance Evaluation Database for Concrete Bridge Components and Systems under Simulated Seismic Loads. *Earthquake Spectra, 16*(2), 413-442. doi:10.1193/1.1586119

Jean, M., St-Martin, C., Roy, N., Rivard, P., Moradian, O., Carvalho, E., & Proulx, J. (2012). Limit states of reinforced concrete bridge piers confined with carbon fiber reinforced

polymer (CFRP). In *15th World Conference on Earthquake Engineering 2012 (15WCEE): Lisbon Portugal, 24-28 September 2012*. Lisboa, Portugal: SPES.

Kowalsky, M. J. (2000). Deformation Limit States for Circular Reinforced Concrete Bridge Columns. *Journal of Structural Engineering, 126*(8), 869-878. doi:10.1061/(asce)0733-9445(2000)126:8(869)

Lehman, D., Moehle, J., Mahin, S., Calderone, A., & Henry, L. (2004). Experimental Evaluation of the Seismic Performance of Reinforced Concrete Bridge Columns. *Journal of Structural Engineering, 130*(6), 869-879. doi:10.1061/(ASCE)0733-9445(2004)130:6(869)

Mehary, S., & Dusicka, P. (2015). *Seismic Retrofit Benefit Considering Statewide Transportation Assessment* (Publication No. OR-RD-15-15). Salem, OR: Oregon Department of Transportation.

Moehle, J., & Deierlein, G. (2004). A framework methodology for performance-based earthquake engineering. In *13th World conference on earthquake engineering: Conference proceedings*. Vancouver, B.C., Canada: Earthquake Engineering Conference Secretariat Canada.

Moyer, M., & Kowalsky, M. (2003). Influence of Tension Strain on Buckling of Reinforcement in Concrete Columns. *ACI Structural Journal, 100*(1), 75-85. doi:10.14359/12441

National Cooperative Highway Research Program. (2013). *Performance-Based Seismic Bridge Design, Synthesis 440.* Washington, D.C.: Transportation Research Board, National Academy of Sciences. doi: 10.17226/22632

Oregon Department of Transportation. (2019). *Bridge design and drafting manual.* Salem, Oregon: Oregon Department of Transportation (ODOT).

Priestley, M. (2000). *Performance based seismic design* (Publication No. 2831). San Diego, CA: University of California. Retrieved from https://pdfs.semanticscholar.org/11d3/f204413074dbd98923281561e4cf0e0a06fa.pdf.

Seismology Committee Structural Engineers Association of California. (1996). *Recommended lateral force requirements and commentary*. Sacramento, CA: Structural engineers Association of California.

Sheikh, M., Legeron, F., & Tsang, H. (2012). *Seismic performance of bridges designed according to AS 5100* (Rep.). Wollongong, Australia: University of Wollongong.

Vecchio, F., & Collins, M. (1986). The Modified Compression-Field Theory for Reinforced Concrete Elements Subjected to Shear. *ACI Journal Proceedings, 83*(2), 219-231. doi:10.14359/10416

APPENDIX A

(a)

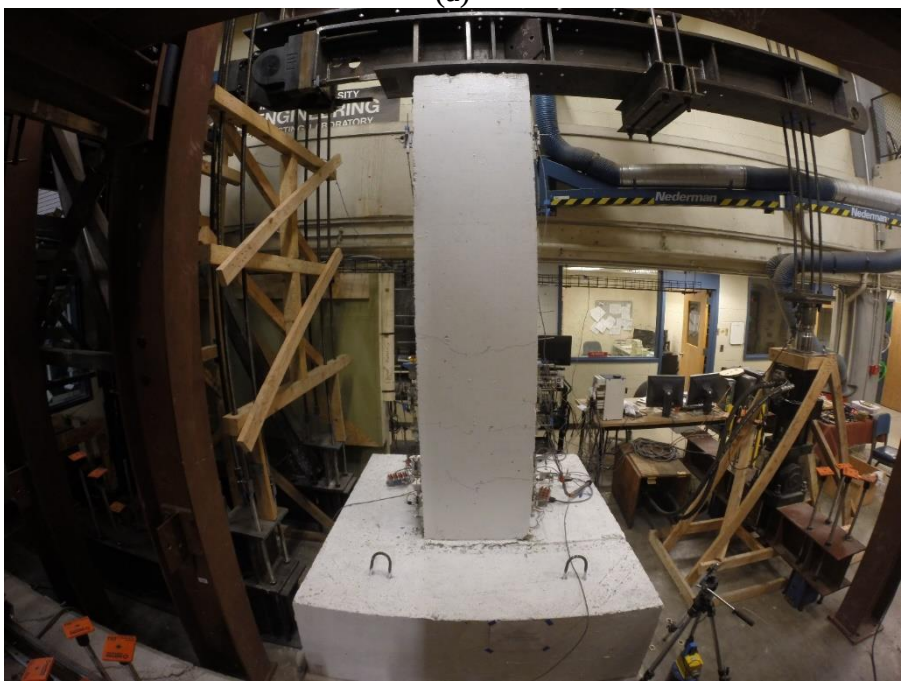

(b)

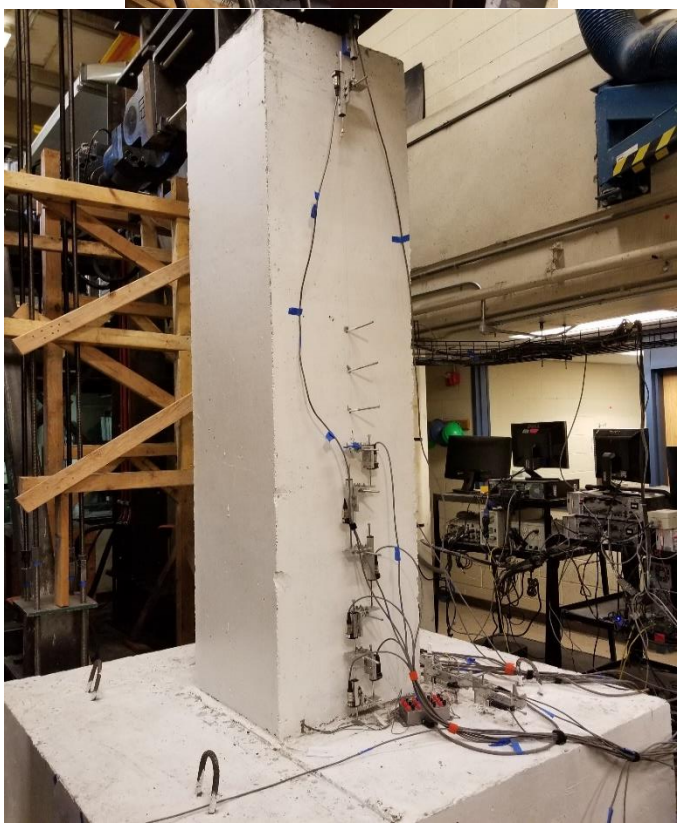

(c)

Figure A-1: Test setup (a) Top view, (b) East face view and (c) Column external instrumentation

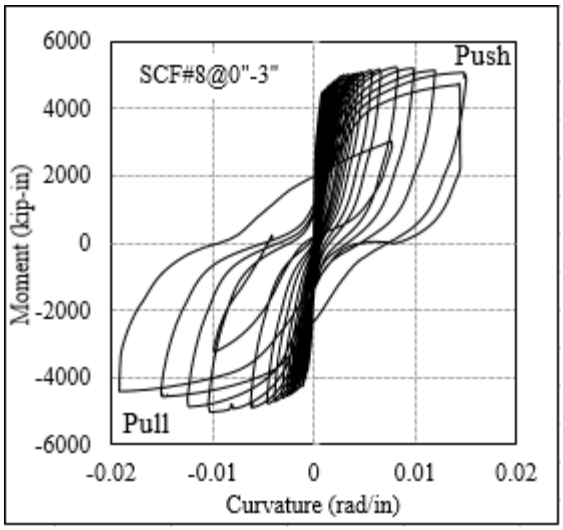

(a) with slip*

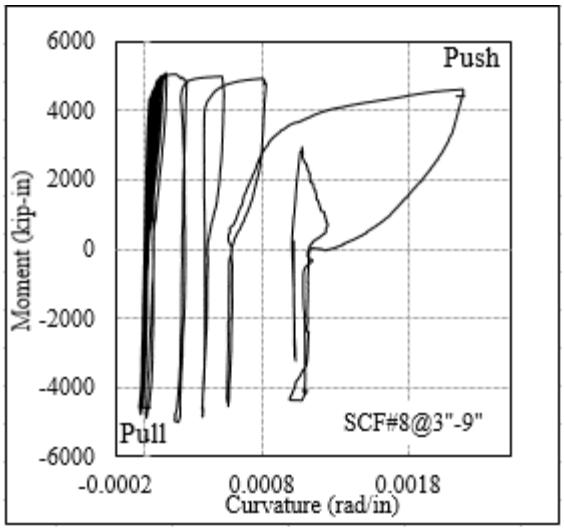

(b)

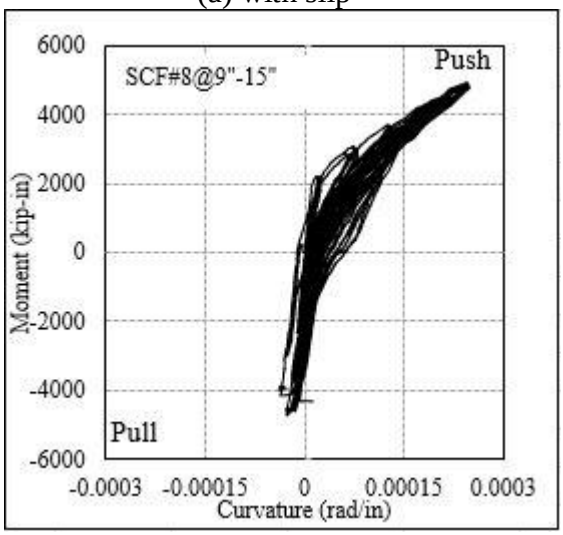

(c)

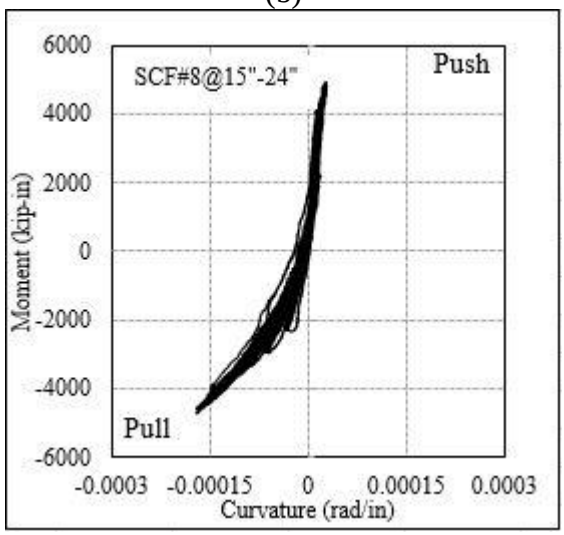

(d)

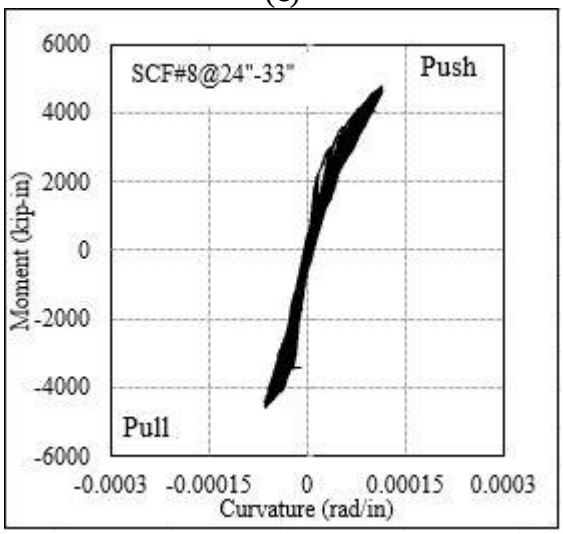

(e)

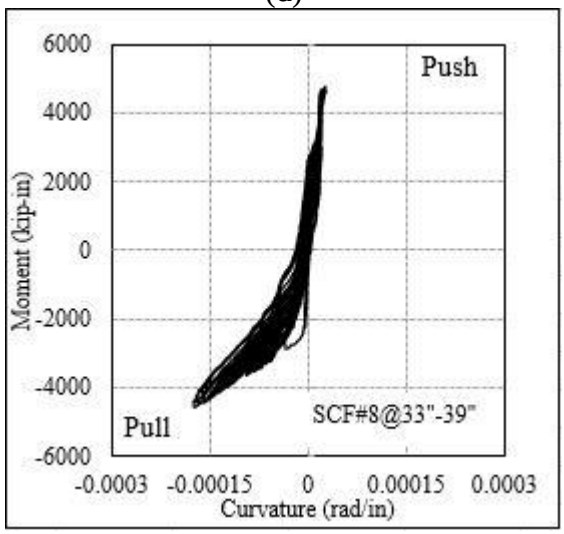

(f)

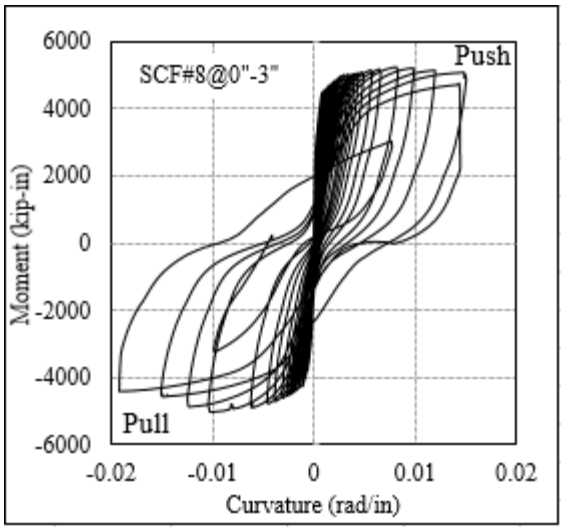

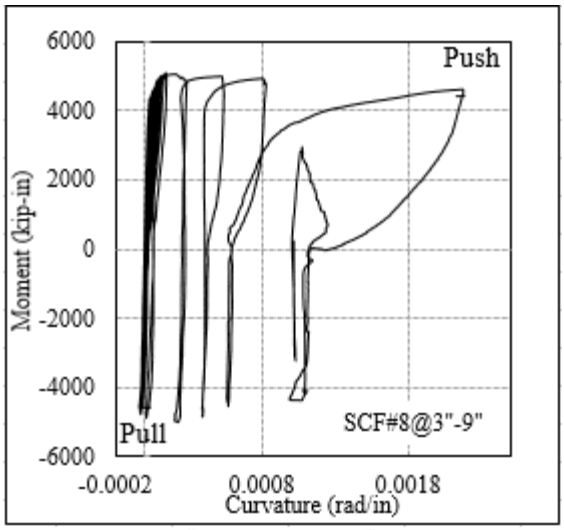

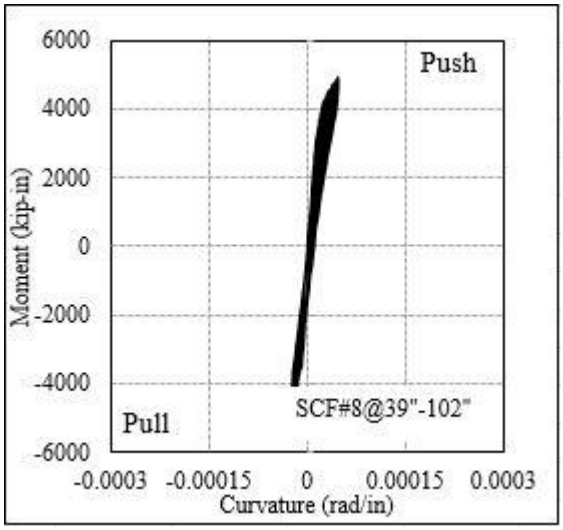

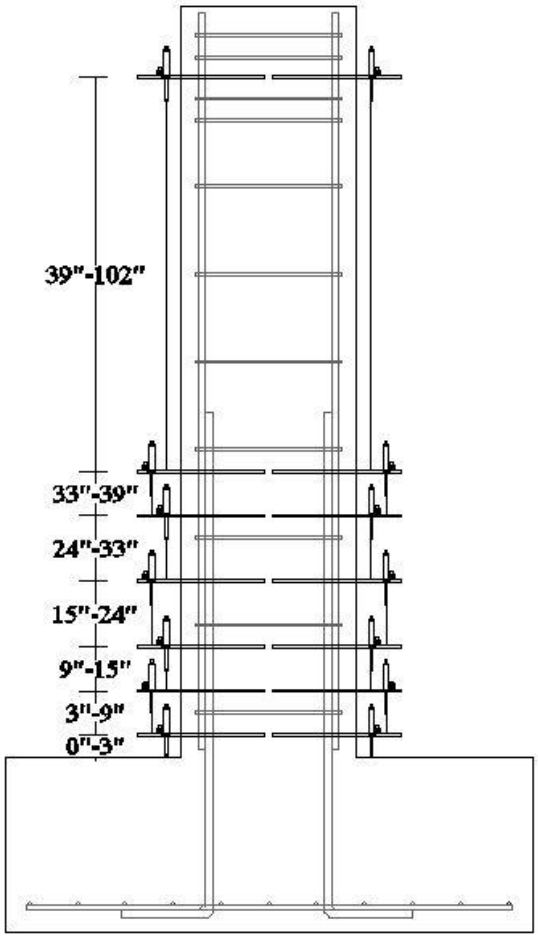

(g) (h)

Figure A-2: Moment-Curvature response for specimen SCF#8 (a) 0"-3" segment, (b) 3"-9" segment, (c) 9"-15" segment, (d) 15"-24" segment, (e) 24"-33" segment, (f) 33"-39" segment, (g) 39"-102" (Top) segment and (h) Measured segment.

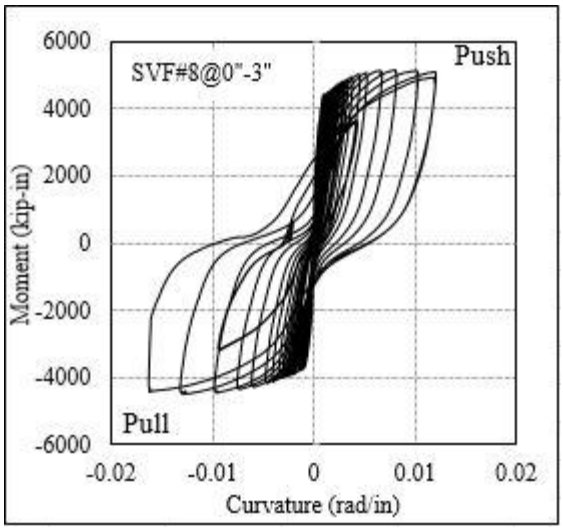

(a) with slip*

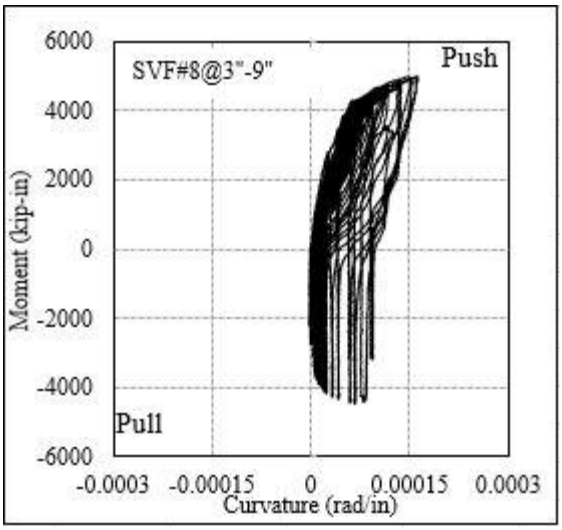

(b)

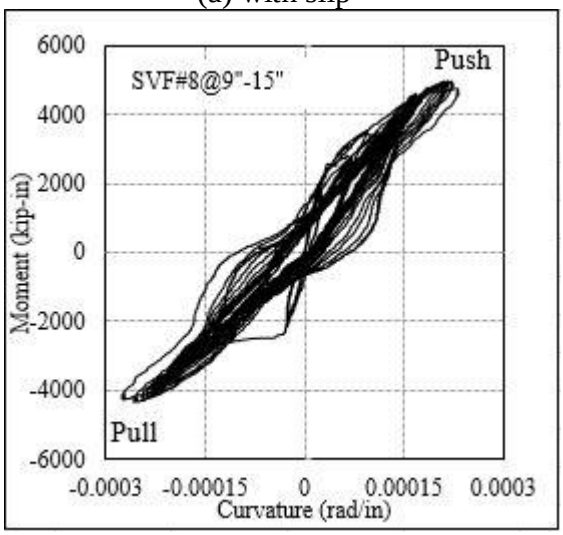

(c)

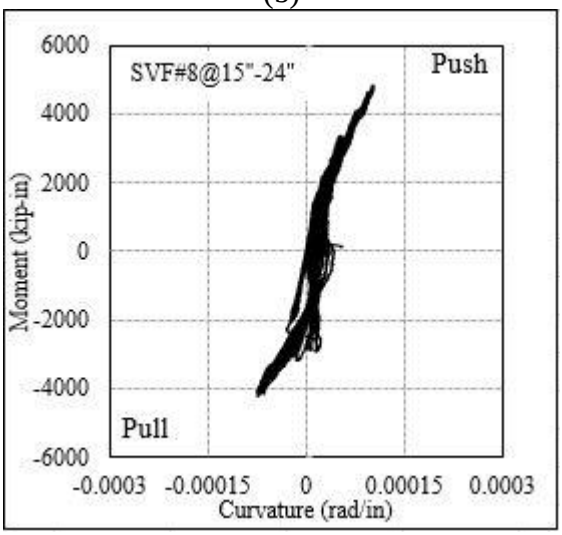

(d)

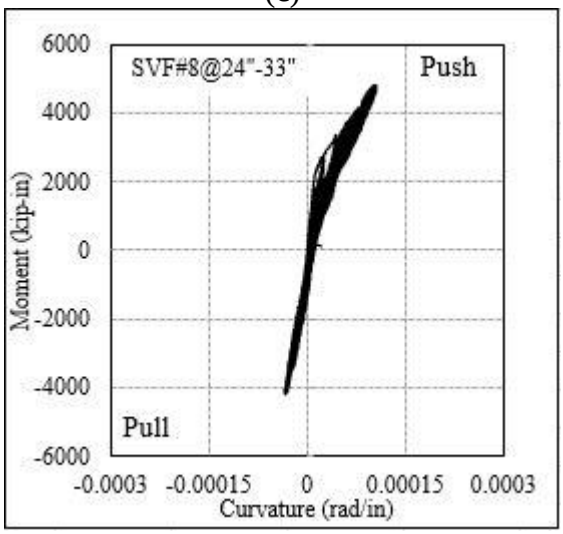

(e)

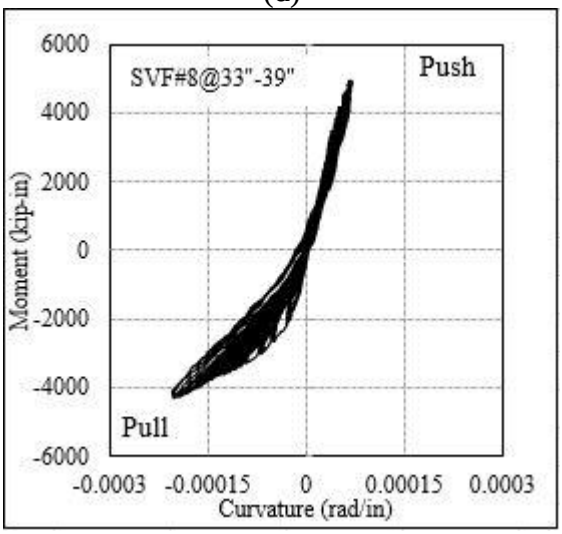

(f)

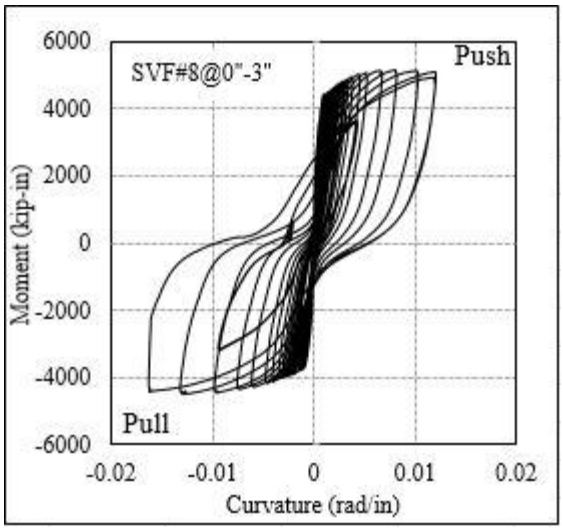

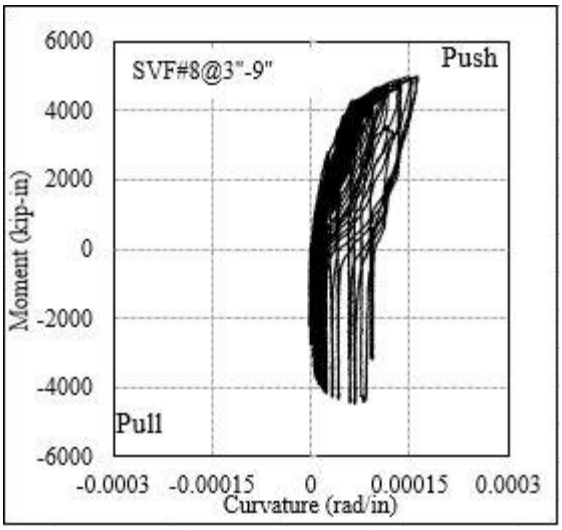

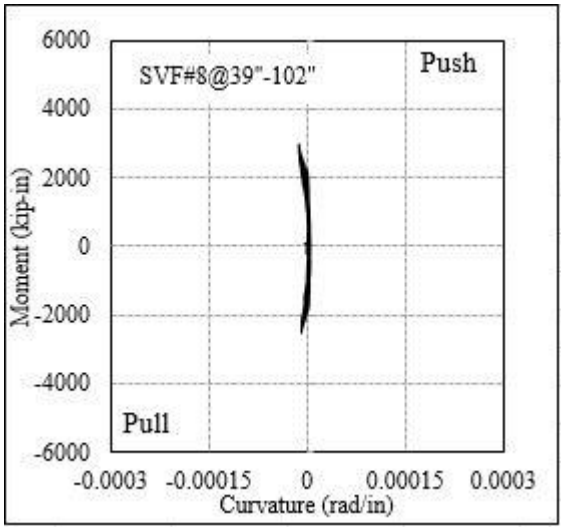

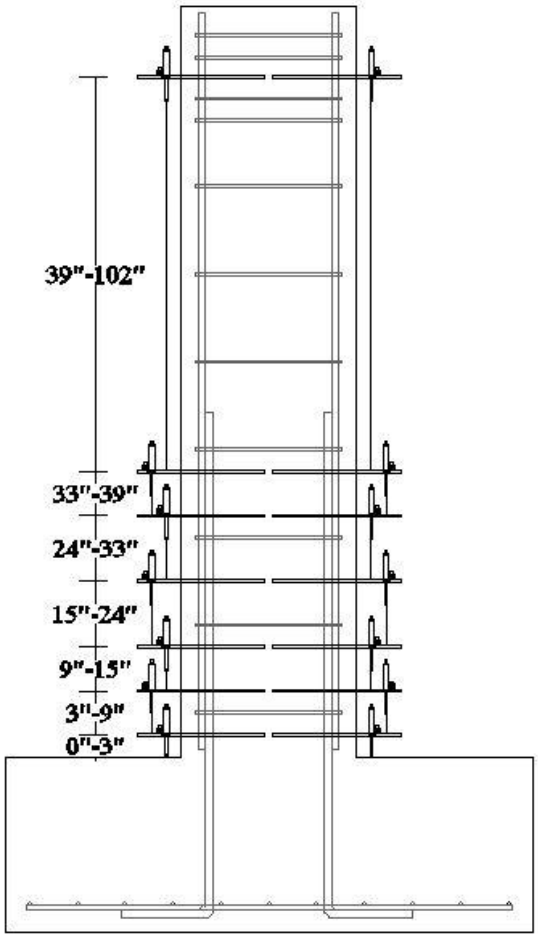

(g) (h)

Figure A-3: Moment-Curvature response for specimen SVF#8 (a) 0"-3" segment, (b) 3"-9" segment, (c) 9"-15" segment, (d) 15"-24" segment, (e) 24"-33" segment, (f) 33"-39" segment and (g) 39"-102" (Top) segment and (h) Measured segment.

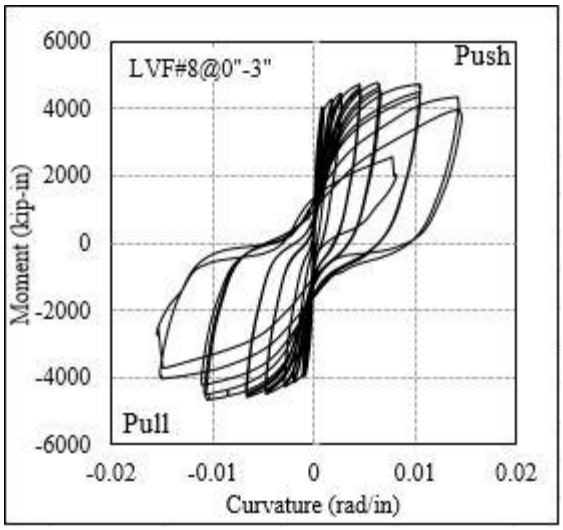

(a) with slip*

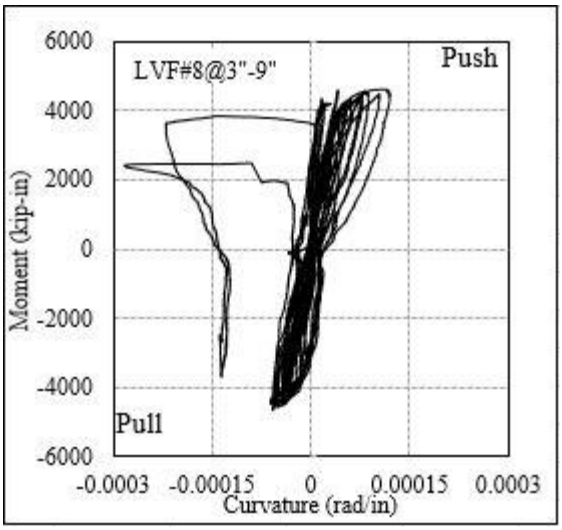

(b)

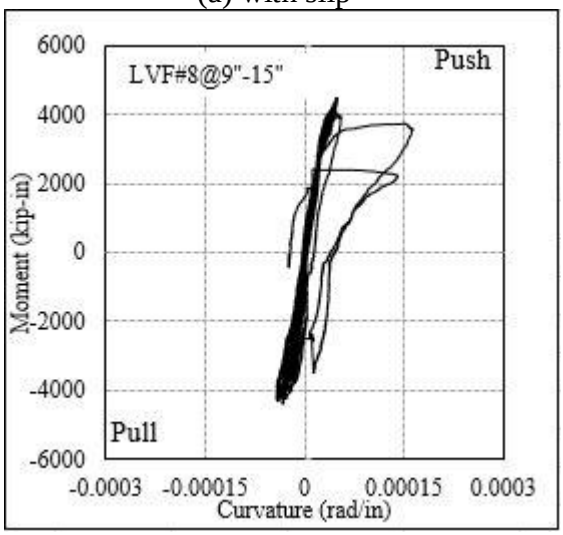

(c)

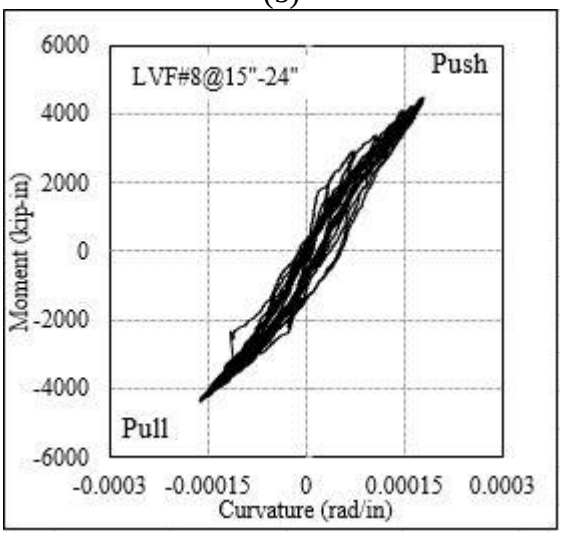

(d)

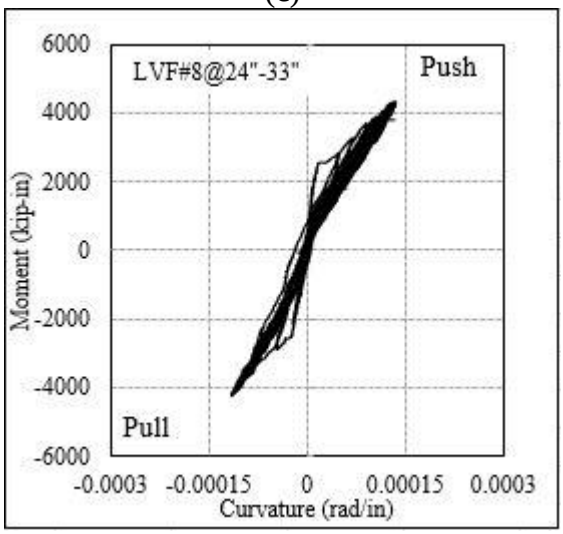

(e)

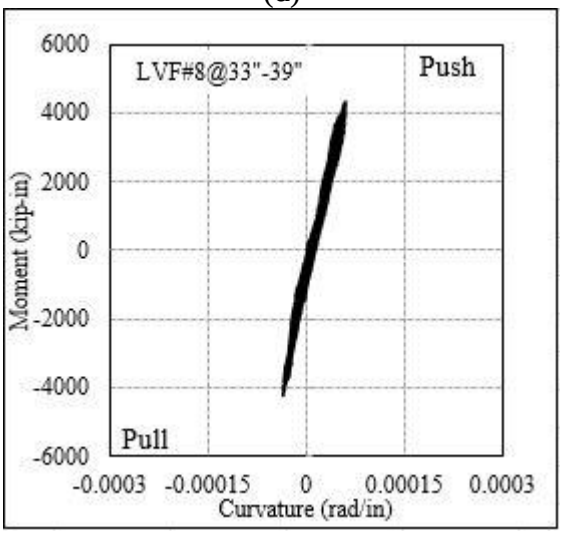

(f)

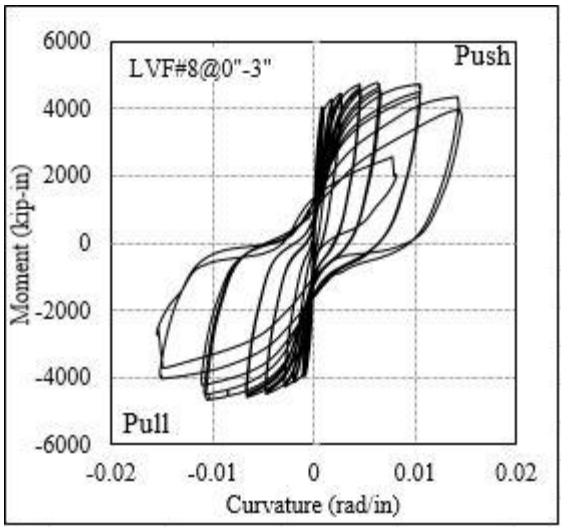

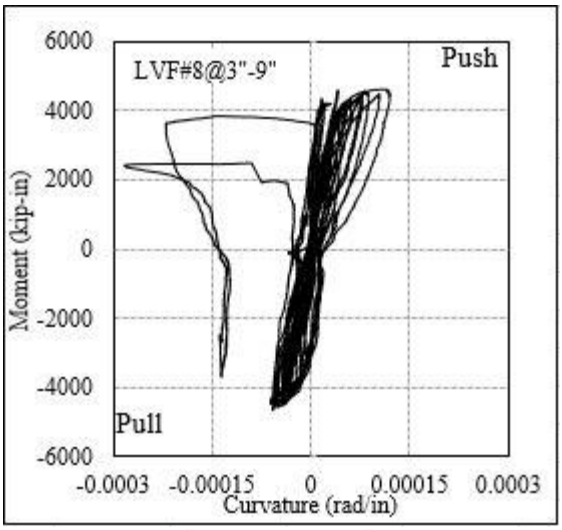

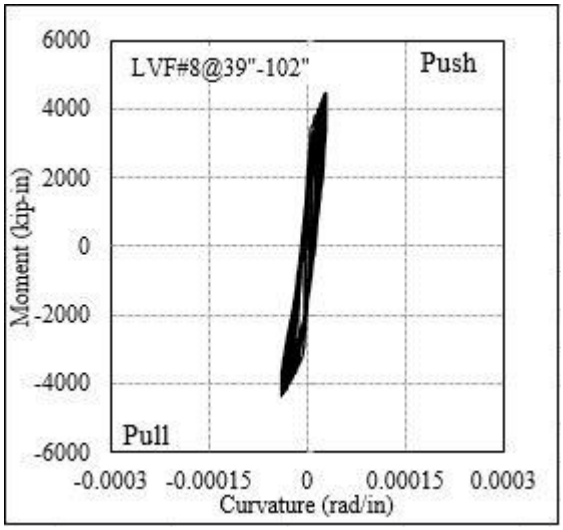

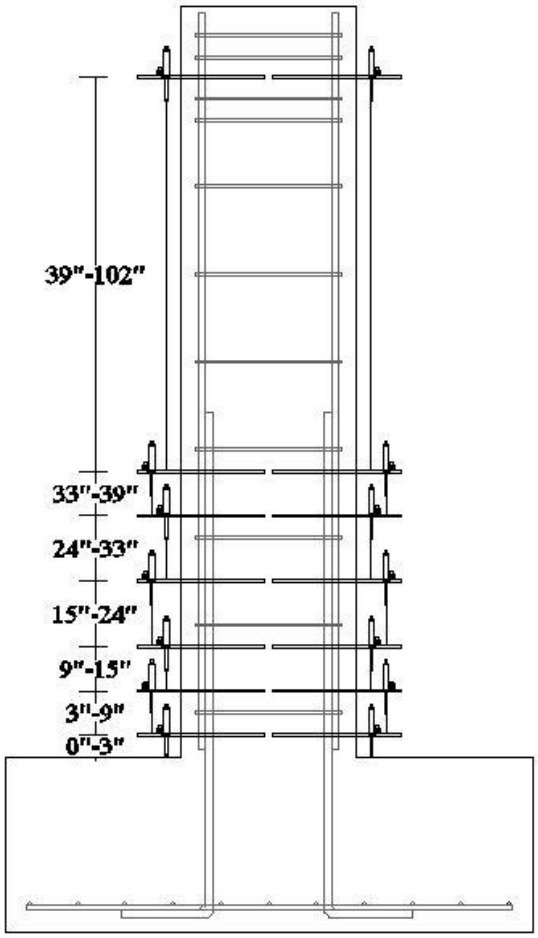

(g) (h)

Figure A-4: Moment-Curvature response for specimen LVF#8 (a) 0"-3" segment, (b) 3"-9" segment, (c) 9"-15" segment, (d) 15"-24" segment, (e) 24"-33" segment, (f) 33"-39" segment and (g) 39"-102" (Top) segment and (h) Measured segment.

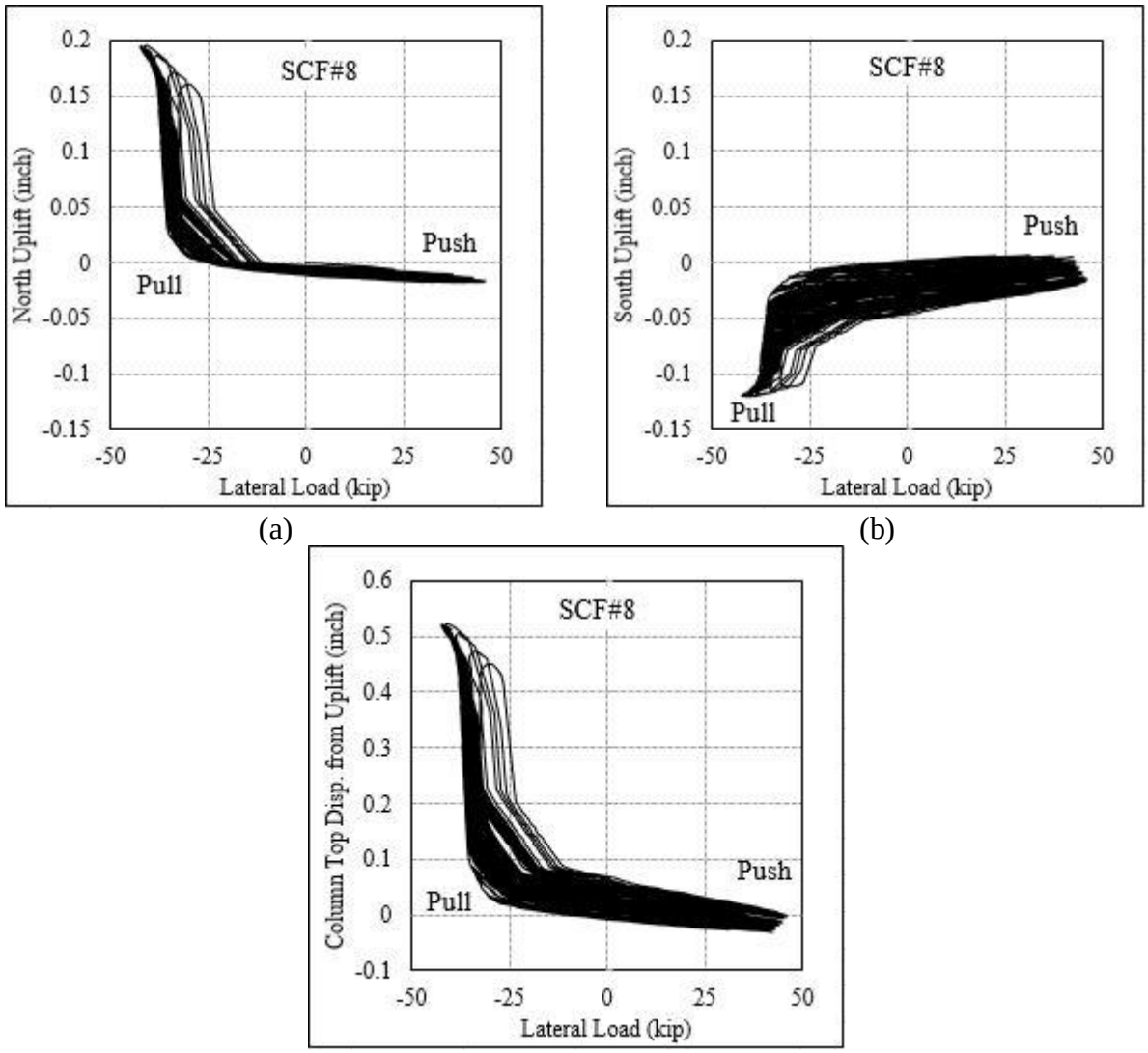

Figure A-5: System deformation for SCF#8 (a) Uplift measured at the north face of foundation, (b) Uplift measured at the south face of the foundation and (c) Column top displacement due to foundation uplift (Rigid body approximation).

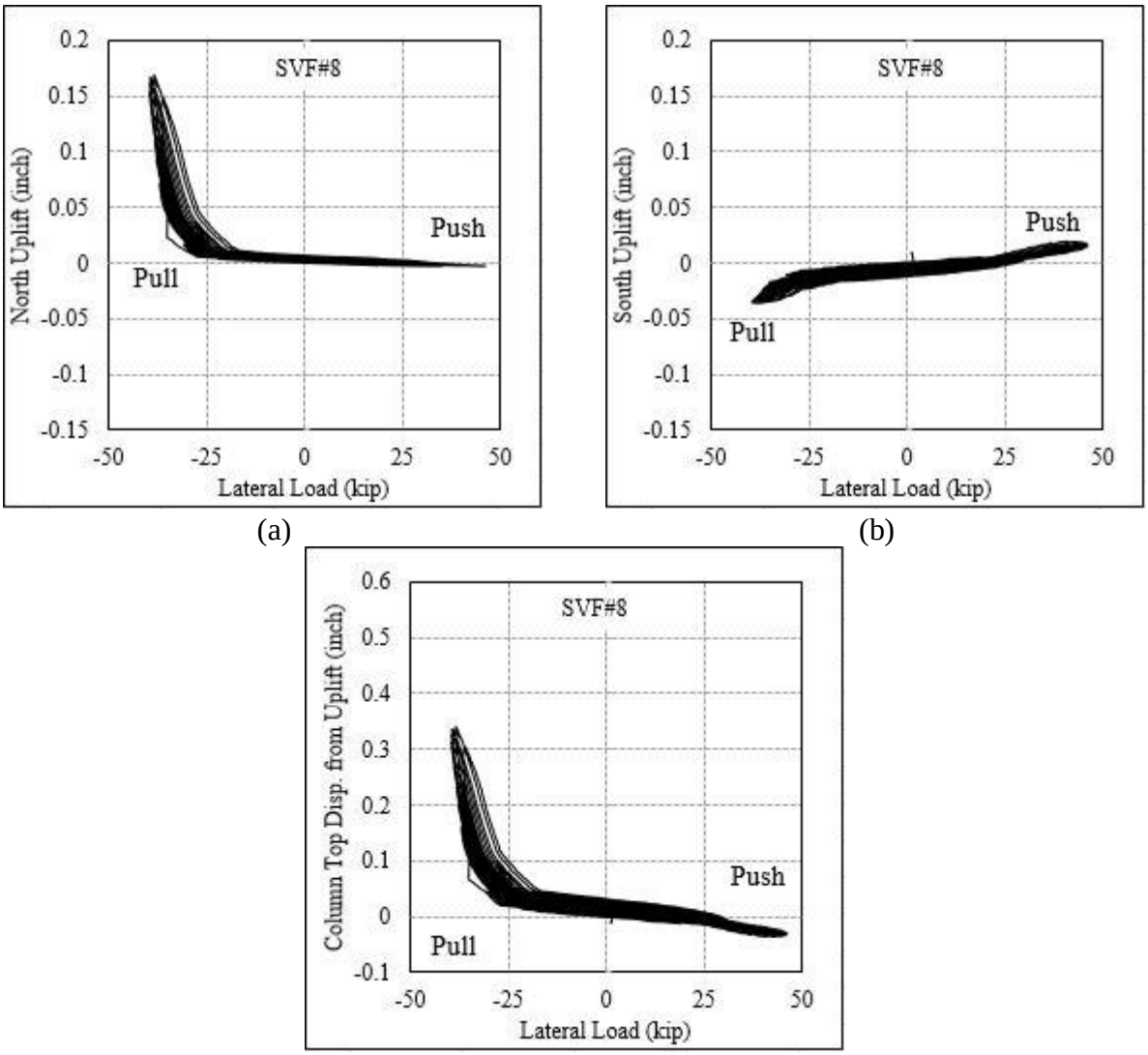

Figure A-6: System deformation for SVF#8 (a) Uplift measured at the north face of foundation, (b) Uplift measured at the south face of the foundation and (c) Column top displacement due to foundation uplift (Rigid body approximation).

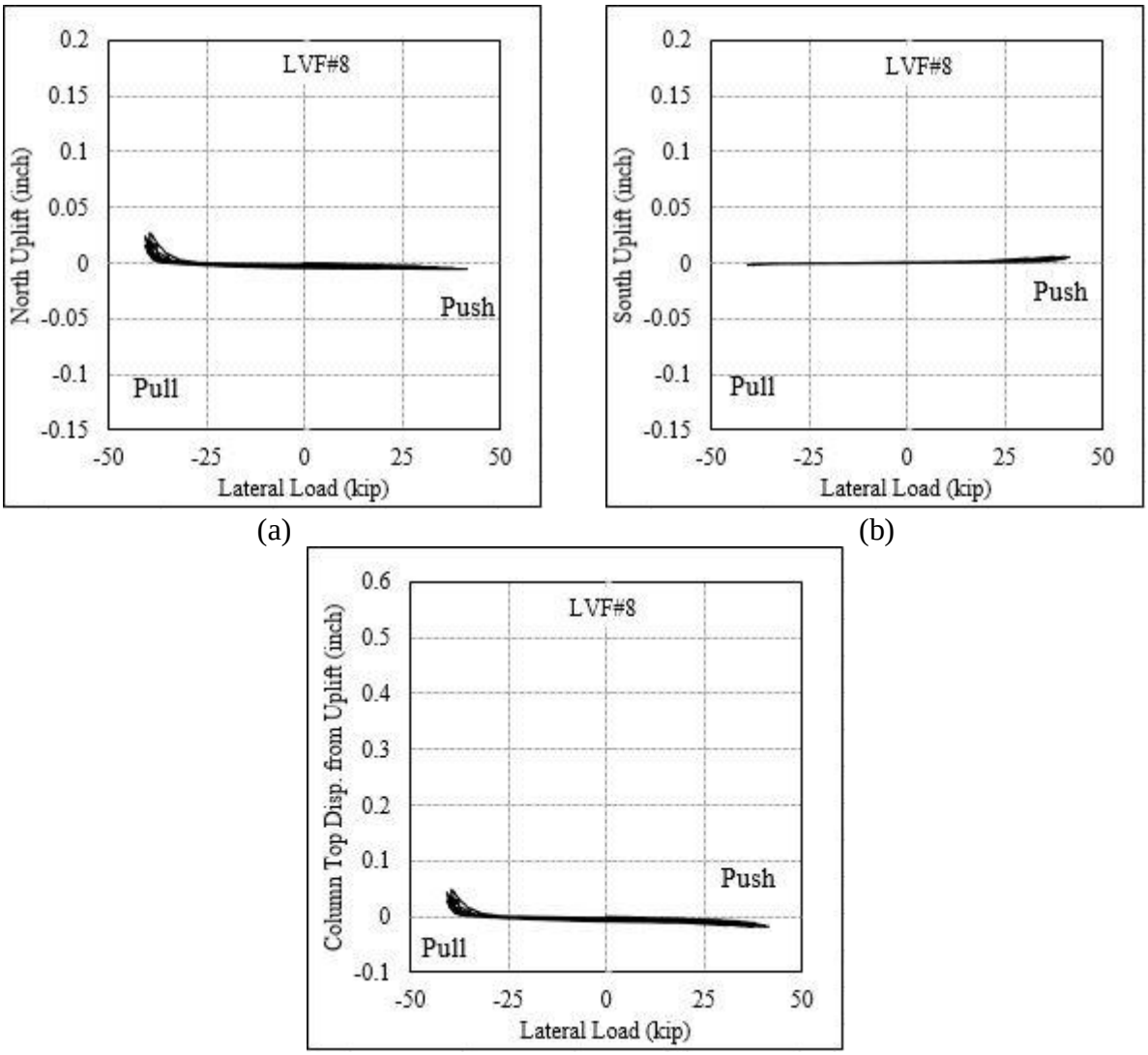

Figure A-7: System deformation for LVF#8 (a) Uplift measured at the north face of foundation, (b) Uplift measured at the south face of the foundation and (c) Column top displacement due to foundation uplift (Rigid body approximation).

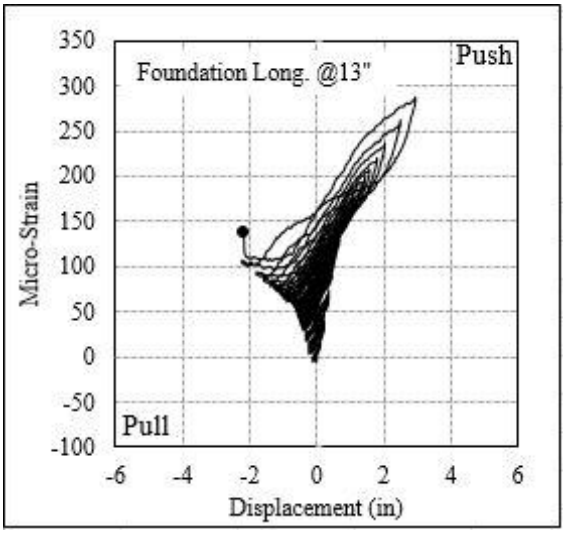
Foundation Long. @13"
Push
Pull
Micro-Strain
Displacement (in)
350
300
250
200
150
100
50
0
-50
-100
-6
-4
-2
0
2
4
6

(a)

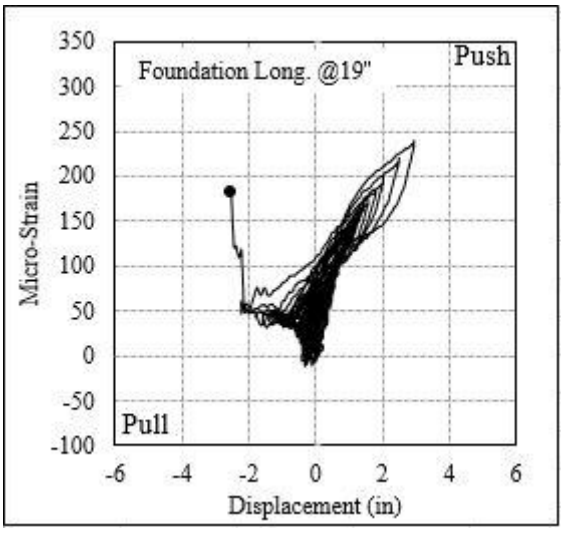
Foundation Long. @19"
Push
Pull
Micro-Strain
Displacement (in)
350
300
250
200
150
100
50
0
-50
-100
-6
-4
-2
0
2
4
6

(b)

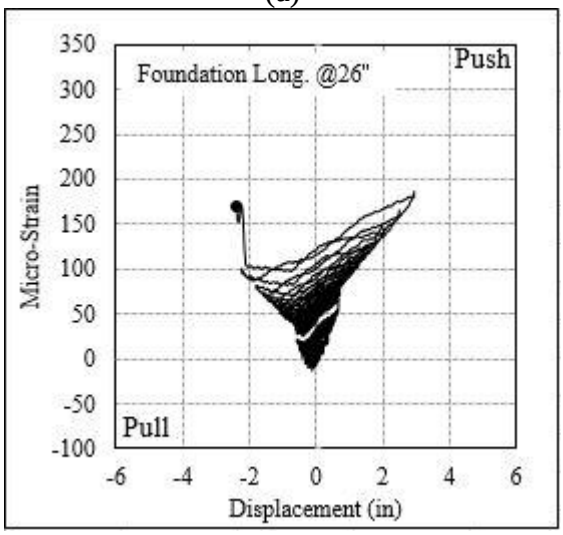
Foundation Long. @26"
Push
Pull
Micro-Strain
Displacement (in)
350
300
250
200
150
100
50
0
-50
-100
-6
-4
-2
0
2
4
6

(c)

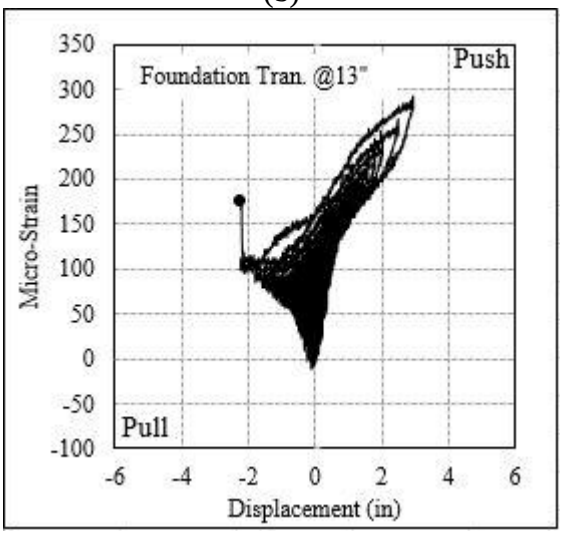
Foundation Tran. @13"
Push
Pull
Micro-Strain
Displacement (in)
350
300
250
200
150
100
50
0
-50
-100
-6
-4
-2
0
2
4
6

(d)

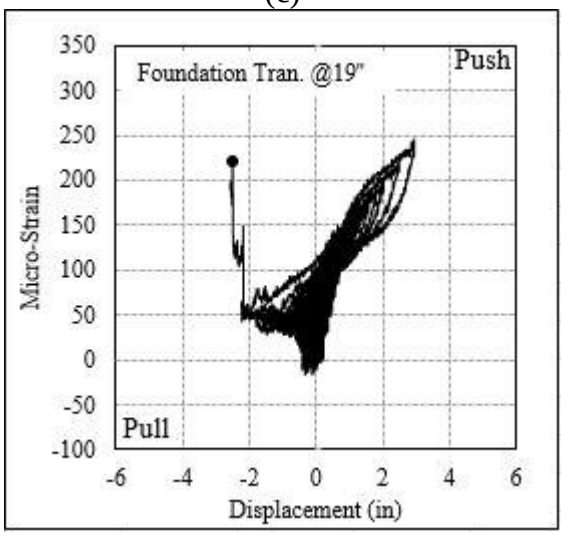
Foundation Tran. @19"
Push
Pull
Micro-Strain
Displacement (in)
350
300
250
200
150
100
50
0
-50
-100
-6
-4
-2
0
2
4
6

(e)

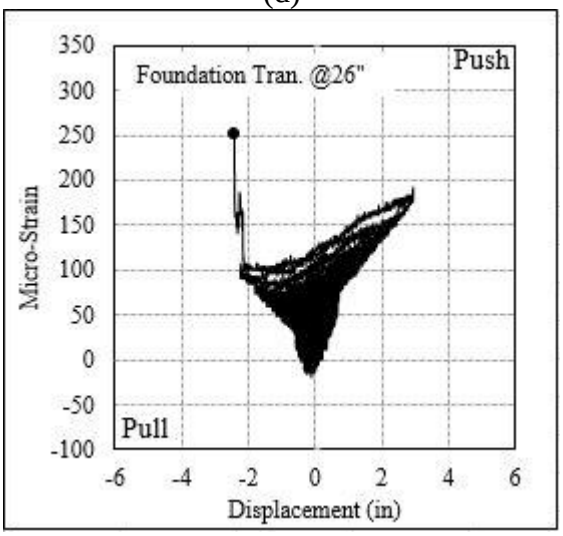
Foundation Tran. @26"
Push
Pull
Micro-Strain
Displacement (in)
350
300
250
200
150
100
50
0
-50
-100
-6
-4
-2
0
2
4
6

(f)

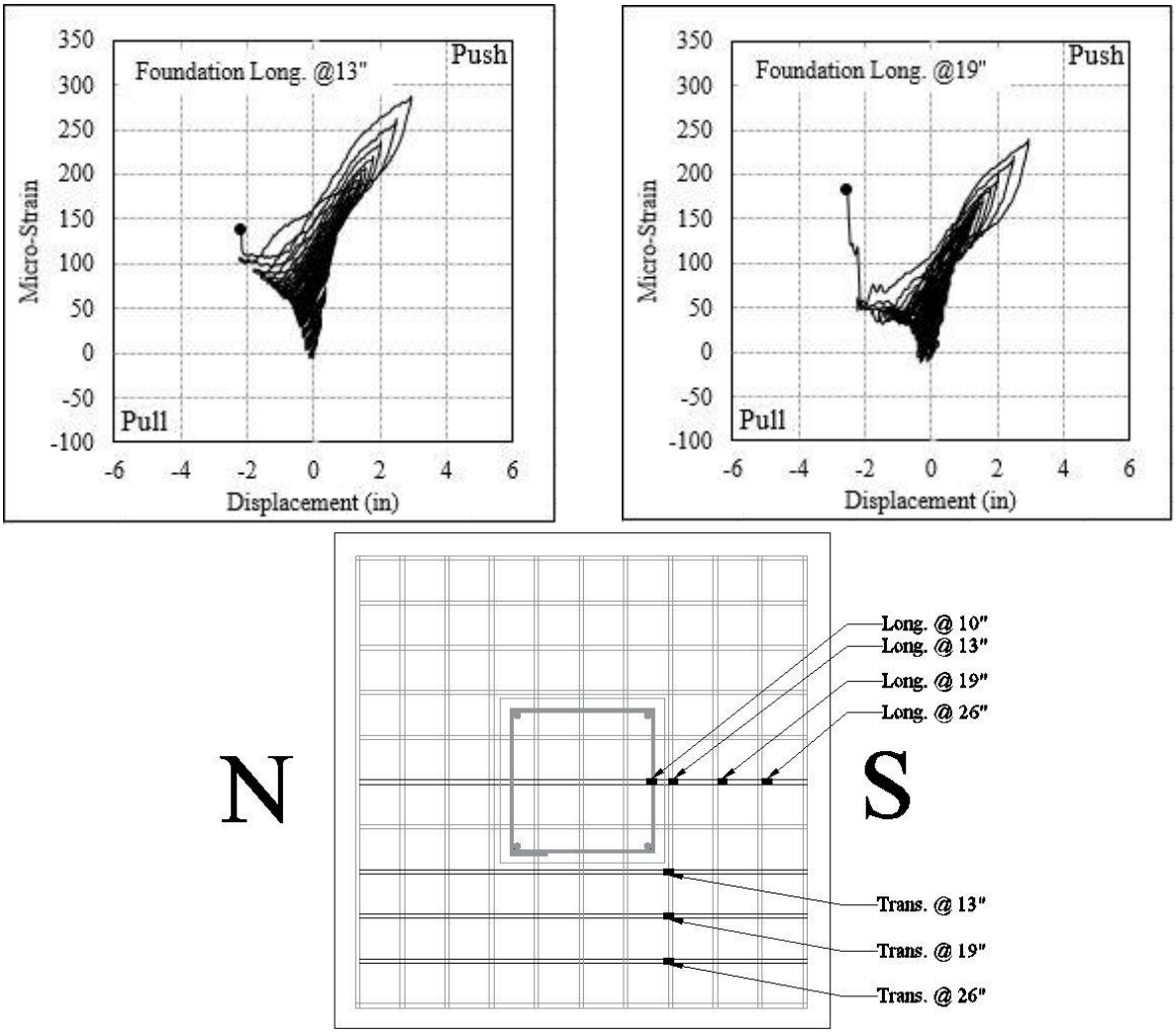

(g)

Figure A-8: Foundation Rebar strain hysteresis for specimen SVF#8 (a) Longitudinal rebar @ 13" from column center, (b) Longitudinal rebar @ 19" from column center, (c) Longitudinal rebar @ 26" from column center, (d) Transverse rebar @ 13" from column center, (e) Transverse rebar @ 19" from column center, (f) Transverse rebar @ 13" from column center and (g) Instrumentation designation.

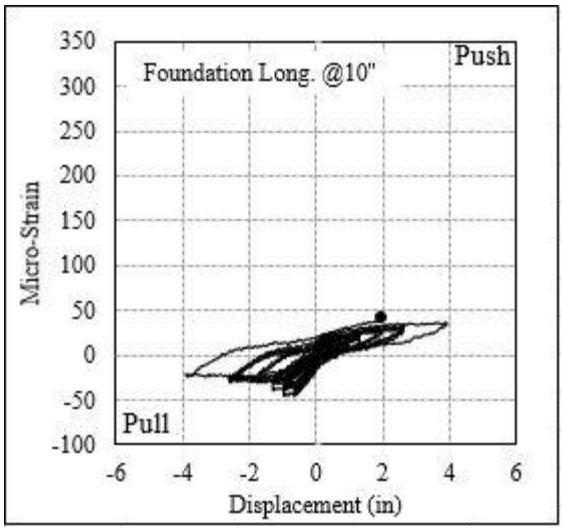
Foundation Long. @10"
Push
Pull
Micro-Strain
Displacement (in)
350
300
250
200
150
100
50
0
-50
-100
-6
-4
-2
0
2
4
6

(a)

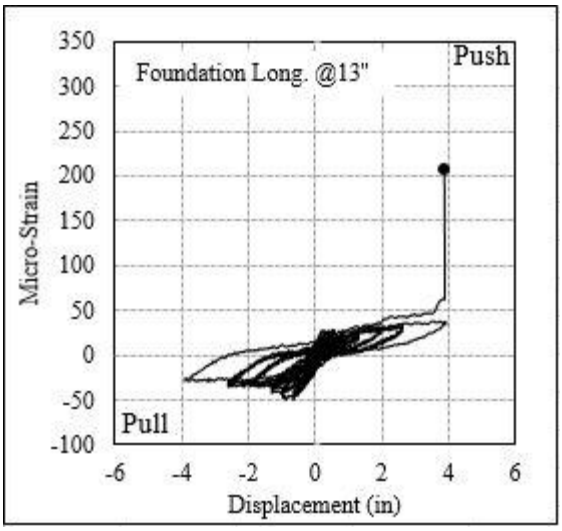
Foundation Long. @13"
Push
Pull
Micro-Strain
Displacement (in)
350
300
250
200
150
100
50
0
-50
-100
-6
-4
-2
0
2
4
6

(b)

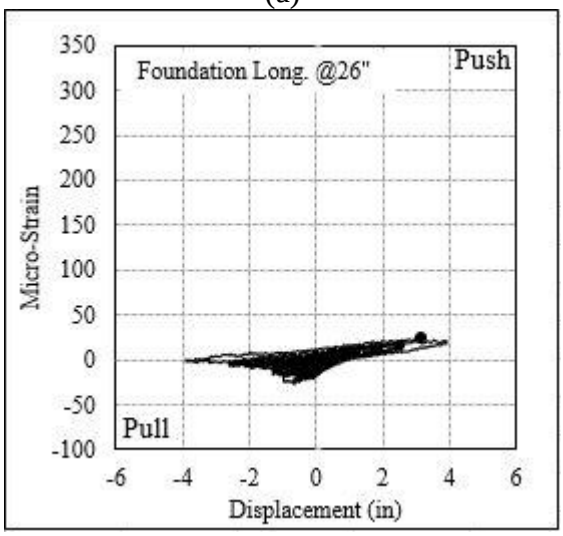
Foundation Long. @26"
Push
Pull
Micro-Strain
Displacement (in)
350
300
250
200
150
100
50
0
-50
-100
-6
-4
-2
0
2
4
6

(c)

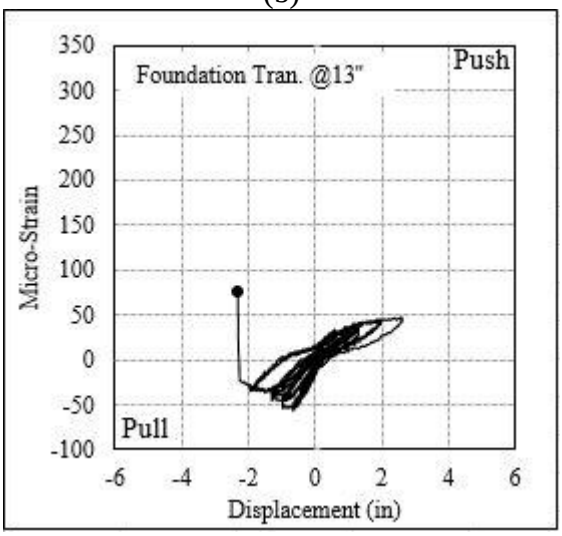
Foundation Tran. @13"
Push
Pull
Micro-Strain
Displacement (in)
350
300
250
200
150
100
50
0
-50
-100
-6
-4
-2
0
2
4
6

(d)

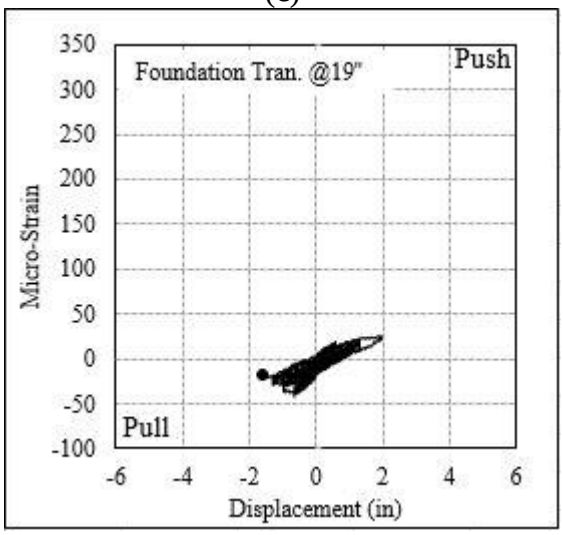
Foundation Tran. @19"
Push
Pull
Micro-Strain
Displacement (in)
350
300
250
200
150
100
50
0
-50
-100
-6
-4
-2
0
2
4
6

(e)

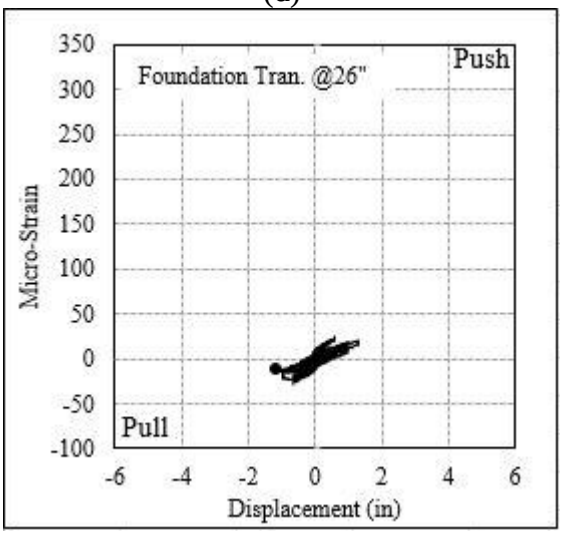
Foundation Tran. @26"
Push
Pull
Micro-Strain
Displacement (in)
350
300
250
200
150
100
50
0
-50
-100
-6
-4
-2
0
2
4
6

(f)

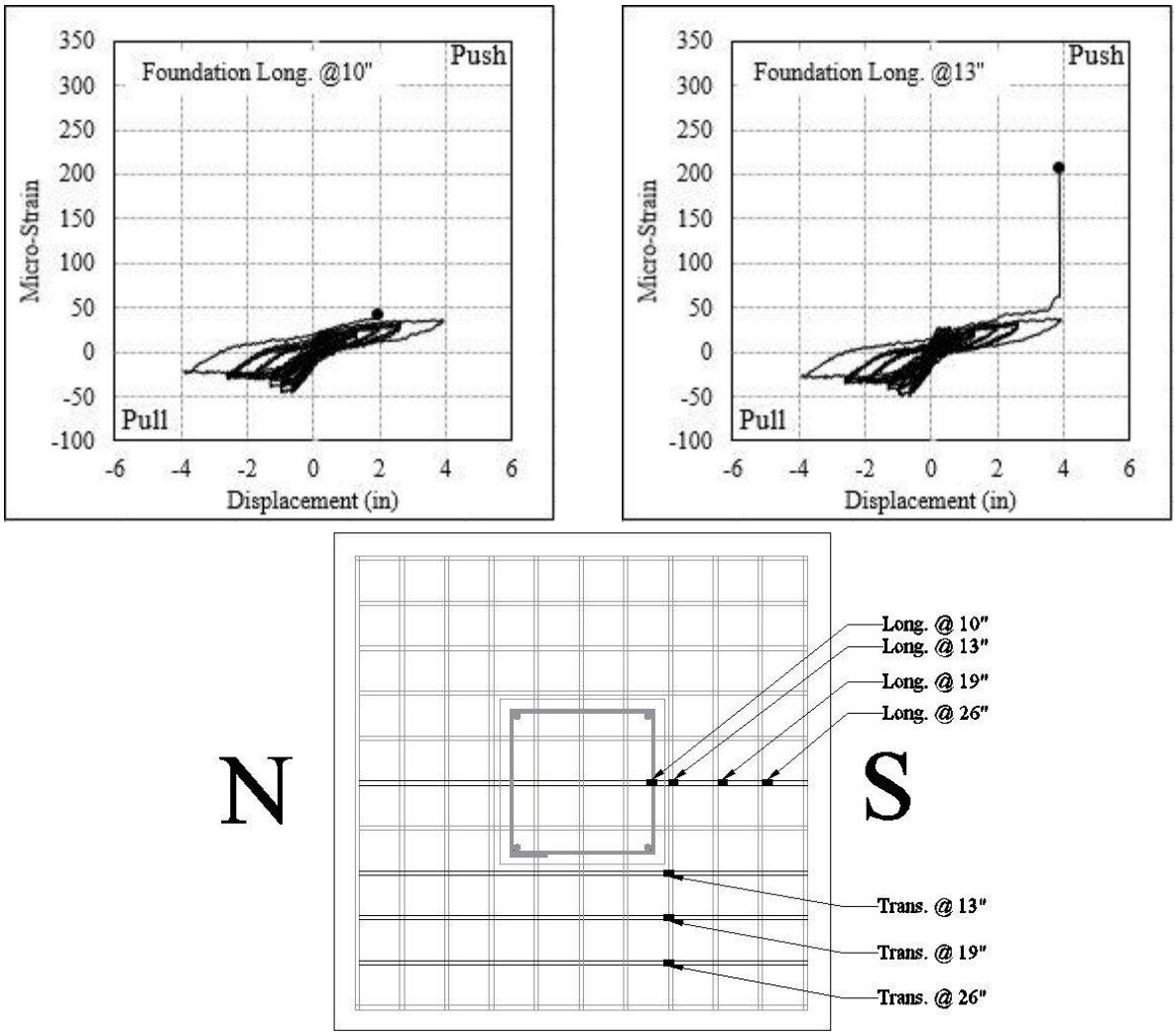

(g)

Figure A-9: Foundation Rebar strain hysteresis for specimen LVF#8 (a) Longitudinal rebar @ 10" from column center, (b) Longitudinal rebar @ 13" from column center, (c) Longitudinal rebar @ 26" from column center, (d) Transverse rebar @ 13" from column center, (e) Transverse rebar @ 19" from column center, (f) Transverse rebar @ 13" from column center and (g) Instrumentation designation.